

GROWTH, PROPERTIES, AND REACTIVITY OF
HIGH-CONCENTRATION OXYGEN PHASES ON Pt(100)

By

ROBERT BRADLEY SHUMBERA

A DISSERTATION PRESENTED TO THE GRADUATE SCHOOL
OF THE UNIVERSITY OF FLORIDA IN PARTIAL FULFILLMENT
OF THE REQUIREMENTS FOR THE DEGREE OF
DOCTOR OF PHILOSOPHY

UNIVERSITY OF FLORIDA

2008

© 2008 Robert Bradley Shumbera

To my parents and grandparents, it is my deepest desire that all of my accomplishments justify your many great sacrifices. And to my loving wife, Kristen, whose enduring support made this work possible; may it serve as a solid foundation upon which we build our future.

ACKNOWLEDGMENTS

Firstly, I express my gratitude to Dr. Jason Weaver, my supervisory committee chair and principal investigator, for his support and guidance through graduate school. I sincerely believe that our time together evolved into a friendship that I hope will continue regardless of our individual pursuits. I also thank the remaining members of my advisory committee. While limited, my interactions with Dr. David Micha and Dr. Dmitry Kopelevich were very helpful and greatly educational. In addition, I particularly appreciate Dr. Helena Hagelin-Weaver who not only advised me, but also opened her home and family to my wife and me.

I must also recognize the other students I interacted with during my time in Dr. Weaver's research group. Most notably, I acknowledge the work performed by Heywood Kan, a colleague that contributed to many of the experiments detailed in and coauthored the publications resulting from this work. Alex Gerrard, Paulo Herrera-Morales, and Jau Jiun Chen provided me with many of the tools and instruction necessary to accomplish my work. Sunil Devarajan and Jose Hinojosa offered numerous opportunities for informative discussion on a variety of topics in surface science. While not members of my research group, Mike Everett and Beverley Hinojosa also played critical roles during my time at the University of Florida.

It is important that I also express my appreciation to Dr. Jochen Lauterbach, who furnished the Pt(100) crystal utilized in the experiments performed for this work. I thank Dr. Fan Ren and Dr. Jason Butler for advising me through my teaching assistant responsibilities. For their stimulating and insightful discussions pertaining to my work, I am indebted to Dr. Charles Campbell and Dr. Aravind Asthagiri. Finally, I acknowledge the financial support provided by the Department of Energy, Office of Basic Energy Sciences, Catalysis and Chemical Transformations Division through grant number DE-FG02-03ER15478.

TABLE OF CONTENTS

	<u>page</u>
ACKNOWLEDGMENTS	4
LIST OF FIGURES	8
LIST OF ABBREVIATIONS.....	11
ABSTRACT.....	12
 CHAPTER	
1 INTRODUCTION	14
1.1 Motivation.....	14
1.2 Literature Review.....	16
1.2.1 Pt(100) Surface Structure.....	16
1.2.2 O ₂ Adsorption on Pt(100)	17
1.2.3 CO Oxidation on Pt(100).....	19
1.3 Experimental Apparatus.....	20
1.4 Experimental Techniques.....	21
1.4.1 TPD and TPRS.....	21
1.4.2 XPS	23
1.4.3 LEED	23
1.4.4 ELS.....	24
 2 ADSORPTION OF GAS-PHASE OXYGEN ATOMS ON Pt(100)-hex-R0.7°: EVIDENCE OF A METASTABLE CHEMISORBED PHASE.....	 31
2.1 Introduction.....	32
2.2 Experimental Methods	34
2.3 Results.....	35
2.3.1 O ₂ TPD from Surfaces Prepared at 573 K	35
2.3.2 LEED of Surfaces Prepared at 573 K	37
2.3.3 O ₂ TPD from Surfaces Prepared at 450 K	38
2.3.4 LEED of Surfaces Prepared at 450 K	41
2.4 Discussion	43
2.4.1 Oxygen Phase Development at 573 K	43
2.4.2 Oxygen Phase Development at 450 K	47
2.4.3 Interpretation of the TPD Measurements.....	50
2.5 Summary	53
 3 OXIDATION OF Pt(100)-hex-R0.7° BY GAS-PHASE OXYGEN ATOMS.....	 59
3.1 Introduction.....	60
3.2 Experimental Methods.....	63

3.3	Results.....	65
3.3.1	Thermal Desorption of O ₂	65
3.3.2	Characterization Using XPS and ELS.....	67
3.3.3	LEED.....	69
3.3.4	Influence of Surface Temperature.....	70
3.4	Discussion.....	71
3.4.1	Oxide Precursor Phase.....	71
3.4.2	Pt Oxide Growth and Properties.....	74
3.4.3	Pt Oxide Thermodynamic Stability.....	76
3.4.4	Oxide Decomposition Kinetics.....	81
3.5	Summary.....	83
4	THE TRANSITION FROM SURFACE TO BULK OXIDE GROWTH ON Pt(100): PRECURSOR-MEDIATED KINETICS.....	91
4.1	Introduction.....	92
4.2	Experimental Methods.....	94
4.3	Results.....	95
4.4	Kinetic Model and Analysis.....	99
4.5	Conclusions.....	109
5	TEMPERATURE PROGRAMMED REACTION OF CO ADSORBED ON OXYGEN- COVERED Pt(100): REACTIVITY OF HIGH-COVERAGE OXYGEN PHASES.....	115
5.1	Introduction.....	116
5.2	Experimental Methods.....	118
5.3	Results.....	120
5.3.1	Oxygen Preadsorbed at 575 K.....	120
5.3.2	Oxygen Preadsorbed at 450 K.....	125
5.3.3	Mass Balance Considerations.....	131
5.4	Discussion.....	134
5.5	Summary.....	138
6	ISOTHERMAL OXIDATION OF CO MOLECULAR BEAMS ON OXYGEN- COVERED Pt(100).....	149
6.1	Introduction.....	150
6.2	Experimental Methods.....	152
6.3	Results.....	155
6.3.1	Oxygen Phase Development on Pt(100).....	155
6.3.2	CO Adsorption on Pt(100).....	157
6.3.3	Reaction with Low Initial Oxygen Coverages.....	157
6.3.4	Reaction with High Initial Oxygen Coverages.....	161
6.3.5	Partial Reduction of an Oxidized Surface.....	164
6.4	Discussion.....	166

6.4.1	Reactivity of Pt(100) with Initial Oxygen Coverages Below 1 ML	167
6.4.2	Reactivity of Pt(100) Partially Covered by 3D Oxide	170
6.5	Summary	176
7	CONCLUSION.....	186
7.1	Synopsis	186
7.2	Future Considerations	188
7.2.1	Structural Investigations.....	188
7.2.2	Reactivity Studies	189
7.2.3	Computational Modeling	189
7.2.4	Generality of Findings	190
	LIST OF REFERENCES.....	191
	BIOGRAPHICAL SKETCH	198

LIST OF FIGURES

<u>Figure</u>	<u>page</u>
1-1 O ₂ TPD spectra obtained after an O ₂ saturation exposure on Pt(100)-hex-R0.7°	26
1-2 Schematic depicting the upper level of the UHV system	27
1-3 Schematic depicting the lower level of the UHV system and the two-stage, differentially-pumped chamber.....	28
1-4 XPS (Al K _α) survey spectrum obtained from a clean Pt(100)-hex-R0.7° surface	29
1-5 A simple model of LEED	30
2-1 O ₂ TPD spectra obtained after exposing Pt(100)-hex-R0.7° at 573 K to an atomic oxygen beam	55
2-2 LEED images recorded after exposing Pt(100)-hex-R0.7° at 573 K to an atomic oxygen beam	56
2-3 O ₂ TPD spectra obtained after exposing Pt(100)-hex-R0.7° at 450 K to an atomic oxygen beam	57
2-4 LEED images recorded after exposing Pt(100)-hex-R0.7° at 450 K to an atomic oxygen beam	58
3-1 O ₂ TPD spectra obtained after exposing Pt(100)-hex-R0.7° at 450 K to an atomic oxygen beam (lower coverages)	85
3-2 O ₂ TPD spectra obtained after exposing Pt(100)-hex-R0.7° at 450 K to an atomic oxygen beam (higher coverages)	86
3-3 XPS Pt 4f (Al K _α) spectra obtained after adsorbing atomic oxygen on Pt(100)-hex- R0.7° at 450 K using an oxygen-atom beam	87
3-4 ELS spectra obtained after adsorbing atomic oxygen on Pt(100)-hex-R0.7° at 450 K using an oxygen-atom beam	88
3-5 LEED images recorded after exposing Pt(100)-hex-R0.7° at 450 K to an atomic oxygen beam	89
3-6 Uptake curves obtained by plotting the atomic oxygen coverages generated on Pt(100)-hex-R0.7°	90
4-1 Uptake curves showing the coverages generated on Pt(100) at 450 K for different incident fluxes.....	111

4-2	Uptake curves showing the coverages generated on Pt(100) at ~ 575 K for different incident fluxes.....	112
4-3	O ₂ TPD spectra obtained after exposing Pt(100)-hex-R0.7° at 575 K to an atomic oxygen beam with an incident flux of approximately 3.5×10^{-2} ML s ⁻¹	113
4-4	Oxygen coverages generated on Pt(100) as a function of the surface temperature for an approximately 124.3 ML exposure.....	114
5-1	O ₂ TPD traces obtained from initial oxygen coverages on Pt(100) at 575 K without coadsorbed CO and O ₂ TPRS traces obtained after exposing the oxygen-covered surfaces to 27 ML of CO at 100 K.....	141
5-2	CO ₂ TPRS traces obtained after exposing 27 ML of CO at 100 K on Pt(100) with oxygen precoverages prepared at 575 K.....	142
5-3	CO TPRS traces obtained by exposing 27 ML of CO at 100 K on clean Pt(100) and with oxygen precoverages prepared at 575 K.....	143
5-4	O ₂ TPD traces obtained from initial oxygen coverages prepared at 450 K without coadsorbed CO and O ₂ TPRS traces obtained after exposing the oxygen-covered surfaces to 27 ML of CO at 100 K.....	144
5-5	CO ₂ TPRS traces obtained after exposing 27 ML of CO at 100 K on Pt(100) with oxygen precoverages prepared at 450 K.....	145
5-6	CO TPRS traces obtained by exposing 27 ML of CO at 100 K on clean Pt(100) and with oxygen precoverages prepared at 450 K.....	146
5-7	Estimated CO ₂ yields, total CO adsorbed, and reaction probability for TPRS.....	147
5-8	Estimated concentration of oxygen lost to the bulk during TPRS.....	148
6-1	O ₂ TPD spectra obtained after exposing Pt(100) at 575 K and 450 K to an atomic oxygen beam.....	178
6-2	CO TPD spectra obtained after exposing Pt(100) at 315 K to a CO molecular beam.....	179
6-3	CO ₂ production rates and corresponding reaction probabilities obtained by exposing various oxygen-covered surfaces held at 400 K to a CO molecular beam.....	180
6-4	CO ₂ production rates and corresponding reaction probabilities obtained by exposing a 0.61 ML oxygen-covered surface prepared at 575 K and a 0.52 ML oxygen-covered surface prepared at 450 K to a CO molecular beam.....	181
6-5	CO ₂ production rates and corresponding reaction probabilities obtained by exposing oxygen-covered Pt(100) surfaces held at 400 K to a CO molecular beam.....	182

6-6	Plot showing that the CO exposure required to reach the maximum CO ₂ production rate and the full width at half-maximum of the rate curves both increase linearly with the initial oxygen coverage	183
6-7	CO ₂ production rates and corresponding reaction probabilities obtained by exposing Pt(100) precovered with 2.1 ML and 4.2 ML of oxygen generated at 450 K to a CO molecular beam	184
6-8	O ₂ TPD traces obtained from 4.2 ML and 0.69 ML of oxygen atoms prepared on Pt(100) at 450 K and after approximately 23.4 ML of CO partially reduces the 4.2 ML covered surface	185

LIST OF ABBREVIATIONS

2D	two-dimensional
3D	three-dimensional
AES	Auger electron spectroscopy
DC	direct current
DFT	density functional theory
ELS	electron energy loss spectroscopy
ISS	ion scattering spectroscopy
LEED	low energy electron diffraction
ML	monolayer, where 1 ML is defined as one adsorbate per substrate atom
PID	proportional-integral-derivative
QMS	quadrupole mass spectrometer
RF	radio frequency
STM	scanning tunneling microscopy
TPD	temperature programmed desorption
TPRS	temperature programmed reaction spectroscopy
UHV	ultrahigh vacuum
UV	ultraviolet
XPS	X-ray photoelectron spectroscopy

Abstract of Dissertation Presented to the Graduate School
of the University of Florida in Partial Fulfillment of the
Requirements for the Degree of Doctor of Philosophy

GROWTH, PROPERTIES, AND REACTIVITY OF
HIGH-CONCENTRATION OXYGEN PHASES ON Pt(100)

By

Robert Bradley Shumbera

May 2008

Chair: Jason F. Weaver
Major: Chemical Engineering

Pt oxidation is of fundamental scientific interest and is critically important to many applications of heterogeneous catalysis since the active surface of a Pt catalyst can be in a variety of oxygen-covered states under the operating conditions of typical catalytically relevant processes. Given that such oxygen phases can significantly affect catalyst performance, there is substantial motivation for pursuing a detailed understanding of Pt oxidation. As such, we utilized gas-phase atomic oxygen beams and surface analysis techniques in ultrahigh vacuum to investigate the growth, properties, and reactivity of high-concentration oxygen phases on the Pt(100) surface.

We find that, for relatively low coverages, the types and relative populations of oxygen phases that develop are highly dependent on the surface temperature during adsorption. Indeed, a disordered oxygen state preferentially forms at 450 K, at the expense of a two-dimensional, surface oxide that forms at 575 K. Thus, the disordered state appears to be metastable relative to the two-dimensional oxide. For higher coverages, oxygen atoms apparently adsorb on top of the two-dimensional oxide and act as a precursor to forming bulk-like, three-dimensional oxide particles. We show that a model assuming these precursor oxygen atoms can either associatively desorb or react with the two-dimensional oxide to form a three-dimensional oxide particle

quantitatively reproduces the measured kinetics governing the transition from two-dimensional to three-dimensional oxide growth.

By examining the reactivity of the oxygen-covered Pt(100) surfaces toward the oxidation of CO, we find that the reaction is facile on oxygen phases that form below coverages of about one monolayer and inefficient when three-dimensional Pt oxide particles partially cover the surface. Our work shows that the intrinsic reactivity toward CO is highest for the two-dimensional oxide and lowest for the three-dimensional oxide. At higher temperatures, reaction also occurs on metallic regions of the surface covered with relatively low concentrations of chemisorbed oxygen atoms, while the morphology of the three-dimensional oxide strongly influences the kinetics. Our work supports the growing evidence that three-dimensional oxide on Pt surfaces is less reactive toward CO oxidation than the oxygen phases that form at intermediate coverages.

CHAPTER 1 INTRODUCTION

1.1 Motivation

The oxidation of Pt and other late transition metals is of fundamental scientific interest to many applications of heterogeneous catalysis, including fuel processing applications, the selective oxidation of organic compounds, and pollution control in automobiles. Indeed, under the operating conditions of typical catalytically relevant processes, the active surface of a transition-metal catalyst can be in an oxidized state, and the extent of surface oxidation can significantly affect catalyst performance since transition metals and their oxides usually exhibit different chemisorptive and reactive properties. In addition, a variety of oxygen states can exist on transition-metal surfaces that are distinct from a dilute chemisorbed layer and thick bulk oxides. The possibility that such states interact uniquely with reactant molecules provides substantial motivation for pursuing a detailed understanding of the oxidation of late transition-metal surfaces. Unfortunately, however, difficulties associated with the adsorption of high oxygen concentrations on late transition-metal surfaces in UHV stemming from a kinetic hindrance toward O₂ activation have generally limited surface science studies to low coverages of atomic oxygen.

Intermediate oxygen phases have been the focus of several recent investigations of oxidation reactions on Pt surfaces. For example, Gerrard and Weaver [1] report that oxygen-covered Pt(111) becomes less catalytically active towards CO oxidation as bulk-like oxide domains populate the surface. In contrast, *in situ* high-pressure STM studies [2,3] suggest that oxidized Pt(110) exhibits substantially higher reactivity with CO than oxygen atoms adsorbed on the metallic surface. DFT studies also show general disagreement with Seriani et al. [4] showing that α -PtO₂ on Pt(111) is inactive toward methane dissociation and CO oxidation, while Pedersen

et al. [5] find small CO oxidation energy barriers for the surface oxide and the $(10\bar{1}0)$ facet of α -PtO₂ on Pt(110). Moreover, Li and Hammer [6] posit the existence of special reaction sites near the boundaries of bulk oxide and metallic surface domains characterized by relatively small energy barriers toward CO oxidation. Perhaps most interestingly, a recent study [7] demonstrates that the CO oxidation activities of several late transition-metal surfaces, including Pt, undergo a dramatic increase near oxygen coverages of 1 ML, just prior to bulk oxidation. In regards to NO oxidation, Getman and Schneider [8] employ DFT calculations and plane-wave supercell models to show that similar intermediate oxygen coverages tend to promote NO conversion to NO₂. Clearly, there are many unanswered questions regarding and, given the current state of knowledge, ample motivation for investigating the surface oxygen phases formed on Pt and the properties that characterize these states.

In the present work, we utilized gas-phase atomic oxygen beams to investigate the surface oxygen phases formed on Pt(100). For relatively low oxygen coverages, we find that the types and relative populations of the oxygen phases that develop on Pt(100) strongly depend on the surface temperature during adsorption. At 450 K, a disordered, high-concentration state preferentially forms at the expense of an ordered, 2D oxide that populates at higher surface temperatures, implying that the disordered state is metastable relative to the surface oxide. For higher oxygen coverages, oxygen atoms adsorb weakly on the surface oxide, and act as a precursor to the formation of 3D, bulk-like oxide particles. Thermodynamic considerations show that the thermal stability of the resulting oxidized surfaces greatly exceeds that of bulk PtO₂ but do not fully account for the enhanced stability, suggesting that large kinetic barriers hinder oxide formation and decomposition. We further probed the role of the precursor state in mediating the transition from 2D to 3D oxide growth on Pt(100) by measuring the oxygen uptake as a function

of the incident oxygen-atom flux. We show that the measured kinetics are quantitatively reproduced by a model which assumes that oxygen atoms adsorb onto the 2D oxide and that this precursor can either associatively desorb or react with the 2D oxide to form a 3D oxide particle. Lastly, we investigated the reactivity of oxygen-covered Pt(100) toward the oxidation of CO, finding that the surface oxygen phase distribution strongly influences the reaction. Generally, decreases in the CO and oxygen binding strengths correlate with increasing reactivity of the oxygen phases. Interestingly, while the reaction is facile on oxygen phases that form below coverages of about 1 ML, it is inefficient when 3D oxide particles cover the surface, likely due to kinetic barriers associated with the creation and transport of Pt adatoms.

1.2 Literature Review

1.2.1 Pt(100) Surface Structure

Pt(100) is an intriguing transition-metal surface since it exhibits many thermodynamically favorable structures. Upon heating a bulk-terminated Pt(100)-(1×1) surface above about 400 K, the surface reconstructs into a quasihexagonal arrangement [9,10] through an intermediate (1×5) structure [11]. This quasihexagonal surface yields a LEED pattern consistent with a (5×20) or (5×25) structure, but is better described in matrix notation as $\begin{pmatrix} 14 & 0 \\ 0 & 5 \end{pmatrix}$ [12] or, more commonly, Pt(100)-hex [13]. Further annealing above approximately 1100 K causes a 0.7° rotation relative to the underlying bulk-truncated square lattice [13]. Assigned the matrix designation $\begin{pmatrix} 14 & 1 \\ -1 & 5 \end{pmatrix}$ [12], this reconstruction is commonly labeled Pt(100)-hex-R0.7° [13]. The (1×1), (1×5), and hex structures are metastable orientations, while the hex-R0.7° arrangement is the thermodynamically favored reconstruction.

Interestingly, exposing Pt(100)-hex- $R0.7^\circ$ to species such as CO, NO, H₂, O₂, and hydrocarbons induces deconstruction during adsorption and a reversal of the thermodynamically favored structure to the (1×1) square lattice [14-16]. For example, Hopkinson et al. [17,18] report that CO can induce the deconstruction process through the concerted action of 4 or 5 CO molecules and about 9 surface Pt atoms. In this case, the difference in the low-coverage CO heats of adsorption on the hex and (1×1) surfaces provides the driving force for the deconstruction during adsorption [19]. Since the Pt atom density of the reconstruction is 23.7% greater than that of the (1×1) surface, the deconstruction process also involves the ejection of Pt atoms that then self-diffuse and coalesce to form islands and steps [12,20].

1.2.2 O₂ Adsorption on Pt(100)

The interactions of O₂ with Pt(100) have been extensively investigated in UHV [14-16,21-27]. At low surface temperatures, O₂ molecularly adsorbs on the reconstructed Pt(100) surface [21]. However, early attempts to adsorb atomic oxygen by dissociating O₂ provided conflicting results with some studies [14,22] reporting no uptake and others [23-25] suggesting that adsorption requires high O₂ pressures or elevated temperatures. Indeed, efficient clean-off reactions between adsorbed oxygen and background H₂ and CO are the principal barrier to achieving high oxygen coverages on Pt(100) in UHV [15]. By controlling background conditions, researchers eventually generated reproducible oxygen-covered surfaces, concluding that adsorption depends on both O₂ pressure and surface temperature with an initial sticking probability of about 4×10^{-3} at 573 K [15,16,26]. Furthermore, an observed temperature enhancement of the saturation coverage and of the sticking probability under high ambient O₂ exposures suggests that dissociative O₂ adsorption is an activated process [16,24,26]. Finally, a more recent study indicates the existence of intrinsic and extrinsic precursor states, a strong

coverage dependence of the sticking coefficient, and a difference in the states populated at high incident energies [27].

The saturation TPD trace that results from exposing Pt(100)-hex- $R0.7^\circ$ at 573 K to O₂ in UHV exhibits three distinct peaks centered at approximately 631 K, 656 K, and 775 K and labeled β_1 , β_2 , and β_3 , respectively (Figure 1-1). Kneringer and Netzer [24] first reported three separate O₂ TPD features after exposing the sample at ambient temperature to approximately 10^{-3} Pa O₂ but did not observe obvious structural changes at low oxygen coverages. Conversely, Lang and coworkers [23] suggested that a $(2\sqrt{2}\times\sqrt{2})R45^\circ$ structure forms under high temperature and O₂ pressure conditions for coverages up to about 0.25 ML, where 1 ML is equivalent to the Pt(100)-(1 \times 1) surface density of 1.28×10^{15} atoms cm⁻² [9]. In the first study to adsorb appreciable oxygen concentrations, Barteau, Ko, and Madix [15] examined the β_1 and β_2 features and estimated the saturation coverage obtained at 585 K to be approximately 0.69 ML. Moreover, they linked the observed β_1 desorption characteristics to an autocatalytic process involving attractive interactions that causes an increasing desorption activation energy with increasing oxygen coverage. Later, Norton et al. [26] identified the β_3 state with a local coverage of approximately 0.1 ML and associated it with adsorption onto defects that arise from the 0.7° surface rotation.

A comprehensive study by Griffiths et al. [16] determined the saturation coverage that results from exposing Pt(100)-hex- $R0.7^\circ$ at 573 K to O₂ in UHV is 0.63 ML. Furthermore, they correlated the β_2 desorption feature with a disordered (3 \times 1) oxygen-stabilized surface reconstruction that forms over the range of approximately 0.37 ML to 0.44 ML based on observations of a streaky (3 \times 1) LEED pattern after desorbing roughly 0.2 ML from an oxygen saturated surface. Finally, as the β_1 feature becomes dominant in TPD at higher coverages,

clusters of multiple-order spots appear around the $\frac{1}{3}$ -order positions in LEED patterns and intensify with increasing oxygen coverage, leading investigators to relate the β_1 peak to a “complex” oxygen phase [15,16]. Interestingly, work function measurements [16] suggest that this complex phase consists of Pt and oxygen atoms organized in a 2D layer that resides on top of the surface.

1.2.3 CO Oxidation on Pt(100)

The oxidation of CO on Pt and Pt-group metals remains one of the most widely studied and technologically relevant catalytic reactions dating back to the classic work by Langmuir [28]. An in-depth review by Engel and Ertl [29] highlights the significant advances made in understanding the details of CO adsorption and reaction on the surfaces of Pt-group metals, establishing that CO oxidation occurs via a Langmuir-Hinshelwood mechanism whereby both reactants fully adsorb on the surface during the reaction. CO oxidation on Pt(100) has attracted considerable interest since, under certain conditions, the catalytic activity can exhibit temporal oscillations and spatio-temporal pattern formation [30]. Specifically, Ertl and coworkers [31] present clear evidence that dramatic differences in the sticking coefficient for dissociative O_2 adsorption on the surface's hex and (1×1) reconstructions are responsible for the observed kinetic oscillations.

Like the dissociative adsorption of O_2 on Pt(100), the chemisorption of CO removes the quasi-hexagonal surface reconstruction, passing through $c(2 \times 2)$ and $(\sqrt{2} \times \sqrt{2})R45^\circ$ phases before saturating in $c(4 \times 2)$ domains at 0.75 ML [9,18,32]. Interestingly, Behm et al. [33] did not observe phase mixing or compression during CO oxidation on Pt(100) at 355 K, instead reporting coexisting $c(2 \times 2)$ CO and (3×1) oxygen domains. Barteau, Ko, and Madix [34] showed that adsorbed CO inhibits dissociative O_2 adsorption, effectively blocking it at CO coverages

greater than 0.5 ML, while chemisorbed oxygen atoms do not inhibit CO adsorption. In addition, for surface temperatures greater than 300 K, they suggested that the reaction of CO with preadsorbed oxygen atoms on Pt(100) occurs at the boundaries of oxygen islands with an activation energy of $131.4 \text{ kJ mol}^{-1}$ [34], although the mechanistic details are not fully resolved [35]. Unfortunately, there is a lack of information concerning CO oxidation via reaction between coadsorbed CO and oxygen atoms on Pt(100) at low surface temperatures. Indeed, only two previous investigations [36,37] report such data, finding two CO_2 TPRS features at approximately 290 K and 350 K for relatively low oxygen precoverages.

1.3 Experimental Apparatus

To probe the surface oxygen phases formed on Pt(100) we utilized a UHV system. Characterized by pressures less than approximately 10^{-9} Torr, UHV is critical for several high-volume production applications like semiconductor devices, thin-film media heads, and extreme UV lithography systems [38]. According to the kinetic theory of gas, the mean free path of N_2 at room temperature and 10^{-9} Torr is approximately 50 km. In other words, an atom or molecule in UHV is substantially more likely to interact with the walls of the vacuum vessel than with another gas-phase species or the surface of a sample. As such, UHV enables studying atomically clean surfaces in the absence of contamination and utilizing various experimental techniques without interference from gas-phase collisions [39].

Gerrard [40] and Gerrard, Chen, and Weaver [41] provide excellent descriptions of the UHV system used in the present investigations. Evacuated by an ion pump (400 L s^{-1}), a turbomolecular pump (210 L s^{-1}), and a Ti sublimation pump inserted into a liquid N_2 cryoshield, our three-level chamber is able to reach base pressures of less than 10^{-10} Torr. The upper level, shown in Figure 1-2, consists of a hemispherical analyzer (Specs EA10 plus), a dual Al/Mg anode X-ray source (Specs XR-50), a variable energy electron source (Specs EQ 22/35), and an

ion source (Specs IQE 11). These devices afford capabilities for performing XPS, AES, ELS, ISS, and surface cleaning via ion sputtering. Designed primarily for gas dosing, the middle level contains a directed doser connected to a leak valve and a calibrated molecular beam doser similar to that described by Yates [42]. Depicted in Figure 1-3, the lower level contains LEED optics and a QMS. In addition, a two-stage, differentially-pumped vacuum chamber, attached to the lower level of the main chamber, houses a plasma source used to generate atomic oxygen beams.

The specific design of the differentially-pumped side chamber allows flexible exchange between different plasma sources and facilitates maintaining UHV conditions in the main vacuum chamber during source operation. In the experiments presented in this text, we utilized two commercial sources (Oxford Scientific Instruments) that deliver varying atomic oxygen incident fluxes on the sample surface. Gerrard [40] details the microwave-generated plasma source, while Kan et al. [43] describes the inductively-coupled RF plasma source. Regardless of the source specifics, we produce gas-phase oxygen atoms by dissociating O₂ (BOC gases 99.999%) in a plasma confined to a small reservoir near the end of the source. Species exit the plasma volume through an orifice(s) at the reservoir terminus, forming a beam directed toward the sample in the main UHV chamber. In the first pumping stage, the beam passes between oppositely charged plates ($\pm 10 \text{ kV cm}^{-1}$), deflecting charged particles from the beam path. The beam then flows through a conical skimmer separating the first and second pumping stages before collimating within a quartz tube that delivers the beam to the sample.

1.4 Experimental Techniques

1.4.1 TPD and TPRS

TPD, sometimes termed thermal desorption spectroscopy, is a surface science technique that allows for quantitative measurements of thermodynamic and kinetic parameters of desorption processes. Masel [39] and King [44] provide comprehensive reviews of TPD,

including discussions of common analytical approaches to analyzing the resulting data. Typical TPD experiments involve the adsorption of a gas on a surface at relatively low temperature and then heating the surface at a linear rate while measuring the partial pressure of desorbed species with a QMS. A related technique called TPRS is slightly more complex in that multiple gases are initially coadsorbed on the surface and reaction products are monitored during the heating procedure. Traditionally plotted as the desorption rate vs. the sample temperature, a sample TPD spectra is shown in Figure 1-1 (discussed above).

Since adsorption on metal surfaces is generally non-activated, the activation energy for desorption can be approximated by the differential heat of adsorption. Moreover, Redhead [45] showed that the activation energy for desorption can be related to the desorption temperature as measured by TPD. Thus, the desorption temperature can provide information about the adsorbate-surface bond strength. Interestingly, changes in the peak shapes of a family of desorption traces obtained at various initial adsorbate coverages can provide information regarding the reaction order. Additionally, a mass balance around the surface during TPD shows that Equation 1-1 gives the desorption per unit area of adsorbent, where N is the adsorbate coverage, P is the pressure increase above the background, V is the volume of the desorption chamber, S is the system pumping speed, A is the adsorbent area, and T_g is the gas-phase temperature [44].

$$\frac{dN}{dt} = \left(\frac{V}{Ak_B T_g} \right) \left[\frac{dP}{dt} + \left(\frac{S}{V} \right) P \right] \quad (1-1)$$

For relatively large pumping speeds and low heating rates, the desorption rate is then directly proportional to the partial pressure change as measured with a QMS. Consequently, the integrated area under a desorption trace is directly proportional to the adsorbate coverage.

1.4.2 XPS

XPS, originally termed electron spectroscopy for chemical analysis, is a spectroscopic technique that provides an analysis of the composition and chemical state distribution of solid surfaces [46-48]. Briefly, XPS involves irradiating a surface with monoenergetic soft X-rays in vacuum and measuring the kinetic energy distribution of photoelectrons emitted from the surface via the photoelectric effect. Qualitative and quantitative analysis becomes possible since each element exhibits a unique photoelectron spectrum. Moreover, a spectrum obtained from a mixture is approximately an additive superposition of contributions from the photoelectrons emitted by each elemental constituent in the mixture. XPS is surface sensitive in that only photoelectrons emitted from the top few atomic layers escape the surface and reach the detector. The emitted photoelectrons have kinetic energies, E_K , given by Equation 1-2, where $h\nu$ is the energy of the incident photon, E_B is the binding energy of the atomic orbital from which the photoelectron originates, and ϕ_S is the spectrometer work function.

$$E_K = h\nu - E_B - \phi_S \quad (1-2)$$

Interestingly, the electrons from all atomic orbitals with binding energies less than the incident photon energy are excited, although each excitation occurs with different probability, or cross-section. As such, typical elemental XPS spectra exhibit multiple electron lines. Figure 1-4 provides an example XPS survey spectrum collected from clean Pt(100)-hex-R0.7° using incident Al K_α X-rays ($h\nu = 1486.6$ eV) with each contributing electron line appropriately labeled.

1.4.3 LEED

LEED probes the long-range order of periodic surface structures, providing qualitative information by analysis of diffraction spot positions and quantitative information by measuring

spot intensities as a function of the incident electron beam energy in comparison to theoretical predictions [48]. In essence, LEED involves directing a well-defined low energy electron beam at normal incidence on a sample and monitoring the diffraction pattern resulting from electrons elastically scattered by the surface. By considering the wave nature of matter, the incident beam of electrons acts as electron waves with de Broglie wavelengths, λ , near 1 Å that scatter from surface regions of high electron density. Since the de Broglie wavelength of the incident electrons is comparable with atomic spacing, interference effects associated with the periodic surface structure exist.

The simplest example depicting the LEED phenomena is a one-dimensional chain of surface atoms with equivalent atomic separation, a , and an electron beam at normal incidence (Figure 1-5). This model represents a cross-section of the surface with only the surface layer scattering the incident electrons. In the case of two adjacent atoms that scatter electrons at an angle, θ , to the surface normal, the difference in the distance the electrons travel from the surface atoms to a detector is equivalent to $a \sin \theta$. For a large periodic area of scattering centers, the diffraction intensity measured at the detector is only significant when Equation 1-3 holds.

$$a \sin \theta = n\lambda \quad (1-3)$$

In Equation 1-3, n is an integer denoting the diffraction order. Extending this model to a 2D arrangement of surface atoms involves considering an ensemble of scattering centers arranged in parallel rows as outlined by Ertl and Küppers [48].

1.4.4 ELS

ELS is a surface analytical technique that is particularly sensitive to the surface electronic structure [48]. In an ELS measurement, an electron beam with a well-defined kinetic energy impinges on a sample surface while a detector monitors the kinetic energy distribution of electrons inelastically scattered by the surface. Taking the difference between the incident and

scattered kinetic energies gives the loss energies associated with the surface excitations resulting in the inelastic scattering events. As such, detected electrons resulting from energy losses may be distinguished from other electrons in the energy distribution by varying the incident kinetic energy since loss peaks exhibit a constant energy difference with respect to the incident energy. There are five characteristic loss categories: excitation of core electrons, one-electron excitations of valence electrons (intraband or interband transitions), collective excitations of valence electrons (plasmon losses), extended fine loss structure, and vibrational excitations. Ertl and Küppers [48] provide detailed descriptions of each of these characteristic losses.

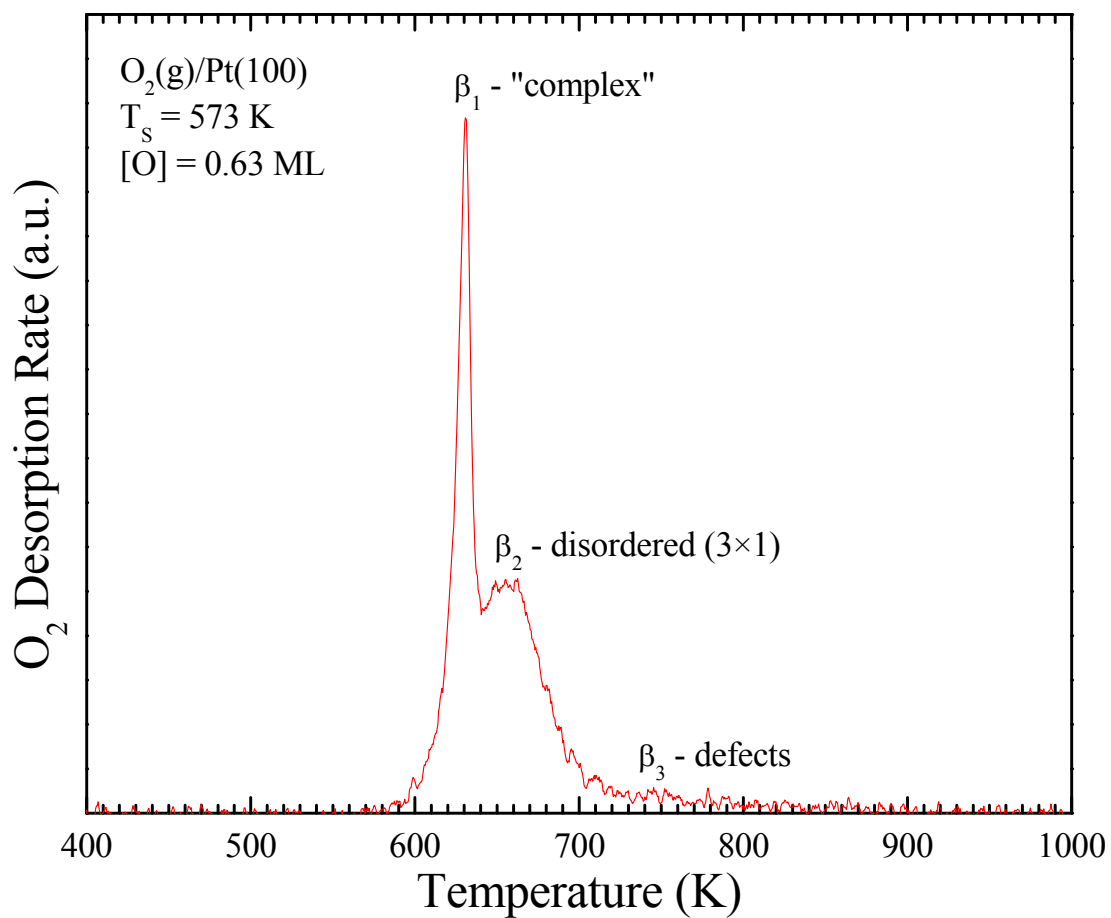


Figure 1-1. O₂ TPD spectra (temperature ramp = 1 K s⁻¹) obtained after an O₂ saturation exposure on Pt(100)-hex-R0.7° at 573 K.

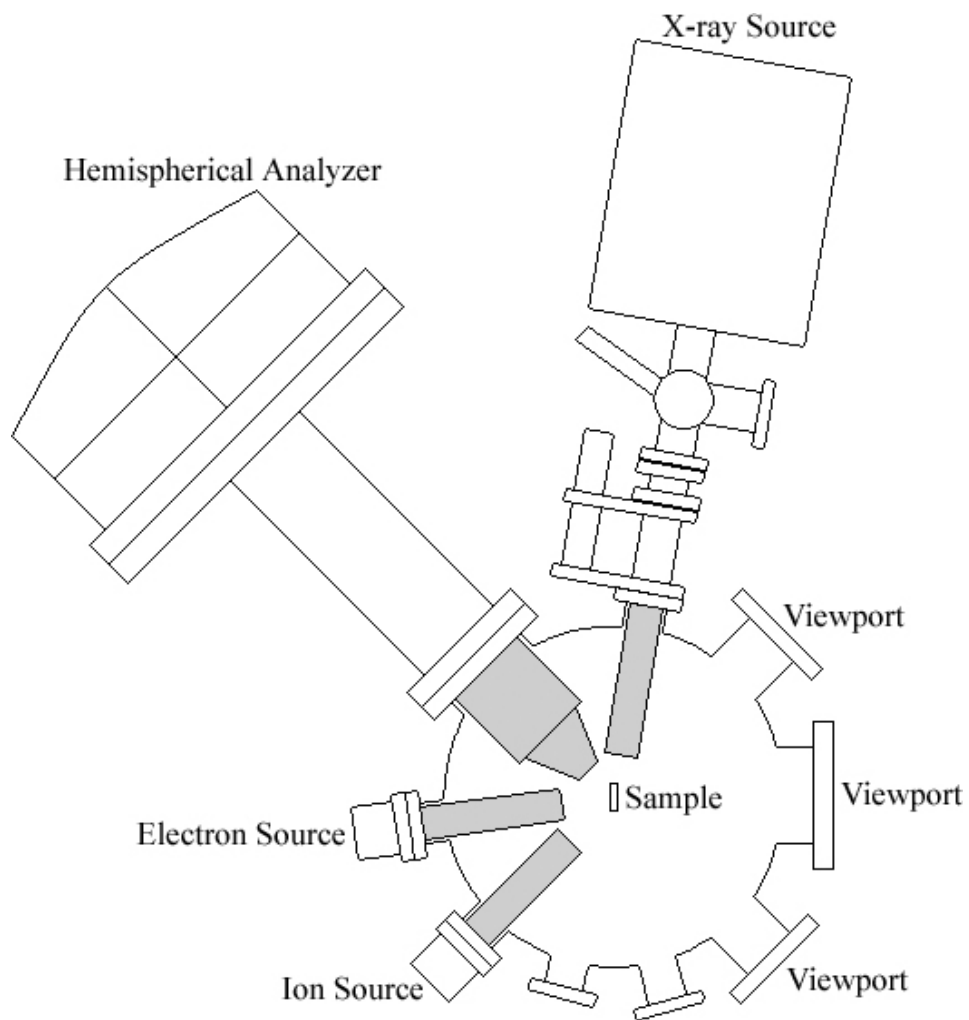


Figure 1-2. Schematic depicting the upper level of the UHV system utilized in the experiments presented in this text.

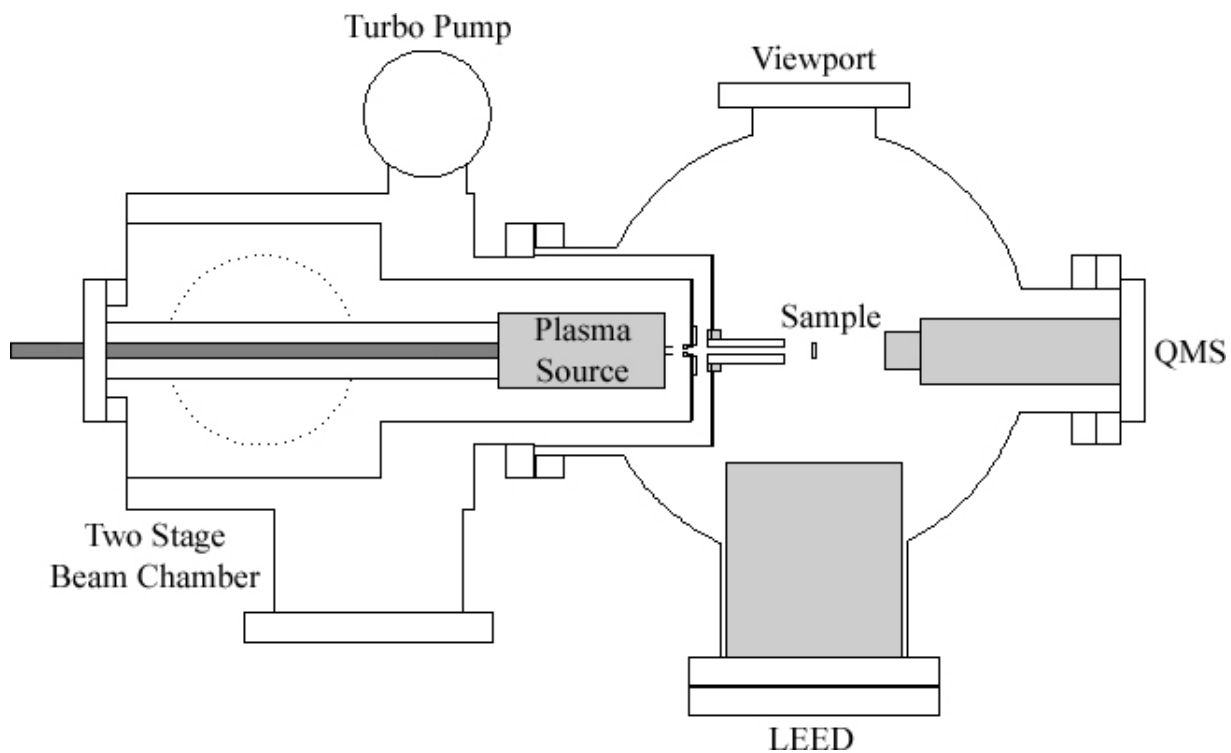


Figure 1-3. Schematic depicting the lower level of the UHV system and the two-stage, differentially-pumped chamber utilized in the experiments presented in this text.

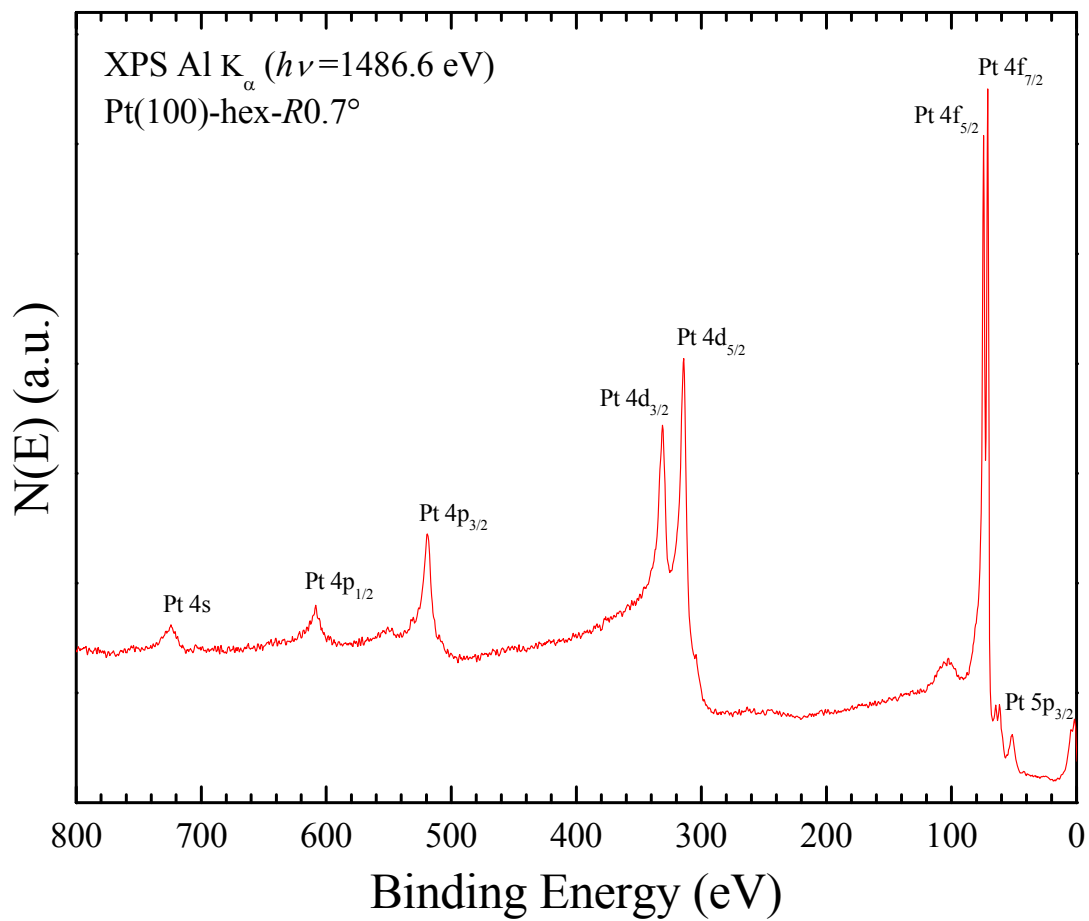


Figure 1-4. XPS (Al K_{α}) survey spectrum obtained from a clean Pt(100)-hex-R0.7° surface.

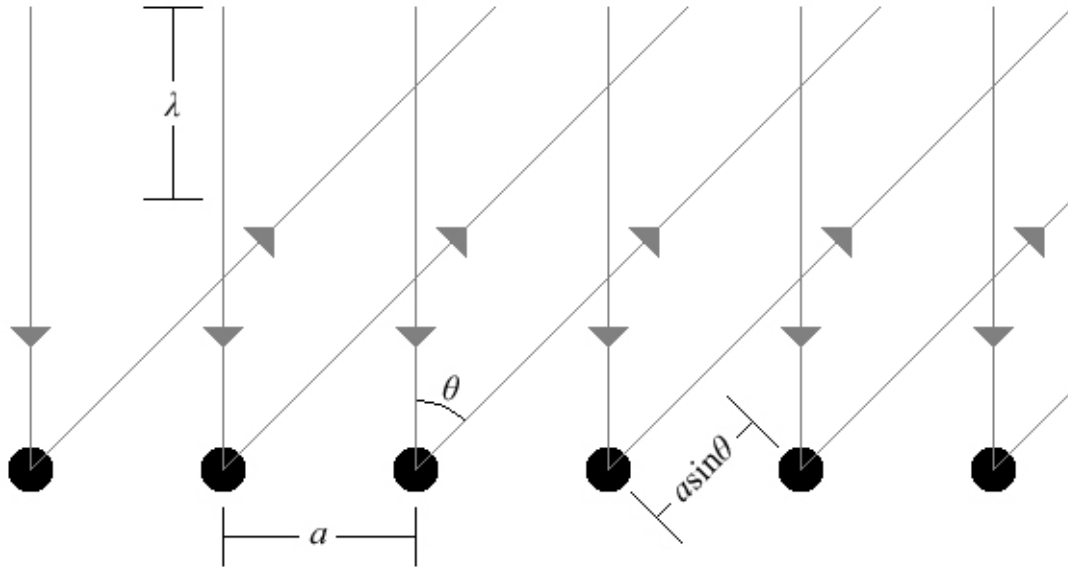


Figure 1-5. A simple model of LEED depicting the scattering of a plane wave at normal incidence by a one-dimensional periodic chain of surface atoms.

CHAPTER 2
ADSORPTION OF GAS-PHASE OXYGEN ATOMS ON Pt(100)-HEX- $R0.7^\circ$: EVIDENCE
OF A METASTABLE CHEMISORBED PHASE

This chapter reprinted from Surface Science, Volume 600, R.B. Shumbera, H.H. Kan, J.F. Weaver, Adsorption of gas-phase oxygen atoms on Pt(100)-hex- $R0.7^\circ$: Evidence of a metastable chemisorbed phase, Pages 2928-2937, Copyright (2006), with permission from Elsevier.

We utilized TPD and LEED to study the chemisorption of gas-phase oxygen atoms on Pt(100)-hex- $R0.7^\circ$ at 450 K and 573 K, and find that the types and relative populations of oxygen phases that develop are highly dependent on the surface temperature during adsorption. At both temperatures, oxygen atoms initially adsorb on defects associated with the surface reconstruction. Increasing the coverage to about 0.32 ML at 573 K causes deconstruction and population of a phase with apparent (3×1) symmetry that desorbs in a single feature centered at about 672 K. Saturating at 0.63 ML leads to the formation of an additional “complex” ordered phase that desorbs in a sharp feature exhibiting autocatalytic behavior as it shifts from approximately 631 K to 642 K. Uptake at 450 K also initiates deconstruction, but in this case two desorption maxima at about 652 K and 672 K grow simultaneously with increasing coverage to about 0.32 ML. The feature at 672 K is associated with the disordered (3×1) phase, while the feature at 652 K has not been previously reported. We attribute this new feature to desorption from disordered arrangements of high oxygen concentrations on (1×1) surface regions. As the coverage increases to about 0.51 ML, small amounts of the complex phase grow, while this “high-concentration” (1×1) and the (3×1) phases continue to develop. We conclude that the complex phase is energetically preferred over the high-concentration (1×1) phase, but kinetic barriers hinder its formation at 450 K, causing oxygen to become trapped in the high-concentration (1×1) phase. Therefore, the high-concentration (1×1) phase is metastable relative

to the complex phase. Lastly, above about 0.51 ML, further adsorption at 450 K promotes the growth of Pt oxide islands as detailed in a future investigation.

2.1 Introduction

Understanding the development and properties of oxygen phases on Pt surfaces is fundamentally important to many industrial applications of heterogeneous catalysis, including the oxidation of CO and hydrocarbon effluent combustion products. Indeed, under the highly oxidative reaction conditions employed in many commercial applications, a variety of oxygen phases may exist on Pt surfaces. These different oxygen states can have a significant influence on the kinetics of catalytic reactions since different phases may have distinct catalytic properties. For example, transitions between oxygen states are thought to cause oscillations in the rate of CO oxidation on Pt surfaces [49,50]. Therefore, it is important to characterize such oxygen phases and further investigate the conditions under which they develop in order to assist in describing and predicting the behavior of Pt catalysts operating in oxidative environments. Unfortunately, however, UHV studies of oxygen phase development on Pt surfaces have generally been limited to low coverages due to their relatively low reactivity toward O₂. Consequently, a detailed understanding of the development and properties of oxygen phases on single-crystal Pt surfaces is still lacking. In this study, we employed a microwave plasma source to produce an atomic oxygen beam that more readily generates oxygen-covered surfaces than O₂ and characterized the development and properties of chemisorbed oxygen on Pt(100).

Pt(100) is an intriguing transition-metal surface since it has many thermodynamically favorable structures. On heating bulk-terminated (1×1) Pt(100) above about 400 K, the surface reconstructs into a quasihexagonal arrangement [9,10] through an intermediate (1×5) structure [11]. This quasihexagonal surface exhibits a LEED pattern consistent with a (5×20) or (5×25)

structure, but is actually more complex and presently designated as $\begin{pmatrix} 14 & 0 \\ 0 & 5 \end{pmatrix}$ [12] or, more commonly, Pt(100)-hex [13]. Further annealing above approximately 1100 K causes a 0.7° rotation relative to the underlying bulk-truncated square lattice [13]. Assigned the designation $\begin{pmatrix} 14 & 1 \\ -1 & 5 \end{pmatrix}$ [12], this reconstruction is commonly labeled Pt(100)-hex- $R0.7^\circ$ [13]. The (1×1) , (1×5) , and hex structures are metastable orientations, while the thermodynamically favored reconstruction is the hex- $R0.7^\circ$ arrangement. Interestingly, exposing Pt(100)-hex- $R0.7^\circ$ to species such as CO, NO, H₂, O₂, and hydrocarbons induces deconstruction during adsorption and a reversal of the thermodynamically favored structure to the (1×1) square lattice [14-16].

At low surface temperatures, O₂ molecularly adsorbs on reconstructed Pt(100) [21]. However, early attempts to adsorb atomic oxygen by dissociating O₂ provided conflicting results with some studies [14,22] reporting no uptake and others [23-25] suggesting that adsorption requires high O₂ pressures or elevated temperatures. Indeed, efficient clean-off reactions between adsorbed oxygen and background H₂ and CO are the principal barrier to achieving high oxygen coverages on Pt(100) [15]. By controlling background conditions, researchers eventually generated reproducible oxygen-covered surfaces, concluding that adsorption depends on both O₂ pressure and surface temperature with an initial sticking probability of about 4×10^{-3} at 573 K [15,16,26]. Furthermore, an observed temperature enhancement of the saturation coverage and of the sticking probability under high ambient O₂ exposures suggests that dissociative adsorption is an activated process [16,24,26]. Finally, a recent study indicates the existence of intrinsic and extrinsic precursor states, a strong coverage dependence of the sticking coefficient, and different states populated at high incident energies [27]. Despite the current understanding of oxygen adsorption on Pt(100)-hex- $R0.7^\circ$, there remains many unanswered questions regarding the

characteristics of oxygen phases on Pt(100) and virtually no knowledge of adlayers formed at temperatures where clean-off reactions hinder O₂ dissociative adsorption.

2.2 Experimental Methods

Previous studies [1,41,51] provide details of the three-level UHV chamber utilized for the present experiments. The Pt(100) crystal employed in this study is a circular disk (8 mm × ~1 mm) spot-welded to W wires and attached to a copper sample holder held in thermal contact with a liquid nitrogen cooled reservoir. A type K thermocouple spot-welded to the backside of the crystal allows sample temperature measurements. Resistive heating, controlled using a PID controller that varies the output of a programmable DC power supply, supports maintaining or linearly ramping the sample temperature from approximately 80 K to 1250 K. Initially, sample cleaning consisted of sputtering with 600 eV Ar⁺ ions at a surface temperature of 800 K, followed by annealing at 1200 K for several minutes. Subsequent cleaning involved routinely exposing the sample held at 800 K to an atomic oxygen beam for several minutes, followed by flashing the sample to 1200 K to desorb oxygen and carbon oxides. We considered the sample to be clean when we could no longer detect contaminants with XPS and could obtain sharp LEED patterns consistent with the Pt(100)-hex-*R*0.7° surface [13].

By partially dissociating pure O₂ (BOC gases 99.999%) in a microwave generated plasma source (Oxford Scientific Instruments), we produce beams that contain approximately 5% oxygen atoms in a balance of O₂ and negligible quantities of impurities. Previous studies [1,41,51] provide convincing evidence that these oxygen-atom beams primarily contain ground-state, neutral species. Furthermore, we estimate that the sample surface experiences a nearly uniform atomic oxygen flux with a lower bound of $\sim 4 \times 10^{12} \text{ cm}^{-2} \text{ s}^{-1}$ ($\sim 3 \times 10^{-3} \text{ ML s}^{-1}$). Following each beam exposure, we analyzed the resulting surface using O₂ TPD or LEED. All TPD measurements began by exposing the sample to the beam at either 450 K or 573 K,

followed by cooling the sample to 300 K at a rate of -3 K s^{-1} , facing the sample toward the entrance of a QMS ionizer at a distance of about 10 mm, and increasing the sample temperature at a linear rate of 1 K s^{-1} . Cooling the sample prior to beginning the TPD measurements avoids an initial transient response in the heating by the PID controller, therefore ensuring an approximately linear temperature ramp during the evolution of O_2 . Processing the TPD spectra entailed performing a linear background subtraction on the data followed by smoothing with a 10-point adjacent averaging procedure. Operating the LEED optics using a primary electron energy of 70 eV and, to avoid field effects from the heating arrangement employed in the study, a sample temperature of approximately 80 K provided the best images when photographed with a digital camera.

2.3 Results

2.3.1 O_2 TPD from Surfaces Prepared at 573 K

In an effort to compare the surface oxygen phase development that results from exposing Pt(100)-hex- $R0.7^\circ$ to atomic oxygen with the known adsorption behavior for O_2 , we performed TPD measurements following adsorption at 573 K. Figure 2-1 displays the TPD spectra obtained after exposures to the atomic oxygen beam at a surface temperature of 573 K. Scaling the areas under the TPD traces with that obtained by dissociatively chemisorbing O_2 until saturation at 573 K allowed estimating the absolute coverages. At 573 K, the known saturation coverage of O_2 dissociative chemisorption is 0.63 ML [16], where 1 ML is equivalent to the Pt(100)-(1 \times 1) surface density of $1.28 \times 10^{15} \text{ atoms cm}^{-2}$ [9]. Interestingly, the TPD spectra we obtained for exposures to atomic oxygen are qualitatively similar to those reported in prior studies employing O_2 at surface temperatures of 570 K [25], 573 K [26], and 585 K [15]. Indeed, the saturation traces resulting from exposures to atomic oxygen and O_2 displayed perfect superposition, suggesting that the development and properties of the atomic oxygen layer prepared at 573 K are

relatively insensitive to the identity of the gaseous oxidant. Recently, Weaver et al. [51] reached the same conclusion for chemisorbed oxygen-atom coverages greater than 0.25 ML on Pt(111).

The saturation TPD trace that results from exposing Pt(100)-hex- $R0.7^\circ$ at 573 K to the atomic oxygen beam exhibits three distinct peaks labeled β_1 , β_2 , and β_3 (Figure 2-1). In an investigation of O_2 interacting with Pt(100), Kneringer and Netzer [24] first observed three separate TPD features after exposing the sample at ambient temperature to $\sim 10^{-3}$ Pa O_2 . Later, Barteau et al. [15] reported the β_1 and β_2 features and estimated the saturation coverage obtained at 585 K to be approximately 0.69 ML. A comprehensive investigation by Norton et al. [26] also identified a third state, labeled β_3 , with a coverage of approximately 0.1 ML and associated with adsorption onto defects that arise from the 0.7° surface rotation. Initially, exposing the surface held at 573 K to the atomic oxygen beam results in an extremely broad β_3 feature that desorbs over the approximate range of 600 K to 950 K. The long tail extending to 950 K persists for all coverages; however, the desorption rate from the saturated β_3 state is slightly greater than the rates from lower total coverages, in agreement with previous observations [26] utilizing O_2 .

As the coverage increases from about 0.04 ML to 0.10 ML, the spectra begin to exhibit a shoulder at approximately 672 K that corresponds to initial population of the β_2 state. Further increasing the coverage from approximately 0.10 to 0.32 ML causes the broad β_2 peak to intensify without shifting the peak temperature. Another feature, termed β_1 , also appears on the low-temperature side of the β_2 state without substantially intensifying to total coverages of about 0.32 ML, thus indicating that a majority of oxygen populates regions associated with the β_2 state. Once the coverage exceeds approximately 0.32 ML, the β_1 peak dramatically intensifies, suggesting that adsorption at higher coverages occurs primarily through the development of the β_1 state. Further increasing the coverage until saturation causes the sharp β_1 feature to

dramatically intensify and shift toward higher temperatures. Barteau et al. [15] linked the observed β_1 desorption characteristics to an autocatalytic process involving attractive interactions that causes an increasing desorption activation energy with increasing oxygen coverage. Interestingly, at saturation, the β_1 feature exhibits a slight slope change centered at about 652 K, which may indicate a previously unidentified oxygen phase.

2.3.2 LEED of Surfaces Prepared at 573 K

Figure 2-2 displays LEED images acquired at 80 K after exposures to the atomic oxygen beam at 573 K. The image from the clean surface shows a pattern consistent with published results for Pt(100)-hex- $R0.7^\circ$ [13]. Like the TPD results, the images follow the general trends reported in prior studies that employed O_2 [15,16,24]. After adsorbing about 0.19 ML, there appears to be very little change in the LEED pattern. Indeed, the $\frac{1}{5}$ -order spots associated with the reconstruction are marginally less intense with no additional spots; thus indicating no obvious structural changes at low coverages, in agreement with an early study by Kneringer and Netzer [24]. However, we did not observe the $(2\sqrt{2}\times\sqrt{2})R45^\circ$ structure previously identified [23] under high-temperature and O_2 pressure conditions for coverages up to about 0.25 ML.

As the coverage increases to approximately 0.32 ML, the $\frac{1}{5}$ -order spots become much dimmer and there is a noticeable increase in the background intensity along the direction from the (0, 0) to $(0, \frac{2}{5})$ spots. These LEED features coincide with an increase in the β_2 feature in the TPD spectra, which suggests that oxygen atoms populating the β_2 state continue the surface deconstruction while remaining disordered. In prior work, Griffiths et al. [16] correlated the β_2 desorption feature with a disordered (3×1) oxygen-stabilized surface reconstruction that forms over approximately 0.37 ML to 0.44 ML. Although a (3×1) pattern is not evident in our images, Griffiths et al. [16] made this assignment based on observations of a streaky (3×1) pattern after

desorbing ~ 0.2 ML from an oxygen-saturated surface prepared at 573 K. We observe a similar pattern when the surface is prepared in this way (not shown).

Further increasing the coverage to about 0.42 ML dramatically changes the LEED pattern. First, the disappearance of the $\frac{1}{5}$ -order spots indicates that higher coverages cause nearly complete deconstruction. Additionally, the pattern from approximately 0.42 ML exhibits clusters of multiple-order spots around the $\frac{1}{3}$ -order positions that intensify with increasing coverage to saturation. The appearance of new multiple-order spots is indicative of a surface structure that is distinct from a (3×1) phase as well as the hexagonal reconstruction. Together with the TPD measurements, these findings suggest a relation between the $\frac{1}{3}$ -order groupings and a dense β_1 phase on a predominantly deconstructed surface. Previous investigations [15,16] reported similar patterns, described as “complex,” that appear when the β_1 desorption feature becomes prominent in the TPD spectra; however, we could not locate any literature reference characterizing the real-space structure of the complex phase. Likewise, resolving the structure of the complex phase is beyond the scope of this investigation.

2.3.3 O₂ TPD from Surfaces Prepared at 450 K

In an effort to elucidate the influence of surface temperature on the development and properties of the adlayer prepared using the atomic oxygen beam, we performed TPD measurements after adsorption at 450 K. Figure 2-3 displays the TPD spectra obtained after exposures to gaseous oxygen atoms at a surface temperature of 450 K. Note that the y-axis in Figure 2-3 is half the magnitude of the y-axis in Figure 2-1. As before, scaling the areas under the TPD traces with that obtained by dissociatively chemisorbing O₂ at 573 K until saturation allowed estimating the absolute coverages. Intriguingly, the spectra we obtained for exposures at 450 K are dramatically different than those collected for exposures at 573 K. Indeed, directly

comparing the trace from a saturated surface prepared at 573 K with a similar coverage, approximately 0.65 ML, prepared at 450 K displays the drastic differences observed. In the former case, desorption yields three distinct peaks, while the latter data exhibits five features, two of which do not evolve when adsorbing oxygen at 573 K. Furthermore, measurements taken after exposures at temperatures lower than 450 K exhibited five similar features. Clearly, oxygen phase development on Pt(100) is temperature dependent over the range of 450 K to 573 K.

The TPD trace corresponding to the highest oxygen coverage we report in this study, about 0.65 ML, which results from exposing Pt(100)-hex- $R0.7^\circ$ at 450 K to the atomic oxygen beam, exhibits five distinct peaks labeled α_1 , β_1 , α_2 , β_2 , and β_3 (Figure 2-3). Initially exposures at 450 K yield the extremely broad β_3 feature that desorbs over the approximate range of 600 K to 950 K. In contrast to the feature observed for the 573 K exposures (Figure 2-1), the low-coverage β_3 feature observed for the 450 K exposures exhibits a desorption rate maximum at about 652 K, in line with the α_2 peak location for higher coverages. As in the high-temperature exposures, the long tail extending to 950 K persists for all coverages, suggesting that the β_3 feature associated with defect sites is a state that is identical for exposures at both surface temperatures and exists for all chemisorbed oxygen coverages regardless of the sample temperature during adsorption.

As the coverage increases from about 0.08 ML to 0.51 ML, the α_2 and β_2 features each intensify until reaching maximum desorption rates at approximately 0.51 ML, indicating that oxygen atoms adsorb into these states simultaneously rather than sequentially. Consistent with the TPD traces obtained after adsorption at 573 K (Figure 2-1), the spectra recorded following exposures at 450 K exhibit a broad β_2 feature that does not substantially shift in peak temperature with increasing coverage. This observation suggests that the β_2 feature represents an identical

state at both surface temperatures and exists for chemisorbed oxygen coverages greater than about 0.1 ML regardless of the sample temperature during adsorption.

The trace measured from about 0.43 ML exhibits a shoulder on the low-temperature side of the α_2 feature. Further increasing the coverage causes the shoulder to intensify and shift to higher temperatures. Additionally, superposing the spectra corresponding to 0.42 ML prepared at 573 K (Figure 2-1) and 0.51 ML prepared at 450 K (Figure 2-3) shows nearly perfect overlap between this peak and the already identified β_1 feature. Therefore, it is reasonable to assume that the peak observed on the low-temperature side of the α_2 feature is the same autocatalytic state found in the high-temperature exposures. As such, these observations suggest that the β_1 feature represents an identical state at both surface temperatures and exists for chemisorbed oxygen coverages greater than approximately 0.4 ML regardless of the sample temperature during adsorption. It is worth noting that the β_1 peak intensity for about 0.51 ML prepared at 450 K (Figure 2-3) is roughly one-third the intensity for a saturated surface prepared at 573 K (Figure 2-1).

As mentioned previously, the α_2 feature appears and grows simultaneously with β_2 for coverages ranging from approximately 0.08 ML to 0.51 ML. The α_2 peak is sharp, narrow, and more intense than its β_2 companion. At all coverages, the α_2 maximum desorption rate occurs at approximately 652 K without displaying a shift in peak location, thus suggesting that this state follows first-order desorption kinetics. Furthermore, TPD measurements performed after exposures at temperatures as low as 80 K consistently exhibit these trends. Interestingly, the slight β_1 slope change observed at about 652 K for the saturated surface prepared at 573 K (Figure 2-1) is consistent with desorption from the α_2 state, implying that this phase is obtainable, albeit to a lesser extent, at higher surface temperatures. Indeed, it is possible that the vastly more intense β_1 feature substantially dwarfs any α_2 contribution to the total trace. Despite

our best efforts, we could not locate any direct literature reference to the α_2 thermal desorption peak for the O/Pt(100) system, though this feature does appear to be present in spectra obtained after dissociatively adsorbing small amounts of O₂ at temperatures below about 534 K [15]. Thus, the present study is likely the first to identify and characterize the α_2 phase on Pt(100).

Increasing the coverage from exposures at 450 K to approximately 0.65 ML causes a broad shoulder, labeled α_1 , to develop on the low-temperature side of the β_1 peak (Figure 2-3). Centered at approximately 550 K, the α_1 state does not appear during exposures performed at 573 K. Interestingly, even though Figure 2-3 does not display data for coverages greater than about 0.65 ML, we generated coverages in excess of 3 ML during exposures at 450 K. These spectra appear in a separate study that focuses on the development and characterization of high-coverage phases on Pt(100)-hex-*R*0.7° [52]. In investigating these high coverages, we conclude that the α_1 desorption peak corresponds to an oxide precursor phase on the surface, consistent with the identification of a similar phase formed during the oxidation of Pt(111) [51].

2.3.4 LEED of Surfaces Prepared at 450 K

Figure 2-4 displays the LEED images acquired at 80 K after exposing Pt(100)-hex-*R*0.7° to the atomic oxygen beam at 450 K. As before, the image taken from a clean sample serves as a reference for images captured from the covered surfaces. After adsorbing about 0.18 ML, there is little change in the LEED pattern aside from a decrease in the intensity of the $\frac{1}{5}$ -order spots associated with losing the reconstruction. However, the decrease in intensity of these spots is more dramatic than that observed for a similar coverage, approximately 0.19 ML, prepared at 573 K (Figure 2-2). Therefore, it appears that, even at low coverages, adsorbing oxygen atoms at lower surface temperatures either facilitates the deconstruction process or produces smaller

reconstructed domains. Interestingly, in investigating the adsorption of H₂ on Pt(100), Barteau et al. [15] observed a similar threshold temperature, below which the deconstruction is observed.

As the coverage increases to approximately 0.31 ML, the $\frac{1}{5}$ -order spots become very faint and a (1×1) pattern with high background intensity appears. These changes coincide with a prominent α_2 feature in the TPD spectra (Figure 2-3), and therefore suggest that α_2 phase development causes the deconstruction to dominate at coverages of only ~0.3 ML. For comparison, the image obtained after adsorbing ~0.3 ML at 573 K exhibits a less intense background and more distinct $\frac{1}{5}$ -order diffraction spots (Figure 2-2). Analysis of the TPD spectra also shows that nearly identical quantities of the α_2 and β_1 states populate at ~0.3 ML when adsorbing at 450 K versus 573 K, respectively. Thus, the greater diminution of the $\frac{1}{5}$ -order spots after adsorption at 450 K may indicate that the α_2 phase has a lower oxygen density than the β_1 phase so that the (1×1) structure covers a larger surface area when a given quantity of oxygen adsorbs in the α_2 phase than in the β_1 phase. It is also possible, however, that the oxygen phases and therefore the reconstructed domains are smaller, on average, when uptake occurs at lower temperature, resulting in more rapid loss of the diffraction spots from the reconstruction.

Further increasing the coverage to about 0.63 ML yields a more distinct (1×1) pattern with high background intensity. For these higher coverages prepared at 450 K, the TPD measurements indicate there should be a complex pattern in the LEED images due to the β_1 phase. Indeed, the intensity within the diffuse pattern appears to be greatest along the $\frac{1}{3}$ -order positions, suggesting contributions from the complex phase. However, the $\frac{1}{3}$ -order structures are significantly less obvious than in the patterns captured from similar coverages prepared at 573 K (Figure 2-2) and appear streaky along the $(0, \frac{1}{5})$ and $(0, \frac{2}{5})$ positions, which is consistent with either a lack of

significant long-range order or much smaller complex phase domains when adsorbing at 450 K. It should be noted that the absence of $(0, \frac{3}{5})$ and $(0, \frac{4}{5})$ spots signifies that the surface deconstruction is essentially complete above ~ 0.40 ML, which allows us to rule out diffraction from small reconstructed domains as the origin of the diffuse intensity near the $\frac{1}{3}$ -order positions. As mentioned previously, we generated coverages in excess of 3 ML at 450 K. The corresponding LEED images appear in a separate study that focuses on the development and characterization of high-coverage phases on Pt(100)-hex- $R0.7^\circ$ [52]. In investigating these high coverages, we find that the images associated with populating the α_1 state show progressively greater disorder, consistent with identifying the α_1 state as an oxide precursor phase similar to the precursor phase formed during oxidation of the Pt(111) surface [51].

2.4 Discussion

2.4.1 Oxygen Phase Development at 573 K

We find that exposing Pt(100)-hex- $R0.7^\circ$ to gaseous oxygen atoms results in the development of at least three different phases of chemisorbed oxygen whose relative populations depend dramatically on the sample temperature during adsorption. For adsorption at 573 K, the data indicates chemisorbed layers develop more efficiently than adlayers prepared with O_2 , but the adlayer growth and properties are generally insensitive to the identity of the gaseous oxidant. Prior studies of O_2 dissociative adsorption therefore provide key insights for understanding the temperature dependence of the adlayer development observed in the present study.

At 573 K, oxygen atoms initially populate surface defect sites (β_3) until the coverage reaches about 0.1 ML. Beyond this, oxygen atoms likely cluster and locally deconstruct the surface via a mechanism similar to that proposed for the transformations induced by CO [17,18] and D_2 [53]. In these models, the clustering of roughly 4 adsorbate atoms or molecules within an

area of the hex- $R0.7^\circ$ surface containing 6 to 9 Pt atoms initiates or extends the deconstruction. Thus, even at low total coverages, oxygen atoms cluster to form domains with relatively high local concentration, while surrounding reconstructed areas remain devoid of oxygen. Recent experiments using STM confirm that the oxygen layer grows in patches on Pt(100), with nucleation occurring preferentially at boundaries between rotationally degenerate reconstructed domains [54]. Interestingly, since the reconstruction is 23.7% more dense than the (1×1) [12,20], the deconstruction process involves the ejection of Pt atoms that then self-diffuse and coalesce to form islands and steps. These excess Pt adatoms may play a role in the growth of oxygen phases, particularly at higher coverages.

A higher oxygen binding energy on the (1×1) relative to the hex- $R0.7^\circ$ surfaces appears to drive the nucleation and growth of (1×1) domains, as previously discussed for the CO induced deconstruction [19,55]. The deconstruction process initiates beyond a critical local coverage at which the total energy is lower for oxygen binding on (1×1) than on hex- $R0.7^\circ$ surface regions. Recognizing that adsorption on surface defects contributes about 0.1 ML to the total coverages, we propose that this critical local coverage ranges from approximately 0.2 ML to 0.3 ML since the β_1 peak (Figure 2-1) does not significantly grow until a total coverage between about 0.32 ML and 0.42 ML. Similarly, the $\frac{1}{5}$ -order LEED spots (Figure 2-2) associated with the reconstruction vanish over this coverage range. This value for the critical local coverage is consistent with previously reported work function changes, Rutherford backscattering measurements, and nuclear microanalysis results [16] that indicate saturation of a distinct phase. In addition, Deskins et al. [56] recently employed DFT to predict that the critical local oxygen coverage for lifting the reconstruction is between 0.1 ML and 0.3 ML.

During deconstruction, oxygen atoms arrange into a dilute phase on the (1×1) surface, while displacing nearly one-third of the surface Pt atoms at least 0.025 nm from their ideal positions [16]. While we did not initially observe any specific periodicity associated with this phase in our LEED images, Griffiths et al. [16] observed a (1×1) pattern with high background intensity that they termed a disordered (3×1) since a streaky (3×1) pattern appeared after partially desorbing oxygen from a saturated surface. Likewise, we recorded a similar pattern after desorbing the β_1 feature from a saturated surface prepared at 573 K (not shown). STM images also reveal that oxygen domains grow anisotropically on Pt(100), and appear to have closer packing parallel to the original close-packed direction of the reconstruction [54], which is consistent with local (3×1) periodicity. Interestingly, oxygen atoms form a $p(3\times 1)$ phase on PtRh(100) bimetallic surfaces but not on Rh(100) [57,58], suggesting that Pt atoms effectively stabilize the $p(3\times 1)$ structure. Although slightly greater than our proposed critical local coverage, a $p(3\times 1)$ structure would yield an ideal coverage of 0.33 ML. It is certainly feasible that deviations from an ideal $p(3\times 1)$ arrangement, perhaps due to small local regions of excess Pt adatoms generated by the deconstruction process, could cause a critical local oxygen coverage lower than 0.33 ML and the disordered (3×1) LEED pattern.

Once the local (3×1) phase saturates, TPD measurements and LEED images suggest further uptake leads to a dense phase that grows at the expense of (3×1) domains. While resolving the real-space structure of the dense phase is beyond the scope of this investigation, previous investigations [15,16] reported similar “complex” LEED patterns. This complex phase is characteristic of the saturated layer prepared at 573 K by exposure to either O_2 or gaseous oxygen atoms. Assuming complete (3×1) to complex phase transformation and recognizing that defect sites contribute about 0.1 ML to the saturated surface, the local coverage in the complex

phase has a lower bound of approximately 0.5 ML. With remarkable similarity, Rutherford backscattering measurements suggest that oxygen adsorbed in the complex phase displaces nearly half of the surface Pt atoms at least 0.025 nm from their ideal positions [16].

Griffiths et al. [16] find that the work function change decreases as the complex phase populates, suggesting a decrease in the dipole moment of the Pt-O bond. This is an unusual and unexpected observation since the work function change should increase linearly with increasing coverage if oxygen atoms have a constant dipole moment and reside on top of the surface. As such, the decreasing work function change is indicative of more “buried” oxygen atoms in the complex phase that experience lateral interactions with Pt atoms, effectively reducing the net dipole moment of the Pt-O surface bond. Such lateral interactions might arise from oxygen atoms penetrating the metal surface layer by settling into four-fold hollow sites. Considering that the saturated surface contains 0.63 ML of oxygen atoms and approximately 0.24 ML of Pt adatoms, it is also likely that local crowding induces restructuring into a complex phase involving coordination and lateral interactions between the oxygen atoms and Pt adatoms. In agreement with this notion, forming the complex phase is a thermally activated process as evidenced by generating much less of the complex phase at 450 K than 573 K. Interestingly, Rotermund et al. [59] presented a similar discussion detailing the formation of subsurface oxygen during CO oxidation on Pt(100) in which a lowering of the work function change was attributed to oxygen atoms located beneath the surface Pt atoms. However, this subsurface oxygen appears to be distinct from the β_1 oxygen as it produces a desorption feature located at temperatures slightly higher than the β_2 desorption temperature and is observed in TPD spectra that exhibit both β_1 and β_2 features.

2.4.2 Oxygen Phase Development at 450 K

Beyond the initial adsorption onto surface defects, the development of the chemisorbed adlayer by exposure to gaseous oxygen atoms at 450 K differs from that at 573 K in three primary ways. Firstly, the $\frac{1}{5}$ -order LEED spots associated with the reconstruction appear to vanish at lower coverages (Figure 2-4). We speculate that reduced adatom mobility at the lower temperature causes less clustering such that nucleation of new (1×1) domains becomes important relative to the growth of existing domains. Consistent with this notion, these domains may nucleate homogeneously by random adsorption into regions with enough local coverage to induce deconstruction. Such adsorption is possible since gas-phase oxygen atoms likely have an initial sticking probability that approaches unity. Relevant to the current observations, these multiple domains would effectively reduce the size of hexagonal regions without significantly altering the surface area covered by the reconstruction. Consequently, the reduced long-range order would yield dimmer $\frac{1}{5}$ -order LEED spots at lower total coverages. As mentioned in the Results section, it is also possible that the oxygen density is lower in the α_2 phase than in the β_1 phase, which would cause more of the surface to deconstruct when a given amount of oxygen populates the α_2 phase rather than the β_1 phase. This would also cause the $\frac{1}{5}$ -order LEED spots to fade more rapidly. Interestingly, this interpretation is consistent with studies [60-62] of the O/Pd(100) system showing that oxygen atoms arrange into a $p(5\times 5)$ structure below 570 K, with the $p(5\times 5)$ transforming into a denser $(\sqrt{5}\times\sqrt{5})R27^\circ$ phase at higher temperature. Future investigations, perhaps utilizing STM techniques, should attempt to quantify the atomic oxygen diffusivity on Pt(100) and resolve the nucleation and growth mechanism as well as the structures of the oxygen phases that develop at 450 K.

There are two other primary differences between the phase development by exposure to gas-phase oxygen atoms at 450 K and 573 K. Indeed, TPD shows that the β_2 and α_2 features grow almost simultaneously rather than sequentially during uptake at 450 K (Figure 2-3). Furthermore, the β_1 desorption feature is much less intense and appears to be replaced with the α_2 peak when adsorption is conducted at 450 K versus 573 K. Following the assumption of lower adatom mobility at 450 K, we speculate that the α_2 feature arises from oxygen that becomes trapped in “high-concentration” arrangements on (1×1) surface regions, rather than restructuring and transforming these domains into the complex β_1 phase. While continued population of the high-concentration (1×1) state to total coverages as high as 0.50 ML may indicate that this state is denser than the (3×1) phase, the LEED images suggest that the high-concentration (1×1) phase exists without distinct long-range order. This observation is consistent with the notion that lower temperatures prevent oxygen atoms from efficiently redistributing to more favorable ordered structures. The simultaneous growth of the β_2 and α_2 features may also be explained within the context of reduced adatom mobility. In particular, the random and efficient adsorption of oxygen atoms facilitates co-populating (3×1) and high-concentration (1×1) regions that do not equilibrate during the time frame of the experiment.

The preference for the complex phase to grow in place of the high-concentration (1×1) state only at the higher temperature suggests that the complex phase is energetically preferred over the high-concentration (1×1) state, but that kinetic barriers restrict the formation and growth of the complex phase at the lower temperature. Consequently, oxygen atoms become trapped in the high-concentration (1×1) phase at 450 K since the adsorption rate exceeds the complex phase formation rate at this temperature. The conversion from high-concentration (1×1) to complex regions is apparently fast at 573 K, rapidly consuming the high-concentration (1×1) phase so that

there is not a significant α_2 contribution to the TPD measurements. However, the transformation is slower at 450 K resulting in more of the high-concentration (1×1) phase remaining unconverted, especially at lower coverages. Indeed, the temperature dependent phase populations suggests that the high-concentration (1×1) state is metastable with respect to the complex phase, and likely acts as a precursor to growing the complex phase. It is conceivable that repulsive interactions within the high-concentration (1×1) state as well as thermal energy promote the phase transformation. In this case, strong repulsive interactions, enhanced with increasing local coverage, compensate a decrease in the thermal energy and enable appreciable phase transformation rates at lower temperatures. This suggests that higher local coverages must be reached for the phase transformation to proceed efficiently at lower temperatures.

Interestingly, observing the α_2 feature indicates that the high-concentration (1×1) phase does not effectively convert to the complex phase during an individual TPD measurement. This implies that desorption from the high-concentration (1×1) state is more facile than conversion to the complex phase during TPD. It is feasible that conversion occurs on a time scale that is much slower than the linear temperature ramp. However, even if the energy barriers for conversion and desorption from the high-concentration (1×1) phase are similar, the system will tend to favor desorption during TPD since there is no gaseous oxygen source to replenish the adsorbed layer. We speculate that the energetic driving forces for conversion and desorption from the high-concentration (1×1) state are similar, but that the large gradient in oxygen concentration between the high-concentration (1×1) state and the gas phase favors desorption under UHV conditions. To test this assertion, we prepared surfaces with oxygen coverages ranging from approximately 0.4 ML to 0.7 ML at 450 K and then annealed the surfaces at 573 K for ten minutes. Afterwards, we cooled the sample to 300 K, and initiated TPD. As suggested, the resulting TPD traces

resembled the spectra obtained from similar coverages prepared at 450 K, thus indicating that the high-concentration (1×1) state did not convert to the complex phase during the anneal. It is worth noting that future STM studies could provide new insight into the relationships that exist between the various surface oxygen phases and help confirm the arguments presented herein.

2.4.3 Interpretation of the TPD Measurements

In many respects, the general characteristics of the desorption traces obtained after atomic oxygen exposures at 573 K resemble those of the O/Pd(100) system [60-62]. Briefly, LEED and desorption measurements show that initial adsorption on Pd(100) feeds a $p(2\times 2)$ state, which transforms into a $c(2\times 2)$ phase for total coverages up to approximately 0.40 ML. Increasing the coverage drives further conversion into a $p(5\times 5)$ arrangement at temperatures below about 570 K and into a denser $(\sqrt{5}\times\sqrt{5})R27^\circ$ structure above 570 K. The TPD traces reported by Chang and Thiel [63] exhibit peaks labeled α , β , and γ which are analogous with respect to shape and relative intensity to the β_2 , α_2 , and β_1 features, respectively, observed after the 573 K exposures in the present investigation. The evolution of the LEED spot intensities that are unique to each phase with coverage and temperature [63,64] suggest that the O/Pd(100) α peak is due to desorption from a variable density, disordered $p(2\times 2)$ state. Moreover, the β peak coincides with desorption from the $c(2\times 2)$ phase, appearing at lower temperatures than the α feature due to next-nearest-neighbor repulsive interactions. Lastly, the γ peak signifies desorption occurring when the $(\sqrt{5}\times\sqrt{5})R27^\circ$ and (2×2) structures coexist.

Interestingly, the γ TPD feature in the O/Pd(100) system is sharp and exhibits approximately zero-order or autocatalytic desorption characteristics that resemble those of the β_1 peak in the O/Pt(100) system. A common approach utilized in previous studies [65-67] to describe explosive or autocatalytic desorption invokes the notion of island decomposition between coexisting phases. In these cases, species eject from the perimeter of a dense phase onto

one or more dilute phases so that the local coverage within the dilute phases remains constant as species desorb. More specifically, desorption directly from the dense phase occurs at a lower rate than desorption from the dilute phases and the migration rate of species from the dense phase to the dilute phases is faster than any of the desorption rates. Consequently, the total species desorption rate is proportional to the fractional surface area covered by the dilute phases, which increases as the dense phase is consumed. The net result is that the thermal desorption rate exhibits self-accelerating or autocatalytic kinetic characteristics. In the O/Pd(100) investigations [63,64], the maximum of the γ feature occurs as the system crosses the phase boundary between the $(\sqrt{5}\times\sqrt{5})R27^\circ$ and (2×2) structures so that $(\sqrt{5}\times\sqrt{5})R27^\circ$ phase consumption ends and the coverage within the (2×2) arrangement begins to decrease.

Similarly, the notion of island decomposition likely explains the desorption behavior observed in the O/Pt(100) system (Figure 2-1 and Figure 2-3). In particular, the sharpness of the β_1 feature may arise from facile transport from the complex phase to the (3×1) phase during desorption, which keeps the coverages in each phase nearly constant while they coexist. The slight shift in the β_1 peak location to higher temperatures with increasing initial coverage is consistent with a higher desorption rate from the (3×1) phase. In this case, decreasing the initial fractional surface area covered by the (3×1) phase, as occurs with increasing initial total coverage, will cause a given desorption rate to occur at higher temperatures. Recently, Weaver et al. [51] employed a similar description to explain the peak shift observed for O_2 desorption from high-coverage phases on Pt(111).

The sharp α_2 feature seen in the TPD spectra obtained after uptake at 450 K (Figure 2-3) is also indicative of oxygen interchange between phases accompanying desorption. Specifically, equilibration between the high-concentration (1×1) phase and the more dilute (3×1) state may be

sufficiently rapid to maintain roughly constant local coverages within each phase during TPD until complete consumption of the denser phase. Then, the desorption rate abruptly drops due to the decreasing oxygen concentration within the more dilute phase. To explain an analogous yet smaller peak observed in O₂ TPD spectra from Pd(100), Chang and Thiel [63] invoked a model in which the desorption activation energy continuously decreases with increasing coverage due to repulsive interactions within the adlayer. However, this model predicts a shift of the desorption maximum to lower temperatures rather than an abrupt feature, as observed in the TPD spectra obtained after atomic oxygen adsorption on Pt(100) at 450 K (Figure 2-3).

To adequately explain the characteristics exhibited by the α_2 and β_1 peaks (Figure 2-1 and Figure 2-3) using the island decomposition mechanism, transport from a dense phase to more dilute phases must be fast relative to desorption. However, the data suggests that conversion of the high-concentration (1×1) state to the complex phase is slow during TPD such that oxygen tends to desorb via rapid equilibration with the (3×1) phase. These conditions would be satisfied if the rate processes governing high-concentration (1×1) to complex phase conversion are slower than the rates for desorption and transport from the high-concentration (1×1) phase to the (3×1) state. Indeed, the annealing experiments described in the previous section support this interpretation since desorption appears to dominate over transformation to the complex state in the absence of a gaseous oxygen source. Thus, barriers to forming the complex phase are effectively overcome at the higher temperature only when the adsorption rate is maintained sufficiently high. In other words, constant replenishment of the high-concentration (1×1) phase is necessary to drive the complex phase formation at 573 K since the competing desorption pathway is favored.

2.5 Summary

We utilized TPD and LEED to investigate the chemisorption of gas-phase oxygen atoms on Pt(100)-hex- $R0.7^\circ$ at surface temperatures of 450 K and 573 K in UHV. The adsorption of oxygen atoms is facile at both temperatures, occurring with much higher probability than the dissociative chemisorption of O_2 . Because the adsorption rates are higher than the rates at which clean-off reactions remove oxygen, we were able to prepare high coverages at lower temperatures than previously examined in studies employing O_2 . Moreover, while only small coverages could be generated at 450 K using O_2 , adsorption of oxygen atoms and O_2 appear to produce identical surface phases at 573 K, suggesting that the phases prepared at lower temperatures using atomic oxygen are representative of the phases that develop at high O_2 pressures.

We find that the types and relative populations of oxygen phases that develop are highly dependent on the temperature during adsorption. Initially, oxygen atoms adsorb on defect sites associated with the reconstruction. At 573 K, continued adsorption beyond about 0.1 ML produces an oxygen phase with apparent (3×1) symmetry that desorbs in a broad TPD feature centered at about 672 K. LEED observations show that growth of the disordered (3×1) phase causes the surface to deconstruct, with the deconstruction most likely occurring locally in oxygen-covered domains. As the coverage increases beyond about 0.32 ML, a “complex” oxygen phase develops that yields an intricate LEED pattern, and gives rise to a sharp desorption feature that shifts from roughly 631 K to 642 K as the coverage approaches saturation near 0.63 ML.

Beyond initial population of defect sites, adsorption at 450 K causes the simultaneous growth of the (3×1) phase and a phase that produces a sharp TPD feature centered at approximately 652 K. LEED observations suggest this new phase corresponds to disordered

oxygen arrangements in relatively high concentrations on deconstructed Pt domains. As the coverage increases from about 0.31 ML to 0.51 ML, a small amount of the complex phase forms, while the “high-concentration” (1×1) and (3×1) phases continue to grow. The temperature dependent phase populations suggest that the complex phase is energetically preferred over the high-concentration (1×1) phase, but kinetic barriers restrict forming the complex state at 450 K for the incident fluxes employed. As such, the high-concentration (1×1) phase is metastable relative to the complex phase, and appears to act as a precursor to growing the complex state.

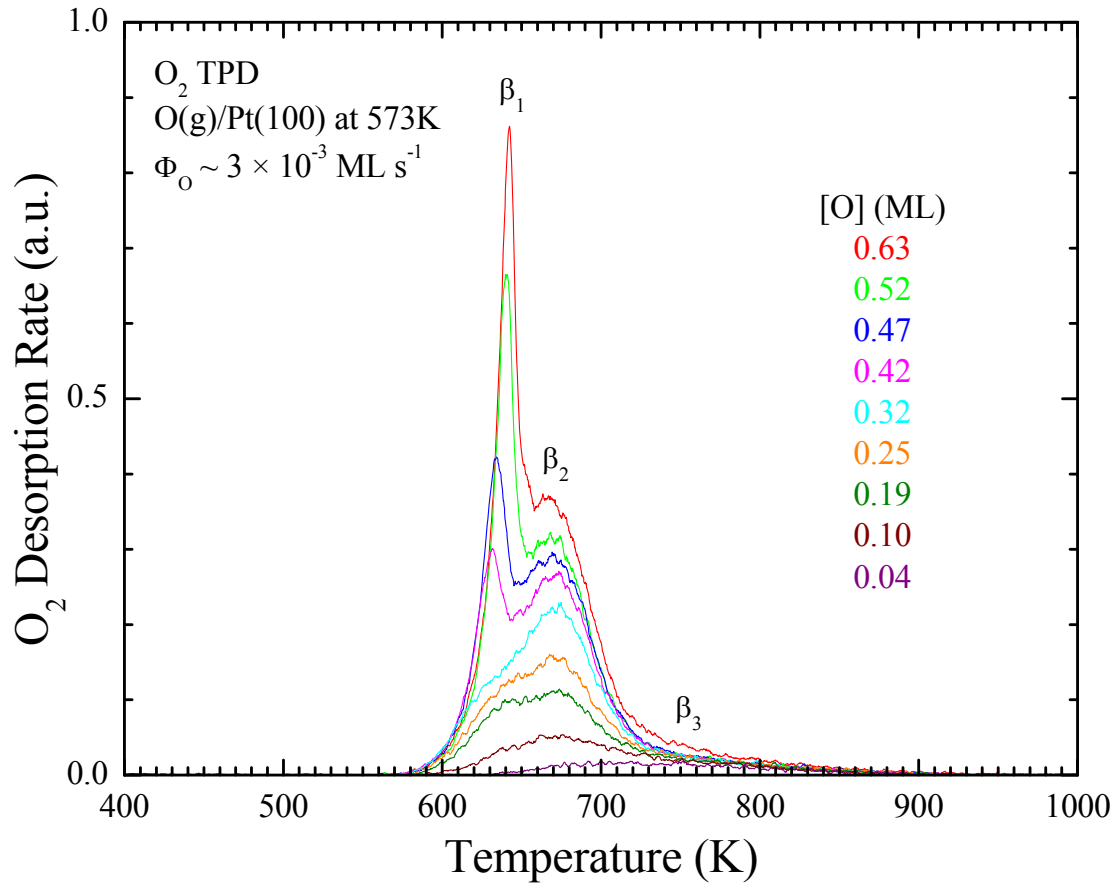


Figure 2-1. O_2 TPD spectra (temperature ramp = 1 K s^{-1}) obtained after exposing Pt(100)-hex- $R0.7^\circ$ at 573 K to an atomic oxygen beam. The initial coverages are 0.04 ML, 0.10 ML, 0.19 ML, 0.25 ML, 0.32 ML, 0.42 ML, 0.47 ML, 0.52 ML, and 0.63 ML.

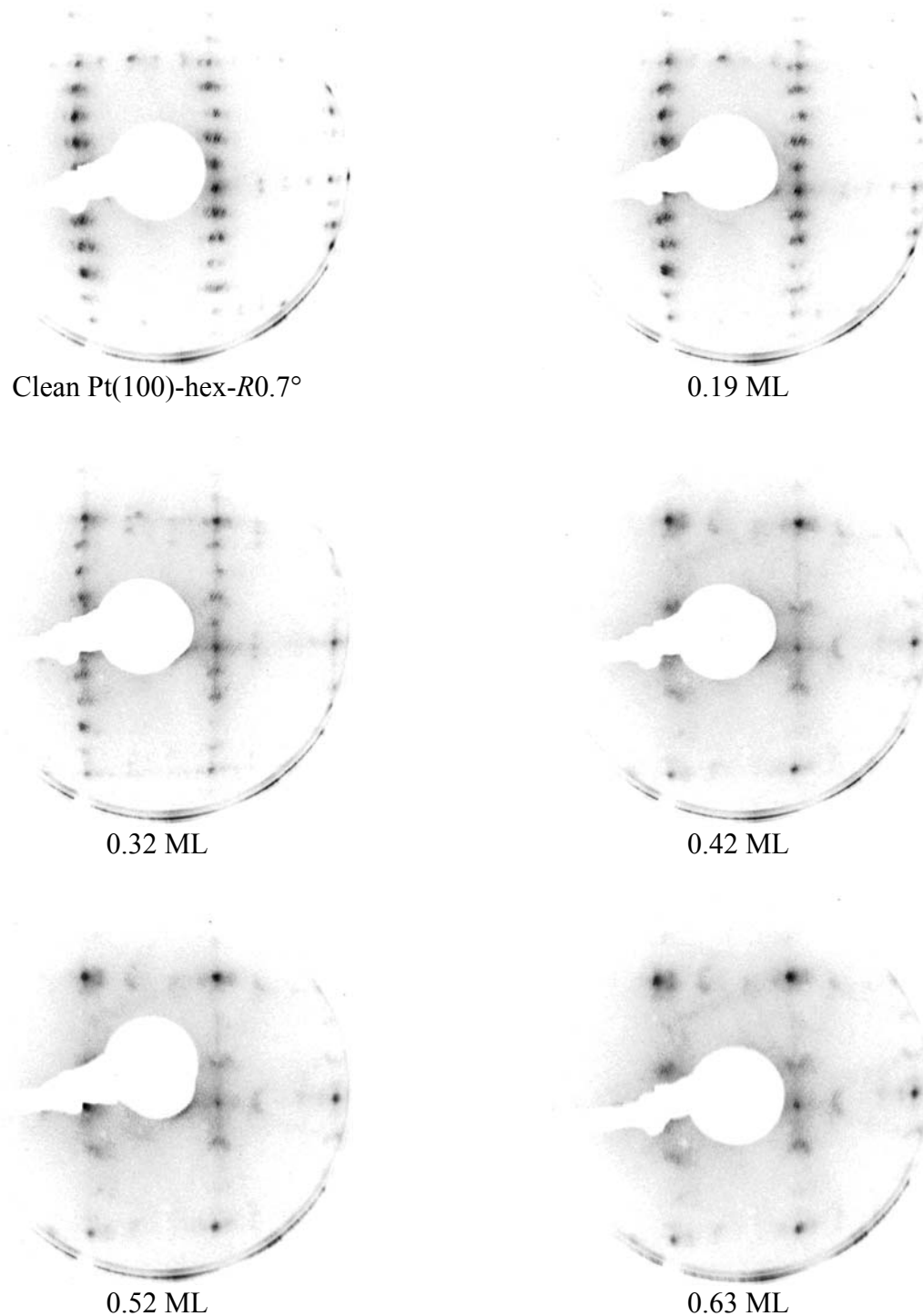


Figure 2-2. LEED images recorded at approximately 80 K after exposing Pt(100)-hex-R0.7° at 573 K to an atomic oxygen beam. The images correspond to a clean surface and coverages of 0.19 ML, 0.32 ML, 0.42 ML, 0.52 ML, and 0.63 ML. Each image was acquired using a primary electron energy of 70 eV.

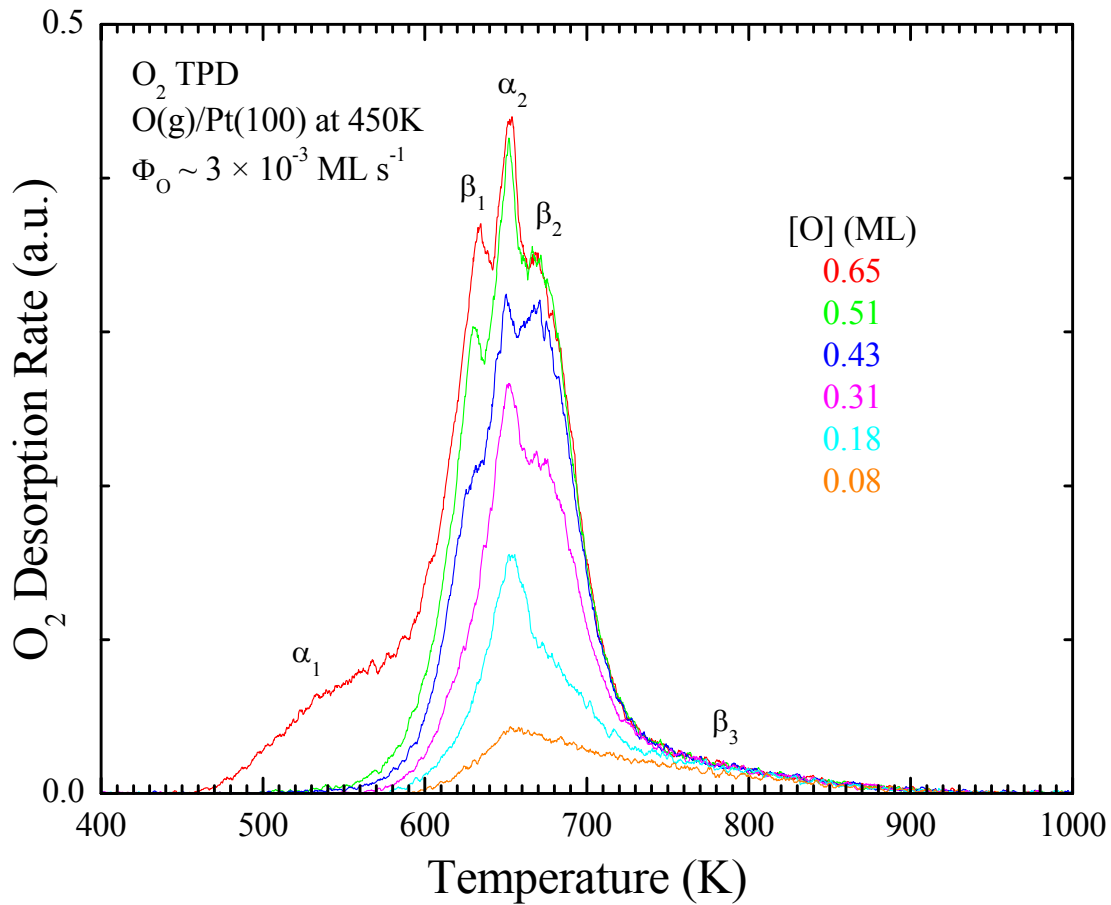


Figure 2-3. O_2 TPD spectra (temperature ramp = 1 K s^{-1}) obtained after exposing Pt(100)-hex- $R0.7^\circ$ at 450 K to an atomic oxygen beam. The initial coverages are 0.08 ML, 0.18 ML, 0.31 ML, 0.43 ML, 0.51 ML, and 0.65 ML. A future investigation will present TPD traces corresponding to higher coverages prepared at 450 K [52]. Note that the y-axis is half the magnitude of the y-axis in Figure 2-1.

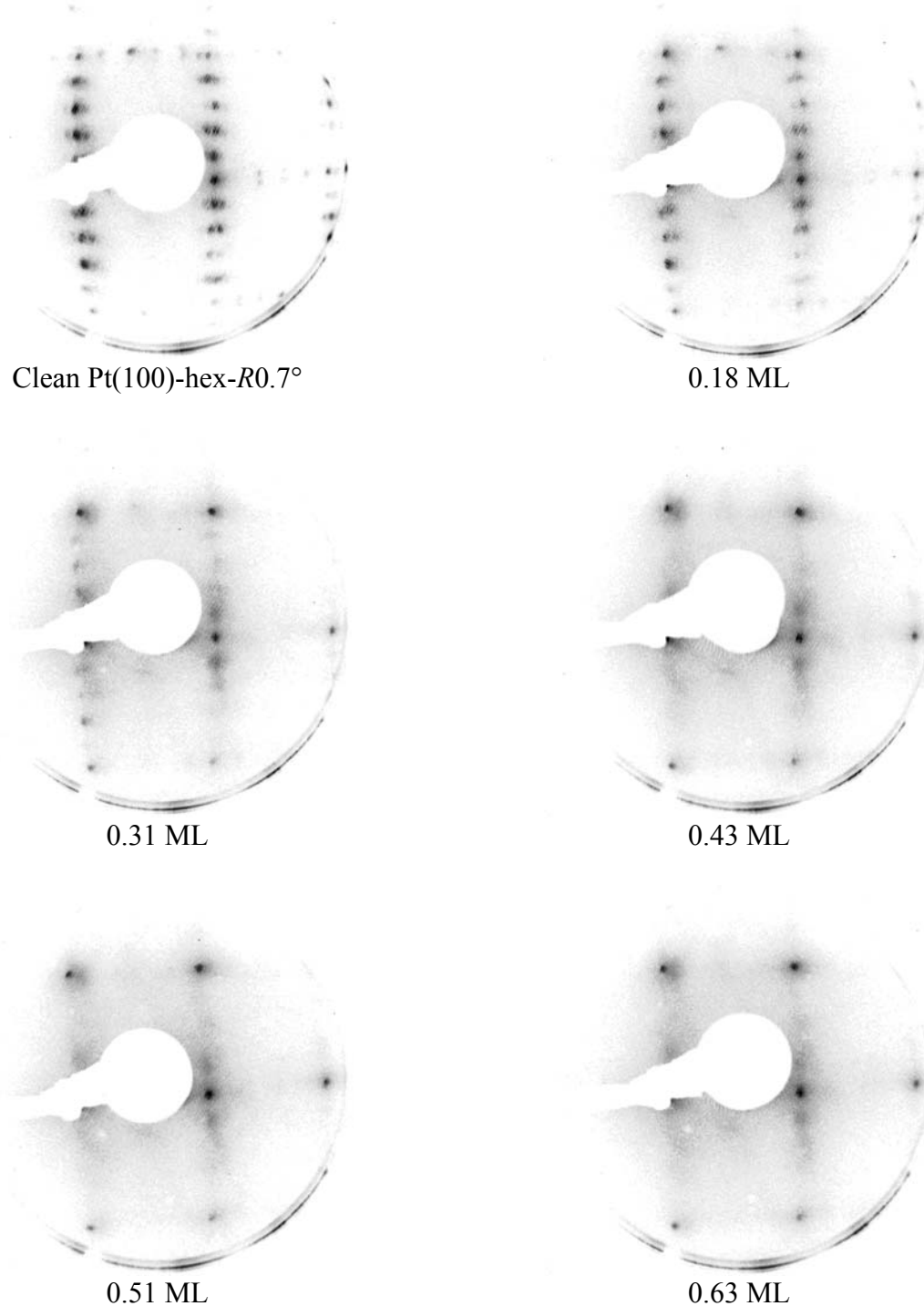


Figure 2-4. LEED images recorded at about 80 K after exposing Pt(100)-hex-R0.7° at 450 K to an atomic oxygen beam. The images correspond to a clean surface and coverages of 0.18 ML, 0.31 ML, 0.43 ML, 0.51 ML, and 0.63 ML. Each image was acquired using a primary electron energy of 70 eV. A future investigation will present LEED images from higher coverages prepared at 450 K [52].

CHAPTER 3 OXIDATION OF Pt(100)-HEX-R0.7° BY GAS-PHASE OXYGEN ATOMS

This chapter reprinted from Surface Science, Volume 601, R.B. Shumbera, H.H. Kan, J.F. Weaver, Oxidation of Pt(100)-hex-R0.7° by gas-phase oxygen atoms, Pages 235-246, Copyright (2006), with permission from Elsevier.

We utilized TPD, XPS, ELS, and LEED to investigate the oxidation of Pt(100)-hex-R0.7° at 450 K. Using an oxygen-atom beam, we generated atomic oxygen coverages as high as 3.6 ML on Pt(100) in UHV, almost 6 times the maximum coverage obtainable by dissociatively adsorbing O₂. The results show that oxidation occurs through the development of several chemisorbed phases prior to oxide growth above about 1 ML. A weakly bound oxygen state that populates as the coverage increases from approximately 0.50 ML to 1 ML appears to serve as a necessary precursor to Pt oxide growth. We find that increasing the coverage above about 1 ML causes Pt oxide particle growth and significant surface disordering. Decomposition of the Pt oxide particles produces explosive O₂ desorption characterized by a shift of the primary TPD feature to higher temperatures and a dramatic increase in the maximum desorption rate with increasing coverage. Based on thermodynamic considerations, we show that the thermal stability of the surface Pt oxide on Pt single crystal surfaces significantly exceeds that of bulk PtO₂. Furthermore, we attribute the high stability and the acceleratory decomposition rates of the surface oxide to large kinetic barriers that must be overcome during oxide formation and decomposition. Lastly, we present evidence that structurally similar oxides develop on both Pt(111) and Pt(100), therefore concluding that the properties of the surface Pt oxide are largely insensitive to the initial structure of the Pt single crystal surface.

3.1 Introduction

Understanding the oxidation of Pt surfaces is fundamentally important to many applications of heterogeneous catalysis, including the oxidation of CO and hydrocarbons in automobile exhausts as well as hydrogen oxidation in fuel cells. Indeed, transition metals and their oxides usually possess very different chemisorptive and reactive properties. As such, predicting catalytic behavior in oxidative environments is challenging without a more complete understanding of the surface properties of Pt oxide and the conditions favoring oxide formation. Furthermore, the oxidation of a metal surface typically involves the growth of surface oxygen phases with properties intermediate to a dilute chemisorbed layer and the bulk oxide. These different types of surface oxygen phases and variations in their populations during reaction could have a significant influence on catalyst performance, providing substantial motivation for investigating the mechanism for Pt oxidation and the properties of the oxygen phases that evolve. Unfortunately, however, UHV studies of Pt oxidation have generally been limited to low coverages due to the relatively low reactivity of Pt surfaces toward O₂. Consequently, a detailed understanding of the oxidation of single-crystal Pt surfaces is still lacking. In this study, we employed an atomic oxygen beam to efficiently generate high oxygen coverages on Pt(100) in UHV and focused on characterizing oxide growth on this surface.

Pt(100) is an intriguing transition-metal surface since it has many thermodynamically favorable structures. On heating bulk-terminated (1×1) Pt(100) above about 400 K, the surface reconstructs into a quasihexagonal arrangement [9,10] through an intermediate (1×5) structure [11]. This quasihexagonal surface exhibits a LEED pattern consistent with a (5×20) or (5×25) structure, but is actually more complex and presently designated as $\begin{pmatrix} 14 & 0 \\ 0 & 5 \end{pmatrix}$ [12] or, more commonly, Pt(100)-hex [13]. Further annealing above approximately 1100 K causes a 0.7°

rotation relative to the underlying bulk-truncated square lattice [13]. Assigned the designation

$\begin{pmatrix} 14 & 1 \\ -1 & 5 \end{pmatrix}$ [12], this reconstruction is commonly labeled Pt(100)-hex- $R0.7^\circ$ [13]. The (1×1) ,

(1×5) , and hex structures are metastable orientations of the Pt(100) surface, while the

thermodynamically favored reconstruction is the hex- $R0.7^\circ$ arrangement.

The interactions of O_2 with Pt(100) have been extensively investigated by surface scientists [14-16,21-27]. However, the low probability for O_2 dissociative chemisorption combined with efficient “clean-off” reactions between adsorbed oxygen atoms and background CO and H_2 has severely limited the range of temperature and oxygen coverage previously explored in UHV. Nevertheless, early studies [15,24-26] show that three states populate during oxygen adsorption on Pt(100)-hex- $R0.7^\circ$ at surface temperatures near 570 K, with each state producing a distinct feature in O_2 TPD spectra. More specifically, oxygen atoms initially bind at defect sites associated with the surface reconstruction up to coverages as high as 0.1 ML, where 1 ML is equivalent to the Pt(100)- (1×1) surface density of 1.28×10^{15} atoms cm^{-2} [9]. Continued adsorption to about 0.32 ML induces local deconstruction and population of an oxygen phase with apparent (3×1) symmetry. Finally, a so-called “complex” ordered phase grows at 573 K until the surface saturates with oxygen atoms at 0.63 ML.

Recently, we reported [68] that exposing Pt(100)-hex- $R0.7^\circ$ to a beam of oxygen atoms at a surface temperature of 573 K yields TPD spectra that are nearly identical to those obtained following the dissociative adsorption of O_2 , supporting the view that the oxygen phases grown on metal surfaces are generally insensitive to the chemical identity of the gaseous oxidant. Interestingly, however, atomic oxygen adsorption at 450 K produces a distinctly different distribution of surface oxygen phases, with a previously unreported metastable phase developing and partially replacing the complex ordered phase that populates at higher temperature. Our

results suggest that formation of the complex phase is kinetically hindered at 450 K and that, consequently, a large fraction of oxygen atoms become trapped in the metastable phase. We also observed a weakly bound oxygen state beginning to populate above about 0.50 ML. In the present study, we show that this oxygen state serves as a necessary precursor to growing surface Pt oxide.

Oxide growth has been examined on Pt(111) [51,69] and Pt(110) [70] in UHV, though no such studies have yet been reported for Pt(100). Saliba et al. [69] recently generated an atomic oxygen coverage of $3.6 \times 10^{15} \text{ cm}^{-2}$ on Pt(111) by using O_3 as the oxidant, observing clear evidence for Pt oxide growth above $1.5 \times 10^{15} \text{ cm}^{-2}$ (~ 1 ML). These workers reported that decomposition of the Pt oxide causes explosive O_2 desorption characterized by a narrow desorption peak that shifts to higher temperature and intensifies dramatically with increasing oxygen coverage; such behavior is indicative of an autocatalytic mechanism for oxide decomposition. By using an atomic oxygen beam, we have also successfully produced Pt oxide on Pt(111) under UHV conditions, finding that the surface saturates at an oxygen coverage of $4.4 \times 10^{15} \text{ cm}^{-2}$ for the incident oxygen-atom flux employed [51]. These results agree well with those reported by Saliba et al. [69] since we also observed explosive O_2 desorption in addition to evidence that the oxide grows as 3D particles and causes significant disordering of the surface. Furthermore, the Pt 4f photoelectron spectra that we recorded suggest that the oxide on Pt(111) is structurally similar to bulk PtO_2 , in agreement with XPS results reported by Parkinson et al. [71]. Interestingly, the decomposition of oxides on Pt(110) also exhibit explosive desorption [70], suggesting similarities in the growth mechanism and stability of oxides on different single crystal Pt surfaces.

3.2 Experimental Methods

Previous studies [1,41,51] provide details of the three-level UHV chamber utilized for the present experiments. The Pt(100) crystal employed in this study is a circular disk (8 mm \times \sim 1 mm) spot-welded to W wires and attached to a copper sample holder in thermal contact with a liquid nitrogen cooled reservoir. A type K thermocouple spot-welded to the backside of the crystal allows sample temperature measurements. Resistive heating, controlled using a PID controller that varies the output of a programmable DC power supply, supports maintaining or linearly ramping the sample temperature from approximately 80 K to 1250 K. Initially, sample cleaning consisted of sputtering with 600 eV Ar⁺ ions at a surface temperature of 800 K, followed by annealing at 1200 K for several minutes. Subsequent cleaning involved routinely exposing the sample held at 800 K to an atomic oxygen beam for several minutes, followed by flashing the sample to 1200 K to desorb oxygen and carbon oxides. We considered the sample to be clean when we could no longer detect contaminants with XPS and could obtain sharp LEED patterns consistent with the Pt(100)-hex-*R*0.7° surface [13].

By partially dissociating pure O₂ (BOC gases 99.999%) in a microwave generated plasma source (Oxford Scientific Instruments), we produce beams that contain approximately 5% oxygen atoms in a balance of O₂ and negligible quantities of impurities. Previous studies [1,41,51] provide convincing evidence that these oxygen-atom beams primarily contain ground-state, neutral species. Furthermore, we estimate that the sample surface experiences a nearly uniform atomic oxygen flux with a lower bound of $\sim 4 \times 10^{12} \text{ cm}^{-2} \text{ s}^{-1}$ ($\sim 3 \times 10^{-3} \text{ ML s}^{-1}$). Following each beam exposure, we analyzed the resulting surface using O₂ TPD, XPS, ELS, or LEED. All TPD measurements began by exposing the sample to the beam at 450 K, followed by cooling the sample to 300 K at a rate of -3 K s^{-1} , facing the sample toward the entrance of a QMS ionizer at a distance of about 10 mm, and increasing the sample temperature by a linear rate of 1

K s^{-1} . Cooling the sample prior to beginning the TPD measurements avoids an initial transient response in the heating by the PID controller, therefore ensuring an approximately linear temperature ramp during the evolution of O_2 . Processing the TPD spectra entailed performing a linear background subtraction followed by smoothing with a 10-point adjacent averaging procedure.

All XPS measurements utilized Al K_α X-rays ($h\nu = 1486.6 \text{ eV}$) with the hemispherical analyzer operating in a retarding mode at a pass energy of 27 eV and the sample normal approximately parallel to the axis of the analyzer. After preparing an oxygen layer, collecting a XPS Pt 4f spectra required about 30 minutes, during which time the prepared layer appeared to remain stable. Most likely, the presence of high oxygen coverages inhibits the adsorption of background CO and H_2 , thereby rendering clean-off reactions by these gases inefficient during the XPS measurements. Processing the XPS spectra included using 21-point Savitzky-Golay smoothing [72], followed by background subtraction using the Shirley method [73]. ELS measurements involved reflecting 500 eV electrons from the surface with the incident and detection angles each set to approximately 30° relative to the surface normal and measuring the energy distribution of scattered electrons with energies as low as 450 eV. ELS measurements also utilized the analyzer operating in a retarding mode at a pass energy of 27 eV. Processing the ELS spectra entailed smoothing using the 21-point Savitzky-Golay filter method [72]. Operating the LEED optics using a primary electron energy of 70 eV and, to avoid field effects from the heating arrangement employed in the study, a sample temperature of approximately 80 K provided the best images when photographed with a digital camera.

3.3 Results

3.3.1 Thermal Desorption of O₂

In an effort to better understand the surface oxygen phase development and the properties of high atomic oxygen coverages that result from exposing Pt(100)-hex-R0.7° to gas-phase oxygen atoms, we performed O₂ TPD measurements following adsorption at a surface temperature of 450 K. Figure 3-1 and Figure 3-2 display the TPD spectra for initial oxygen coverages greater than approximately 0.50 ML obtained after exposing Pt(100)-hex-R0.7° to the atomic oxygen beam at 450 K. Note that the curve resulting from an approximately 1.3 ML covered surface is the highest coverage shown in Figure 3-1 while this same curve is the lowest coverage displayed in Figure 3-2. Scaling the areas under the TPD traces with that obtained from a saturated oxygen-atom layer prepared at 573 K establishes the coverages for each atomic oxygen exposure. Following results from nuclear microanalysis [16], we assume that Pt(100) held at 573 K saturates at an oxygen-atom coverage of 0.63 ML, where 1 ML is equivalent to the Pt(100)-(1×1) surface atom density of 1.28×10^{15} atoms cm⁻² [9]. Recently, we reported [68] TPD spectra for oxygen coverages up to approximately 0.65 ML that result from exposing Pt(100)-hex-R0.7° to gas-phase oxygen atoms at a surface temperature of 450 K. The trace from an oxygen coverage of about 0.51 ML exhibits four main desorption features termed β_1 , α_2 , β_2 , and β_3 corresponding to desorption from a “complex” ordered phase, a high-concentration (1×1) phase, a disordered (3×1) oxygen phase, and from surface defect sites, respectively. As the coverage increases above approximately 0.51 ML, an additional feature, labeled α_1 , appears on the low-temperature side of the β_1 peak. Consistent with the low-temperature oxide precursor phase identified on Pt(111) [51], the α_1 desorption feature continues growing to lower temperatures until desorbing at roughly 550 K at a coverage of about 0.84 ML.

Further increasing the coverage causes the α_1 peak to shift to higher temperatures and eventually cut through the lower coverage desorption traces as the peak desorbs at about 584 K for an initial coverage of approximately 1.3 ML. As the coverage continues to increase, the α_1 feature continues to shift toward higher temperatures while dramatically sharpening and intensifying, giving rise to pronounced autocatalytic or explosive desorption at coverages of about 1.8 ML and higher. Coverages ranging from approximately 1.3 ML to 2.7 ML exhibit particularly pronounced changes in the shape of the desorption traces (Figure 3-2). As the α_1 peak grows and shifts toward higher temperatures, the β_1 and α_2 TPD features also slightly intensify, likely due to peak superposition, until the α_1 state overtakes and passes them. This then causes a decrease in the desorption rate over the temperature range of the original β_1 and α_2 TPD peaks. Saliba et al. [69] reported similar changes in O_2 TPD spectra from high coverages on Pt(111) generated using O_3 , attributing the explosive desorption to the decomposition of small Pt oxide particles. As discussed below, our results are also consistent with oxide particle growth above about 1 ML so the decreasing β_1 and α_2 TPD peak intensities with increasing coverage suggests that these phases are consumed when oxide domains form. However, close inspection of the TPD curves shows that the desorption intensity ranging from about 650 K to 675 K is still significant at the highest initial coverage generated, which may indicate that a small amount of chemisorbed oxygen atoms remains present at high coverages. For atomic oxygen adsorbed on Pt(100), the highest coverage we obtained using gas-phase oxygen atoms is approximately 3.6 ML, characterized by a very sharp desorption feature centered at roughly 693 K with a FWHM of about 11 K. The maximum desorption rate at this coverage is approximately 35 times greater than that exhibited by a coverage of about 0.51 ML prepared at 450 K.

3.3.2 Characterization Using XPS and ELS

In order to better characterize the chemical state changes of Pt and oxygen on the surface as a function of the oxygen coverage prepared at 450 K, we performed XPS and ELS measurements. Figure 3-3 displays the XPS Pt 4f spectra obtained from a clean sample and after preparing the specified oxygen coverages using the atomic oxygen beam. As the coverage increases to about 1.0 ML, the Pt 4f spectra exhibit marginal intensification on the high BE side of the main $4f_{5/2}$ and $4f_{7/2}$ peaks. Further adsorption causes an increase in this high BE spectral intensity as observed for coverages of approximately 1.8 ML and 3.1 ML. Shoulders on the high BE side of the 4f peaks are consistent with Pt oxide formation at coverages greater than roughly 1 ML since bonding in a Pt oxide involves charge transfer from the Pt atoms to the oxygen atoms resulting in Pt cations and oxygen anions. Considering that the O_2 TPD traces begin to exhibit explosive desorption characteristics over this same coverage range, the Pt 4f spectra suggest that Pt oxide begins to form on the Pt(100) surface at coverages greater than approximately 1 ML and that oxide decomposition is responsible for the observed desorption characteristics. This interpretation agrees with previous works [51,69] detailing high oxygen coverages on Pt(111). In the current study, the center of the Pt $4f_{5/2}$ shoulder occurs at a BE of roughly 76.9 eV, identical to the value reported by Weaver et al. [51] and in very good agreement with the value of 76.8 eV reported by Parkinson et al. [71] for oxide formation on Pt(111), pointing to chemical state similarities between the oxides formed on the two surfaces.

Since ELS probes the joint density of filled and empty states near the Fermi level, it is a technique that is very sensitive to the electronic properties of a surface and can serve as a powerful complement to the XPS results. As such, we collected ELS spectra as a function of the oxygen coverage to further characterize changes in the surface electronic structure that accompany oxygen phase development. Figure 3-4 displays the ELS spectra obtained from

Pt(100) as a function of the oxygen coverage prepared at 450 K. The ELS spectrum taken from the clean surface exhibits a sharp loss feature centered at roughly 6.4 eV and broader energy loss features located at about 12.1 eV, 24.5 eV, and 31.6 eV. Consistent with the ELS features observed from Pt and other late transition metals [74,75], we attribute the sharp feature at 6.4 eV to the surface plasmon loss from metallic Pt, the broad feature at 24.5 eV to excitation of the bulk plasmon, and the broad features at 12.1 eV and 31.6 eV to interband transitions between the 5d band and various empty states. Up to coverages of approximately 0.51 ML, the feature corresponding to the surface plasmon loss shifts to about 6.0 eV and slightly decreases in intensity relative to the other features in the spectrum, suggesting that chemisorbed oxygen atoms attenuate the surface plasmon excitation without appreciably altering the metallic properties of the surface. Further increasing the coverage to roughly 1.0 ML causes a more noticeable decrease in the surface plasmon intensity.

As the coverage increases to approximately 1.8 ML, coinciding with Pt oxide formation as deduced from the TPD and XPS results, the relative intensity of the surface plasmon loss continues to decrease while a substantial loss feature centered at about 9.6 eV develops. At a coverage of approximately 3.1 ML, the feature attributed to the surface plasmon loss becomes more difficult to discern while the relative intensity of the feature centered at about 9.6 eV increases and the broad features at 24.5 eV and 31.6 eV appear to merge. Given that XPS provides convincing evidence of Pt oxide at coverages greater than about 1 ML, we attribute the 9.6 eV ELS feature to an energy loss process characteristic of Pt oxide, in close agreement with the feature observed at 9.2 eV for Pt oxide on Pt(111) [51] and consistent with ELS spectra obtained from bulk PdO [74]. Interestingly, the surface plasmon loss feature from metallic Pt is clearly visible even at oxygen coverages as high as about 3.1 ML (arrow in Figure 3-4),

suggesting that relatively large metallic regions remain present at the vacuum-solid interface even after significant amounts of Pt oxide forms. Similar to the findings on Pt(111) [51], this observation supports the interpretation that Pt oxide grows as 3D particles on Pt(100), with the surrounding surface remaining metallic though covered with chemisorbed oxygen atoms.

3.3.3 LEED

Figure 3-5 displays LEED images acquired from Pt(100) as a function of the oxygen coverage generated by adsorption at 450 K. The image taken from clean Pt(100)-hex- $R0.7^\circ$ agrees well with published results [13] and serves as a reference for images captured from the oxygen-covered surfaces. As discussed previously [68], the LEED image obtained at a coverage of about 0.63 ML exhibits a distinct (1×1) pattern with high background intensity that is characteristic of high concentrations of disordered oxygen atoms adsorbed on Pt(100)- (1×1) regions. Furthermore, the intensity within this diffuse pattern appears to be greatest along the $\frac{1}{3}$ -order positions, suggesting contributions from the complex ordered phase (β_1) [68]. Raising the coverage to about 1.0 ML causes a marginal decrease in the intensity of the (1×1) substrate spots and an increase in the background diffusivity with less concentration along the $\frac{1}{3}$ -order positions, indicating that the oxygen adlayer becomes increasingly disordered as the α_1 oxide precursor phase develops. Coinciding with Pt oxide formation on the surface as indicated by TPD, XPS, and ELS, there is a much more dramatic increase in the background diffusivity along with significant blurring of the (1×1) substrate spots at a coverage of approximately 1.8 ML. Finally, further oxide particle growth yields LEED images that only exhibit a diffuse background over total coverages ranging from about 2.7 ML to 3.1 ML.

While the growth of disordered Pt oxide particles on the surface would cause the (1×1) substrate spots to slowly fade, we observe rapid loss of these spots after the formation of only

small amounts of Pt oxide, suggesting significant restructuring of the metal surface even during the initial stages of oxide formation. Weaver et al. [51] reported similar LEED changes associated with high oxygen coverages on Pt(111), attributing their observations to two different possibilities. First, the formation and growth of oxide particles may create dislocations in the metal surface, thereby causing a decrease in the average sizes of the well-defined Pt surface domains. Second, Pt atoms may incorporate into the increasingly disordered chemisorbed phases, effectively hindering diffraction from underlying Pt layers. Although no detailed structural investigation of Pt(100) oxidation exists, STM studies by Zheng and Altman reveal that the development of high oxygen coverages on Pd(111) [76] and Pd(100) [77] involves massive restructuring in which Pd atoms displace from the surface and incorporate into oxidic phases. We suspect that similar structural changes occur during Pt(100) oxidation.

3.3.4 Influence of Surface Temperature

Figure 3-6 shows the coverages obtained as a function of the oxygen-atom beam exposure at surface temperatures of 450 K and 573 K. Multiplying the time of each dose by an incident flux of $3 \times 10^{-3} \text{ ML s}^{-1}$, as estimated from a mass spectrometric analysis of the beam, establishes the amount of oxygen atoms in each exposure. As may be seen in the figure, the uptake curves are quite different with the surface saturating at 0.63 ML for exposures at 573 K and the surface reaching 3.6 ML for exposures at 450 K. Despite this difference in the limiting coverages, the curves show close agreement up to roughly 0.5 ML, suggesting temperature insensitivity of the atomic oxygen adsorption probability. Given that the α_1 desorption feature is centered at approximately 550 K during TPD, these uptake curves are consistent with attributing the α_1 peak to desorption from a necessary oxide precursor state. Since oxygen atoms desorb from the oxide precursor almost immediately upon adsorbing at 573 K, the net rate of adsorption approaches zero as the surface becomes saturated with the complex phase. For exposures at 450 K, oxygen

atoms readily adsorb into the oxide precursor and facilitate Pt oxide growth. Combined with the TPD measurements reported in a previous investigation [68], these results suggest that inhibited oxide precursor formation is the limiting process during the dissociative adsorption of O₂ and chemisorption of gaseous oxygen atoms at 573 K, effectively causing the surface to saturate with the complex phase at 0.63 ML for sufficiently low oxidant fluxes.

3.4 Discussion

We find that the oxidation of Pt(100)-hex-R0.7° involves the development of several phases of chemisorbed oxygen atoms followed by the growth of Pt oxide above a coverage of about 1 ML. We recently reported a study [68] of the evolution and properties of chemisorbed oxygen phases grown on Pt(100)-hex-R0.7° up to about 0.65 ML; therefore, only a brief summary of the pertinent details is given here. As the coverage increases to 0.50 ML at 450 K, oxygen atoms populate a disordered (3×1) phase (β_2), a higher concentration disordered phase (α_2) and a complex ordered phase (β_1). Additionally, performing uptake at higher surface temperature enhances the growth of the complex ordered phase at the expense of forming the α_2 phase, indicating that the α_2 phase is meta-stable and transforms to the complex phase during adsorption at sufficiently high temperature.

3.4.1 Oxide Precursor Phase

The α_1 desorption feature is reported in our prior study [68], but its behavior has not yet been described in detail. This feature first appears in the TPD spectra at about 0.50 ML, intensifying and shifting to lower temperature as the coverage increases to 1 ML (Figure 3-1). A similar feature is observed in O₂ TPD spectra obtained from high oxygen coverages on Pt(111) [51]. Increasing the coverage above about 1 ML then causes the desorption traces to begin undercutting those obtained from lower initial coverages while the α_1 peak starts to vanish and a new desorption feature grows and shifts toward higher temperature (Figure 3-1 and Figure 3-2).

This behavior suggests that the α_1 desorption feature corresponds to a surface oxygen phase or state that is consumed as Pt oxide grows, and is therefore a precursor to the initial formation of Pt oxide domains. Interestingly, Pt oxide does not form during prolonged oxygen-atom exposures above the α_1 peak temperature (Figure 3-6), supporting the conclusion that the α_1 state is a necessary precursor to Pt oxide growth.

The α_1 desorption feature appears to originate from an oxygen state that is distinct from Pt oxide. While an alternative interpretation is that the α_1 desorption feature does not correspond to a new state or phase, but rather to the decomposition of small Pt oxide domains, this interpretation is difficult to rationalize from the data. Firstly, the Pt 4f peaks exhibit clear evidence of Pt oxide only above 1 ML (Figure 3-3). Likewise, increasing the coverage to 1 ML mainly causes attenuation of the surface plasmon peak in the ELS spectra, without producing an obvious increase in the intensity of the oxide loss feature at 9.2 eV. Finally, the coverage range (> 1 ML) at which Pt oxide is first clearly detectable with XPS and ELS coincides with the onset of undercutting in the TPD spectra and a shift of the desorption rate maximum to higher temperature, consistent with a change in the mechanism for desorption. Indeed, the desorption behavior seen above 1 ML is indicative of a self-accelerating or autocatalytic mechanism, whereas the α_1 peak initially exhibits characteristics of second-order desorption, developing as a broad feature that shifts to lower temperature as the coverage increases from about 0.5 ML to 1 ML. Thus, the changes in the XPS and ELS spectra coupled with a distinct change in desorption behavior strongly suggest that Pt oxide grows on Pt(100) only above 1 ML, and therefore that the α_1 desorption feature corresponds to a distinct surface oxygen state that populates at coverages from 0.5 ML to 1 ML.

The exact nature of the α_1 oxygen state is difficult to ascertain from the available data. However, oxygen atoms begin to populate the weakly bound α_1 state only after the high-concentration (1×1) (α_2) and complex (β_1) phases cover a majority of the surface. It is therefore plausible that the α_1 state forms by continued adsorption into either the high-concentration (1×1) or complex phases. Repulsive interactions due to crowding in the high-concentration (1×1) phase or adsorption at a less favorable binding site within this phase may yield a TPD feature that desorbs at much lower temperatures. However, in our previous investigation of chemisorbed oxygen on Pt(100) [68], we reported that the high-concentration (1×1) phase is a precursor to forming the complex phase and that local crowding likely initiates the transformation. It thus seems unlikely that oxygen addition to the high-concentration (1×1) phase would produce a new weakly bound state rather than transforming to the complex phase. Therefore, we speculate that the α_1 state directly results from adding oxygen atoms to the complex phase. To test this hypothesis, we saturated the surface at 573 K with the complex oxygen phase, cooled to 450 K, and continued exposure to the gaseous atomic oxygen source. TPD curves obtained from the resulting surfaces (not shown) exhibit a distinct α_1 feature, along with the sharp β_1 peak representing the complex phase. Furthermore, there was no evidence of the α_2 desorption feature, thus confirming that the α_1 state forms by oxygen addition to the complex phase.

As discussed previously [68], there is significant evidence that the complex phase consists of Pt and oxygen atoms organized in a 2D layer that resides on top of the Pt substrate. Because the complex phase is dense and energetically stable, it is likely that substantial energy barriers must be overcome for oxygen atoms to incorporate into the complex phase and disrupt its structure. Nevertheless, we were able to obtain TPD spectra containing the α_1 feature even after starting with a surface saturated with the complex oxygen phase (not shown). Therefore, we

speculate that the oxide precursor phase (i.e., α_1 state) corresponds to oxygen atoms chemisorbed on top of the complex phase where they coordinate with exposed Pt atoms. Such chemisorption is plausible if Pt and oxygen atoms in the complex phase do in fact reside in the same layer. Oxygen atoms weakly bound on top of the complex phase could certainly desorb as a TPD feature centered at relatively low temperature and follow second-order desorption kinetics. Once the local coverage within the oxide precursor phase surpasses a critical value, surface restructuring initiates and Pt oxide particles begin to nucleate and grow. The initial shift of the α_1 TPD feature toward higher temperature appears to signal the transition to Pt oxide formation at ~ 1 ML.

3.4.2 Pt Oxide Growth and Properties

Platinum oxide begins to grow on Pt(100) above an oxygen coverage of about 1 ML, and approaches saturation at 3.6 ML for the conditions investigated. Moreover, the TPD, ELS and LEED results are consistent with the growth of 3D Pt oxide particles, and disordering of the Pt substrate. We reported very similar behavior in a recent study of Pt(111) oxidation by gaseous oxygen atoms [51], which suggests that common mechanisms govern the oxidation of Pt(100) and Pt(111). Indeed, there is also strong evidence to suggest that the oxides formed on the two surfaces are structurally similar. Most notably, the XPS Pt $4f_{5/2}$ shoulder obtained from oxidized Pt(100) is centered at a binding energy of roughly 76.9 eV (Figure 3-3), identical to the value reported by Weaver et al. [51] and in very good agreement with the value of 76.8 eV reported by Parkinson et al. [71] for oxide formation on Pt(111). These matching values imply that the initial structure of the metallic Pt surface has little influence on the oxide structure that develops. This is certainly plausible considering that the oxides appear to grow as particles on each surface and cause significant loss of the original surface periodicity.

As discussed previously [51], the binding energy of the Pt 4f_{5/2} shoulder lies between the values reported for bulk PtO and PtO₂ [78-80] of 75.6 eV and 77.4 eV, respectively, yet is closer to the binding energy for PtO₂. This may indicate that the surface oxide is structurally similar to PtO₂ but laden with oxygen vacancies or is an intermediate oxide like Pt₃O₄ [4]. However, it is also possible that stoichiometric PtO₂ particles grow on both Pt(111) and Pt(100), but that the Pt 4f photoelectrons appear at slightly lower binding energy than reported for bulk PtO₂ due to more efficient final state screening by the conduction electrons in the nearby metallic substrate. Recently, Penner et al. [81] suggested that a similar final state effect causes differences in the core-level binding energies for PdO in different electronic environments. It is worth noting that the Pt 4f_{5/2} shoulder observed in the current study appears broader than reported for oxidized Pt(111) [51,71], potentially indicating that the oxide structure formed on Pt(100) is more heterogeneously distributed with local regions resembling either the PtO or PtO₂ configurations.

In addition to the similarities observed in the XPS results for Pt(100) and Pt(111), the ELS features that are characteristic of Pt oxide on Pt(100) and Pt(111) are in close agreement. Indeed, we recorded loss features centered at 9.2 eV and 9.6 eV for oxides grown on Pt(111) [51] and Pt(100), respectively (Figure 3-4). The slight difference observed in the two loss features likely results from the heterogeneity of the oxide on Pt(100) as suggested by XPS, but may also be a consequence of dissimilar peak superposition contributions due to differences in the ELS detection angles used during the two studies. Like the XPS and ELS results, there is also remarkable agreement between the oxygen-atom densities within the oxides on Pt(100) and Pt(111) [51]. Specifically, at the highest coverages obtained on Pt(100) and Pt(111), the oxygen-atom densities are approximately 4.6×10^{15} atoms cm⁻² and 4.4×10^{15} atoms cm⁻², respectively. These similar oxygen-atom densities provide further support to the notion that oxides of similar

structure and thickness grow on Pt(100) and Pt(111) and that the oxide growth follows a common mechanism that is largely insensitive to the initial structure of the Pt surface.

Interestingly, our TPD results show remarkable agreement with the TPD spectra obtained by Wagner and Ross from electrochemically oxidized Pt(100) [82]. In their investigation, Wagner and Ross formed anodic films on Pt(100) in 0.3 M HF using a quasi thin-layer electrochemical cell within a vacuum envelope and transferred these surfaces to UHV for study by AES and TPD. The oxidized surfaces generated using this procedure saturated at approximately 2.3 ML, and the O₂ TPD spectra exhibited a sharp primary peak located between approximately 570 K and 630 K, in close agreement with our observations for similar atomic oxygen coverages. In addition, the leading edges and desorption peaks for lower coverages appear at lower temperature than similar desorption rates from more heavily oxidized surfaces as observed in our TPD results. Taken into context, the similarities between the oxides generated electrochemically and using the atomic oxygen source suggest that gas-phase oxygen atoms in UHV effectively reproduce the surface Pt oxides generated under oxidative environments at greater pressures. However, the TPD spectra (Figure 3-2) that we obtained from oxidized Pt(100) are distinctly different than traces obtained from oxygen states, thought to be surface oxides, formed during CO oxidation in the millibar pressure range [50]. In the latter case, the TPD spectra exhibited two relatively broad desorption maxima located at approximately 1020 K and 1160 K, much higher than the peak location of roughly 693 K for the highest oxygen coverage reported in this study. This difference suggests that the chemical states that oxygen atoms populate on Pt(100) are sensitive to the presence of coadsorbates.

3.4.3 Pt Oxide Thermodynamic Stability

The platinum oxide on Pt(100) decomposes explosively during TPD, liberating O₂ in a narrow desorption peak that shifts to higher temperature and intensifies dramatically as the initial

oxygen coverage increases. For an initial coverage of 3.6 ML, the O₂ desorption rate peaks at 693 K in the TPD spectra. Similar behavior is observed during oxide decomposition on Pt(111) [51], though the peak temperature is 750 K for a nearly identical oxygen coverage. To better understand these results, it is useful to first consider the thermodynamics of PtO₂ decomposition. PtO₂ is the most stable Pt oxide and our XPS results suggest its presence on Pt(100). Recall that the decomposition pressure, P_{O_2} , of an oxide is defined by Equation 3-1.

$$\ln\left(\frac{P_{O_2}}{P^0}\right) = \frac{\Delta G_f^0}{RT} \quad (3-1)$$

In Equation 3-1, P^0 is the standard state pressure, ΔG_f^0 is the standard Gibbs free energy for oxide formation per mole of O₂, R is the ideal gas constant, and T is the temperature. Using thermochemical data for bulk PtO₂ [83], we predict $P_{O_2} = 3 \times 10^{-4}$ Torr at 450 K; the decomposition pressure is even higher for bulk PtO at 450 K. This estimate indicates that bulk PtO₂ is thermodynamically unstable at 450 K below an O₂ partial pressure of 3×10^{-4} Torr, and therefore that it should not be possible to produce PtO₂ under the vacuum conditions employed in the present study. Clearly, we can produce a Pt oxide on Pt(100) in UHV and this surface oxide does not begin to decompose appreciably until the temperature reaches about 680 K (Figure 3-2), indicating that the oxide formed on Pt(100) is significantly more stable than bulk PtO₂.

Recently, Campbell [84] presented an insightful model showing that transition-metal oxides possess extra stability as thin films due to adhesion to the metal surface. While our experimental results are consistent with Pt oxide growing as 3D particles, this model affords quantitative estimates of the thermodynamic properties of PtO₂ thin films that aid in determining the origin of the high stability exhibited by the surface Pt oxide that we have produced on

Pt(100) and Pt(111). Campbell shows that the decomposition pressure of an oxide film may be written as Equation 3-2.

$$\ln\left(\frac{P_{O_2}}{P^o}\right) = \frac{\Delta G_f^o}{RT} + \frac{(\gamma_{g/ox} + \gamma_{ox/m} - \gamma_{g/m})}{tN_{ox}RT} \quad (3-2)$$

In Equation 3-2, $\gamma_{g/ox}$, $\gamma_{ox/m}$, and $\gamma_{g/m}$ are the standard surface free energies per unit area of the gas-oxide, oxide-metal, and gas-metal interfaces, respectively, N_{ox} is the number of moles of O₂ per cm³ of an oxide with PtO₂ stoichiometry, and t is the film thickness. For oxides that wet their metals, the quantity $(\gamma_{g/ox} + \gamma_{ox/m} - \gamma_{g/m})$ is negative with values on the order of $-100 \mu\text{J cm}^{-2}$, thus the second term in Equation 3-2 can cause P_{O_2} at a given temperature to be lower for a thin film than for the bulk oxide. It may also be seen that the decomposition pressure decreases as the film thickness decreases; or, in other words, thinner films are more stable.

We estimated the decomposition pressure of a PtO₂ film on Pt metal using available data in order to determine if the extra stability of the surface Pt oxide can be explained solely by the thermodynamics of thin film adhesion. Using the bulk density of PtO₂ of 10.2 g cm^{-3} [85] and the molecular weight of 227.08 g/mol , we calculate that $N_{ox} = 0.0449 \text{ mol O}_2 \text{ cm}^{-3}$. The oxide grown on Pt(100) saturates at a coverage of 4.6×10^{15} oxygen atoms cm^{-2} which is equivalent to $3.74 \times 10^{-9} \text{ mol O}_2 \text{ cm}^{-2}$. Using these values, we estimate the effective PtO₂ film thickness on Pt(100) to be about 0.85 nm . Assuming a value of $-100 \mu\text{J cm}^{-2}$ for the quantity $(\gamma_{g/ox} + \gamma_{ox/m} - \gamma_{g/m})$, we estimate that a 0.85 nm thick PtO₂ film on Pt(100) has a decomposition pressure of approximately $3 \times 10^{-7} \text{ Torr}$ at 450 K . This pressure is 1000 times lower than that predicted for bulk PtO₂, but is still at least two orders of magnitude higher than the O₂ partial pressures in our vacuum chamber at which the surface oxide is stable. Decreasing $(\gamma_{g/ox} + \gamma_{ox/m} - \gamma_{g/m})$ to a value of $-200 \mu\text{J cm}^{-2}$ results in a much lower decomposition pressure, but in this case the PtO₂

film is still predicted to decompose in UHV ($P_{O_2} < 10^{-9}$ Torr) at temperatures near 470 K. These estimates suggest that factors in addition to the changes in surface free energy must significantly contribute in stabilizing the Pt oxide grown on Pt(100) and Pt(111).

Since our experiments suggest the growth of Pt oxide particles, it is instructive to briefly consider the thermodynamics of oxide particle formation. This approach is a generalization of the thin film model presented by Campbell [84]. Consider an oxide particle of volume V_p on a metal surface for which the areas of the gas-oxide and oxide-metal interfaces are $A_{g/ox}$ and $A_{ox/m}$, respectively. The molar Gibbs free energy for oxide particle formation on a metal surface may then be expressed as Equation 3-3.

$$\Delta G_{particle}^o = \Delta G_f^o + A_{ox/m} \frac{(\gamma_{ox/m} - \gamma_{g/m})}{V_p N_{ox}} + A_{g/ox} \frac{\gamma_{g/ox}}{V_p N_{ox}}. \quad (3-3)$$

Notice that Equation 3-3 simplifies to that for a thin film (Equation 3-2) when Equation 3-4 and Equation 3-5 hold.

$$A_{g/ox} = A_{ox/m} \quad (3-4)$$

$$V_p = tA_{g/ox} \quad (3-5)$$

Since the free energy for an oxide-metal interface is typically smaller than that for the gas-metal interface, the second term of the expression is negative and acts to stabilize the oxide particle, whereas the last term is destabilizing. Thus, the stability of a surface oxide is determined by both the surface free energies and the interfacial areas, and can be either higher or lower than the bulk oxide limit. A 2D thin film represents the morphology with the highest stability if one neglects particles that satisfy Equation 3-6.

$$A_{ox/m} > A_{g/ox} \quad (3-6)$$

As discussed above, the extra thermodynamic stability of PtO₂ as a thin film on metallic Pt is significant but is not enough to completely account for the stability observed in the present study.

Furthermore, an oxide thin film will not decompose explosively since the film becomes more stable as its thickness decreases.

Contrastingly, spherical oxide particles are less stable than the bulk oxide since they do not form an interface with the metal (i.e., $A_{ox/m} = 0$), and consequently Equation 3-7 holds.

$$\Delta G_{particle}^{\circ} > \Delta G_f^{\circ} \quad (3-7)$$

This destabilization causes spherical particles to decompose explosively. Specifically, the area to volume ratio increases with decreasing particle size so spherical particles become less stable as they shrink during decomposition. This effect is analogous to the well-known enhancement of the vapor pressure of liquid droplets as their size decreases, as given by the Kelvin equation. Indeed, explosive desorption traces have been interpreted within this context [69,86]. However, since the thermodynamic estimates suggest that a PtO₂ thin film is unstable under the conditions studied, thermodynamics would predict that PtO₂ particles are even less stable and would decompose at much lower temperatures than observed. Importantly, the thermodynamics calculations employ only a single data set for the decomposition of bulk PtO₂ [83] as well as estimates of surface free energies. Despite considerable effort, we could not locate other published thermodynamic data for bulk PtO₂. Additionally, the thermodynamic model presented for oxide particle formation may need to include additional energetic terms such as strain energy [87]. Nevertheless, it is difficult to reconcile both the high stability of the surface oxide and the explosive desorption that is observed by considering only thermodynamics. Thus, while the adhesion of the oxide to the metal likely contributes significantly to the extra stability, we assert that kinetic barriers must also be important in stabilizing the Pt oxide particles that grow on Pt single crystal surfaces.

3.4.4 Oxide Decomposition Kinetics

We have recently presented a kinetic model that reproduces the key characteristics of O₂ explosive desorption observed during oxide decomposition on Pt(111) [51]. This model can also account for the desorption behavior observed in the present study with Pt(100). In this so-called island decomposition mechanism, we assume that oxygen atoms migrate from oxide islands to a more dilute phase of chemisorbed oxygen from which they recombinatively desorb. The model further assumes that desorption directly from the oxide phase is negligible relative to desorption from the chemisorbed phase, and that migration is sufficiently fast to maintain constant oxygen concentrations in each phase while the two phases coexist on the surface. Under these assumptions, the model predicts that the total desorption rate is proportional to the fractional area of the surface covered by the chemisorbed phase, and therefore self-accelerating since the area covered by the chemisorbed phase increases as the oxide decomposes. It is important to recognize that explosive desorption does not result from an intrinsic particle size effect according to the island decomposition mechanism. As such, this mechanism differs fundamentally from the thermodynamic model presented above for an oxide particle.

In applying this model to describe explosive O₂ desorption from oxidized Pt(111), we assumed that the oxide transfers oxygen to only a single, well-defined phase of chemisorbed oxygen atoms. While this assumption is likely an oversimplification considering that several chemisorbed phases populate during adsorption on Pt(111) as well as on Pt(100), the model is intended to approximately represent the desorption mechanism. A more complicated model could be developed that includes desorption and oxygen transfer among multiple phases. It is unclear, however, that such a model will provide new insights for understanding the explosive desorption, or if this approach would even be meaningful given the available data. Indeed, the nature of the chemisorbed phases that coexist with the oxide at high coverages is not known and

may differ from those that populate prior to oxide formation. Specifically, the surface restructuring caused by oxide growth may create different types of surface defects and new, local arrangements of Pt atoms on which oxygen atoms could experience different binding than in the phases that develop prior to oxide formation. Therefore, we are reluctant to develop a more complicated model until more detailed information about the binding states of oxygen at high coverages is obtained, perhaps through STM experiments or quantum chemical calculations. Nevertheless, the good agreement between the simulated and measured TPD curves reported previously [51] supports the conclusion that the island decomposition model captures the essential mechanistic details of Pt oxide decomposition on Pt(111) and Pt(100).

The island decomposition model can also explain the observation that the saturated oxides thermally decompose and desorb at considerably different temperatures on Pt(100) and Pt(111), even though nearly identical amounts of oxide are produced on each surface. At the highest oxygen coverages obtained on Pt(100) and Pt(111), the sharp desorption feature occurs at temperatures of approximately 693 K and 750 K, respectively. After accounting for the different temperature ramp rates utilized in each study, we estimate from Redhead analysis [45] that the effective activation energy for oxygen desorption from an oxide formed on Pt(100) is approximately 17 kJ mol^{-1} lower than from an oxide with nearly the same oxygen-atom density on Pt(111). Thus, the different temperature ramp rates do not fully account for the primary TPD feature desorbing at a lower temperature for Pt(100) than Pt(111), which appears to be inconsistent with the conclusion that structurally similar oxides are formed on these surfaces. However, examining the TPD spectra in the context of the island decomposition mechanism accounts for the lower desorption temperature observed for Pt(100). Indeed, the chemisorbed oxygen phases on Pt(100) [68] desorb about 50 K lower than the chemisorbed phases on Pt(111),

consistent with a lower activation energy for chemisorbed oxygen desorption from Pt(100) than Pt(111). As such, since the island decomposition model suggests that desorption from the chemisorbed phases controls the Pt oxide decomposition rate, it accurately predicts that the explosive TPD feature will occur at a lower temperature for a given oxygen-atom density on Pt(100).

The island decomposition model implies that the activation energy is higher for desorption directly from the oxide than for desorption of chemisorbed oxygen atoms that coexist with the oxide. This means that the surface oxide is more stable against decomposition than are high coverages of chemisorbed oxygen atoms, and therefore that an O₂ molecule must also surmount a larger activation barrier to produce the surface oxide than to chemisorb on the oxygen-covered metal surface. In a prior study [51], we presented estimates of the adsorption energetics that support this interpretation for Pt(111) oxidation. Briefly, the heat of oxygen chemisorption is estimated to fall below that of oxide formation at a coverage lower than that at which the surface oxide is observed. This implies that kinetic barriers restrict oxide growth since the oxide should otherwise form once it becomes the thermodynamically preferred phase. Recently, we have also observed that surface oxide domains are stable on Pt(111) after the coverage is decreased to 0.50 ML by partially reducing an oxidized surface with CO at 500 K [1], whereas oxygen adsorption to a coverage of 0.50 ML produces only chemisorbed oxygen atoms on Pt(111). This result provides additional evidence that kinetic barriers stabilize the surface oxide on Pt(111) since the 0.50 ML of oxygen atoms remaining on the surface would otherwise convert to chemisorbed oxygen atoms.

3.5 Summary

We utilized TPD, XPS, ELS, and LEED to investigate the oxidation of Pt(100) by gas-phase oxygen atoms at a surface temperature of 450 K in UHV. Atomic oxygen coverages as

high as 3.6 ML on Pt(100) were generated using an atomic oxygen beam, thus demonstrating the ability to cleanly prepare high concentrations of atomic oxygen on Pt(100) by exploiting the enhanced reactivity of gaseous oxygen atoms. The results of this investigation show that the oxidation of Pt(100) involves the development of several chemisorbed oxygen phases for coverages up to about 1 ML. A previous investigation [68] details the properties and growth of the different chemisorbed phases on Pt(100). A desorption feature at 550 K is attributed to a weakly bound oxygen state that populates from about 0.50 ML to 1 ML. The inability to oxidize the surface at 573 K shows that population of this state is required to initiate oxide growth. Based on a qualitative assessment of the TPD spectra, this oxide precursor state may correspond to oxygen atoms chemisorbed on top of the complex ordered phase.

Increasing the oxygen coverage above about 1 ML causes growth of Pt oxide particles and significant disruption in the long-range order of the surface. Decomposition of the Pt oxide particles produces explosive O₂ desorption characterized by a shift of the narrow TPD peak to higher temperatures and a dramatic increase in the maximum desorption rate with increasing coverage. At the highest coverage generated of approximately 3.6 ML, the primary desorption peak is centered at about 693 K. This surface oxide is significantly more stable than bulk PtO₂ based on the thermodynamics of bulk oxide decomposition, but the extra stability is difficult to explain by considering only the thermodynamics of oxide particle or thin film formation. Both the high stability and the acceleratory decomposition rates are best explained by concluding that large kinetic barriers must be overcome for the surface oxide to form and therefore to thermally decompose. Lastly, similarities between oxides formed on Pt(100) and Pt(111) [51] support the conclusion that structurally similar oxides form on Pt single crystal surfaces, independent of the initial Pt surface structure.

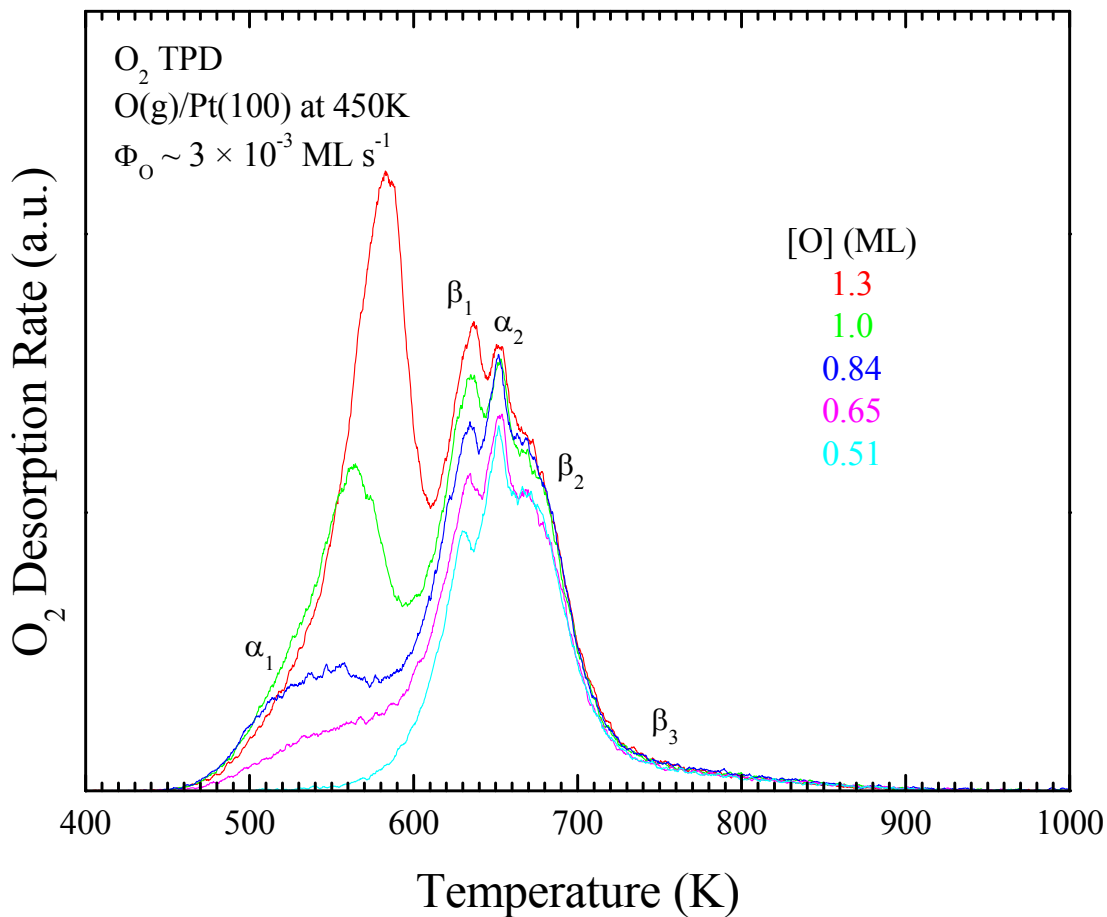


Figure 3-1. O_2 TPD spectra (temperature ramp = 1 K s^{-1}) obtained after exposing Pt(100)-hex- $R0.7^\circ$ at 450 K to an atomic oxygen beam. The initial atomic oxygen coverages are 0.51 ML, 0.65 ML, 0.84 ML, 1.0 ML, and 1.3 ML. TPD traces corresponding to lower coverages prepared at 450 K appear in a previous investigation [68].

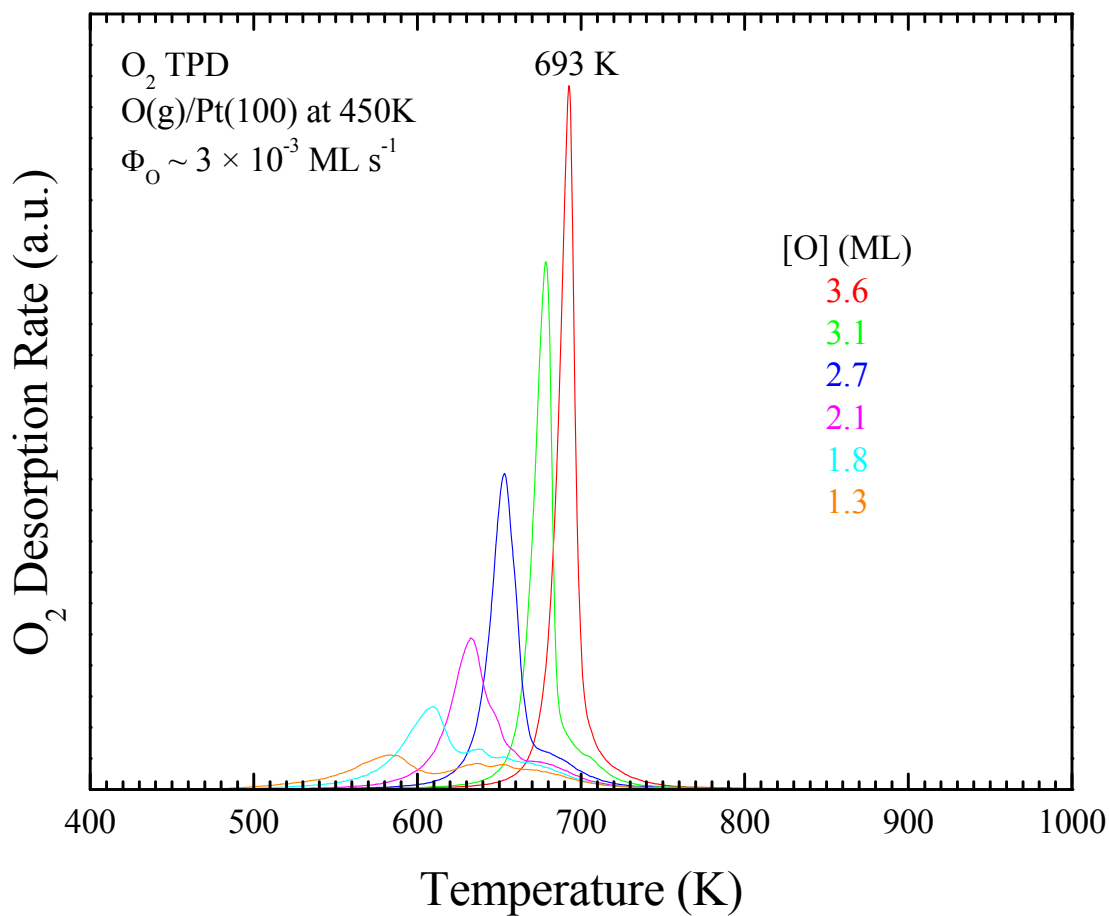


Figure 3-2. O_2 TPD spectra (temperature ramp = 1 K s^{-1}) obtained after exposing Pt(100)-hex- $R0.7^\circ$ at 450 K to an atomic oxygen beam. The initial atomic oxygen coverages are 1.3 ML, 1.8 ML, 2.1 ML, 2.7 ML, 3.1 ML, and 3.6 ML. Note that the curve resulting from an approximately 1.3 ML covered surface is the same as that shown in Figure 3-1.

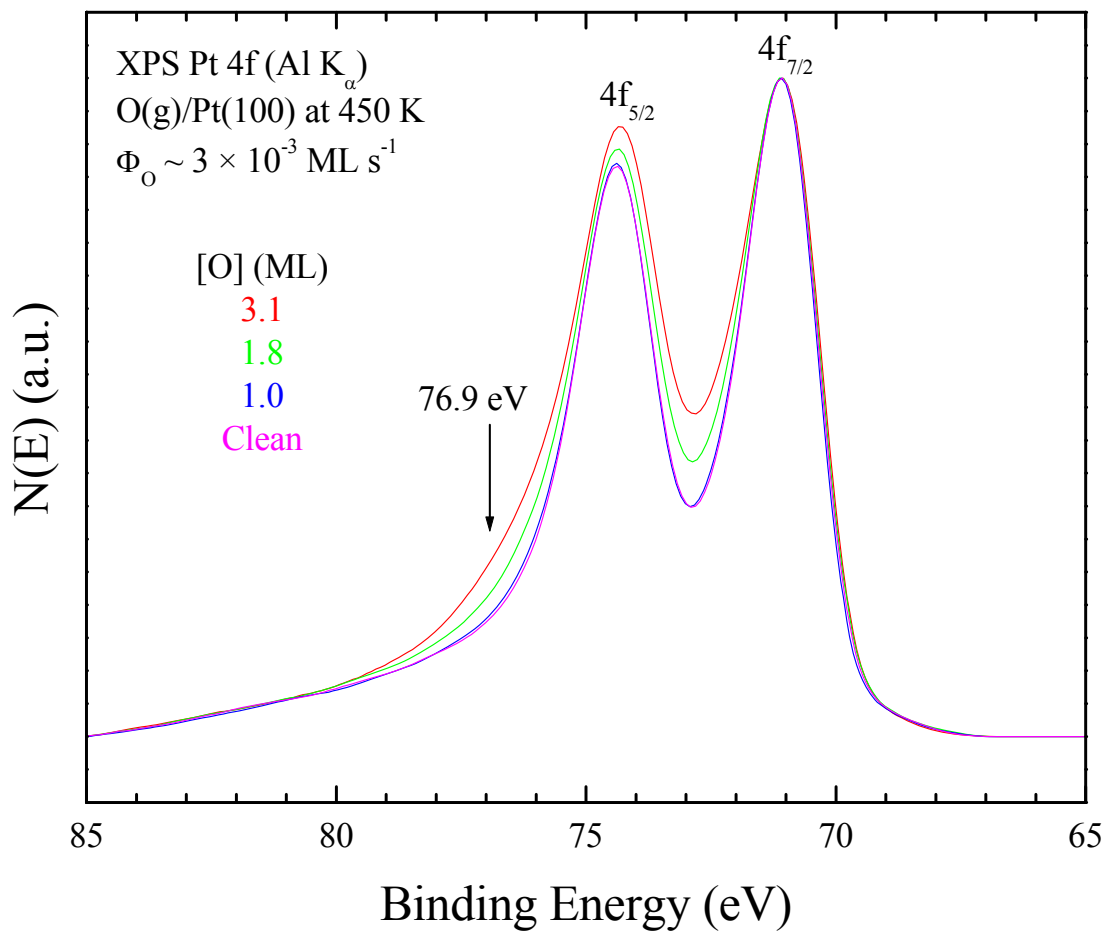


Figure 3-3. XPS Pt 4f (Al K_{α}) spectra obtained after adsorbing atomic oxygen coverages of 1.0 ML, 1.8 ML, and 3.1 ML on Pt(100)-hex- $R0.7^{\circ}$ at 450 K using an oxygen-atom beam. The spectra collected from a clean surface serves as a reference. The broad shoulder at approximately 76.9 eV is indicative of Pt oxide(s).

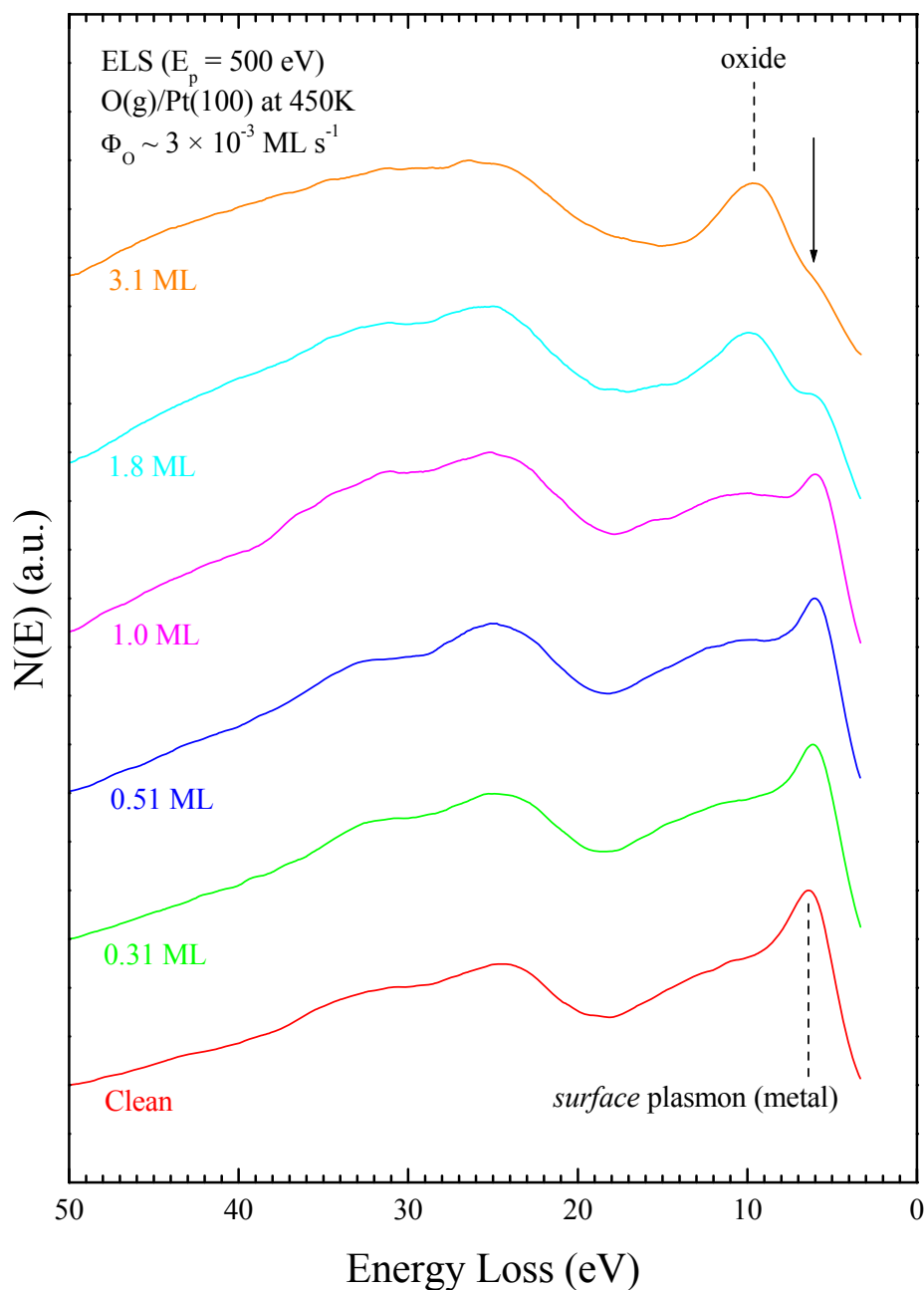


Figure 3-4. ELS spectra obtained using an incident electron energy of 500 eV and incident and collection angles of approximately 30° with respect to the surface normal. The ELS spectra correspond to clean Pt(100)-hex- $R0.7^\circ$ and surfaces prepared by adsorbing 0.31 ML, 0.51 ML, 1.0 ML, 1.8 ML, and 3.1 ML of atomic oxygen at 450 K using an atomic oxygen beam. The major loss features located at approximately 6.4 eV and 9.6 eV are attributed to the surface plasmon loss from metallic Pt and an energy loss process characteristic of Pt oxide, respectively. The arrow points to evidence of the surface plasmon loss feature remaining at 3.1 ML.

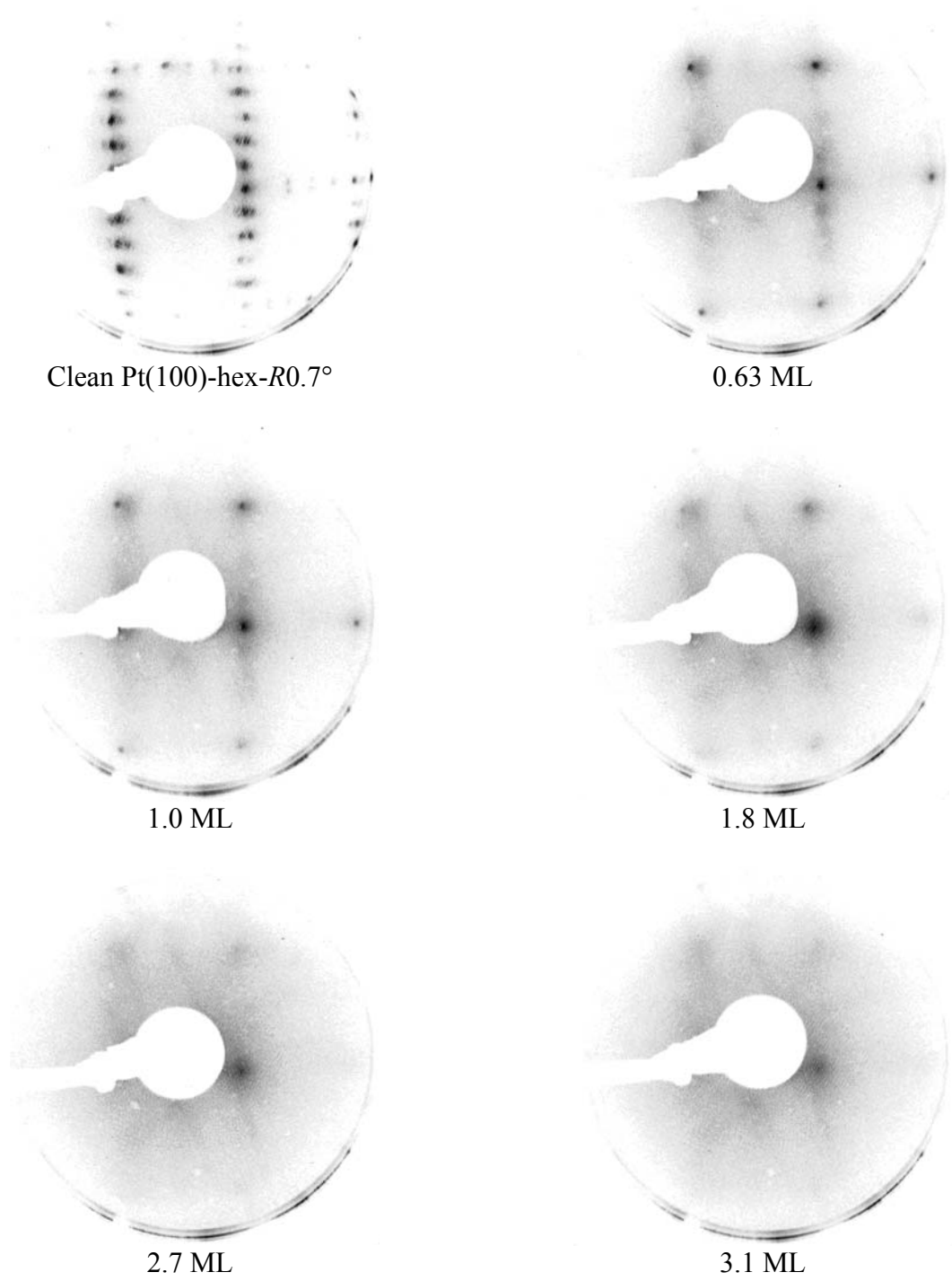


Figure 3-5. LEED images recorded at about 80 K after exposing Pt(100)-hex-R0.7° at 450 K to an atomic oxygen beam. The images correspond to a clean surface and coverages of 0.63 ML, 1.0 ML, 1.8 ML, 2.7 ML, and 3.1 ML. Each image was acquired using a primary electron energy of 70 eV. LEED images corresponding to lower coverages prepared at 450 K appear in a previous investigation [68].

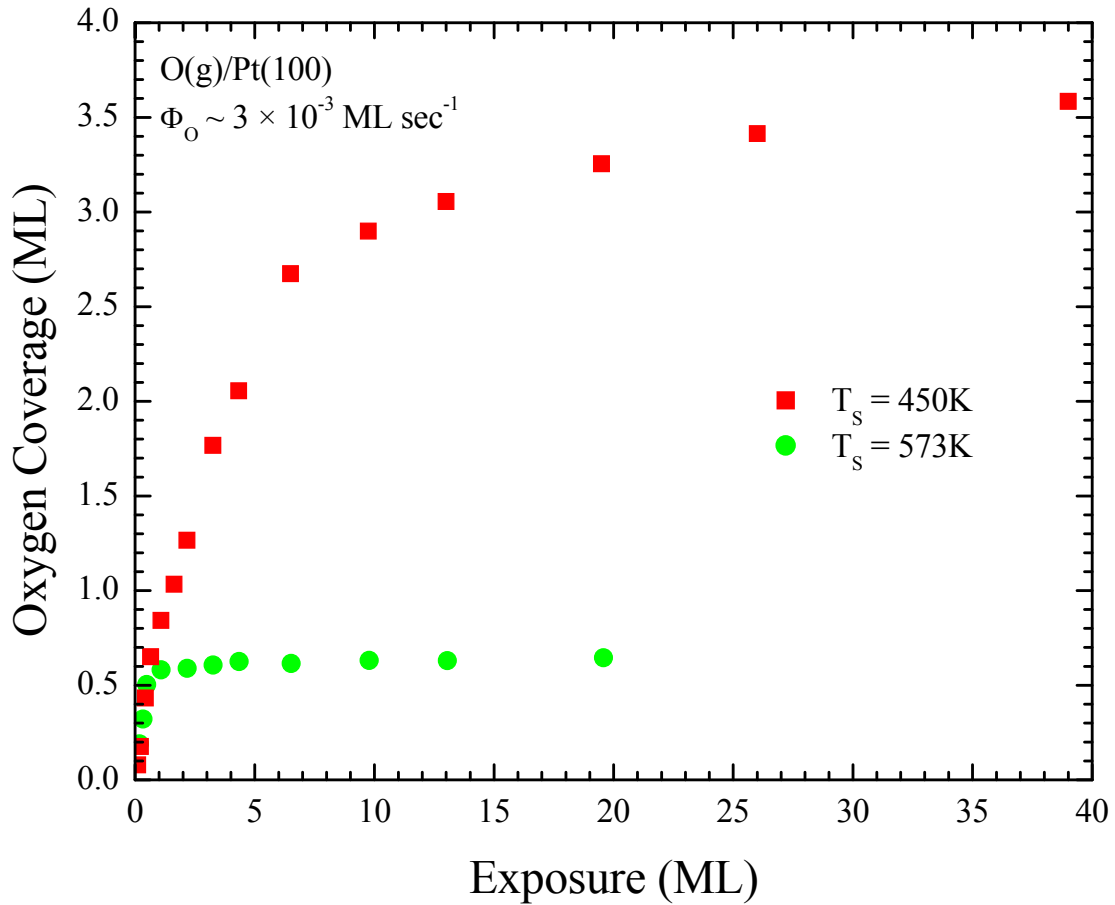


Figure 3-6. Uptake curves obtained by plotting the atomic oxygen coverages generated on Pt(100)-hex-R0.7° at surfaces temperatures of 450K and 573 K as a function of the oxygen-atom beam exposure. Scaling the time of each dose with an incident flux of $3 \times 10^{-3} \text{ ML s}^{-1}$, as estimated from a mass spectrometric analysis of the beam, establishes the amount of oxygen atoms in each exposure.

CHAPTER 4
THE TRANSITION FROM SURFACE TO BULK OXIDE GROWTH ON Pt(100):
PRECURSOR-MEDIATED KINETICS

This chapter reprinted from Surface Science, Volume 601, R.B. Shumbara, H.H. Kan, J.F. Weaver, The transition from surface to bulk oxide growth on Pt(100): Precursor-mediated kinetics, Pages 4809-4816, Copyright (2007), with permission from Elsevier.

We investigated the kinetics governing the transition from surface (2D) to bulk (3D) oxide growth on Pt(100) in UHV as a function of the surface temperature and the incident flux of an oxygen-atom beam. For the incident fluxes examined, the bulk oxide formation rate increases linearly with incident flux (Φ_{O}) as the oxygen coverage increases to about 1.7 ML and depends only weakly on the surface temperature in the limit of low surface temperature ($T_{\text{S}} < 475$ K). In contrast, in the high-temperature limit ($T_{\text{S}} > 525$ K), the bulk oxide formation rate increases with Φ_{O}^2 for oxygen coverages as high as 1.6 ML, and decreases with increasing surface temperature. We show that the measured kinetics is quantitatively reproduced by a model which assumes that oxygen atoms adsorb on top of the 2D oxide, and that this species acts as a precursor that can either associatively desorb or react with the 2D oxide to form a 3D oxide particle. According to the model, the observed change in the flux and surface temperature dependence of the oxidation rate is due to a change in the rate-controlling steps for bulk oxide formation from reaction at low temperature to precursor desorption at high temperature. From analysis of flux-dependent uptake data, we estimate that the formation rate of a bulk oxide nucleus has a fourth-order dependence on the precursor coverage, which implies a critical configuration for oxide nucleus formation requiring four precursor oxygen atoms. Considering the similarities in the development of surface oxides on various transition metals, the precursor-mediated transition to bulk oxide growth reported here may be a general feature in the oxidation of late transition-metal surfaces.

4.1 Introduction

Understanding the oxidation of Pt and other late transition metals is fundamentally important to many commercial applications of heterogeneous oxidation catalysis including fuel processing, remediation of exhaust gases, and selective oxidation of organic compounds. Indeed, the extent of surface oxidation can significantly influence catalytic behavior since transition metals and their oxides typically have quite different chemisorptive and reactive properties. Furthermore, a variety of oxygen phases can exist on transition-metal surfaces that are distinct from a dilute chemisorbed layer and the bulk oxide(s) [88-93]. This intermediate, 2D surface oxide regime is particularly interesting since its development appears to precede the nucleation of 3D bulk oxide particles [51,52,76,77]. Despite the current level of knowledge, however, the transformation from a 2D oxide to 3D oxide particles remains poorly understood. As such, elucidating the atomic-level processes that occur during the transition from surface to bulk oxide growth is key to developing a comprehensive understanding of the oxidation of transition-metal surfaces.

Recently, we utilized oxygen-atom beams to adsorb high concentrations of oxygen on Pt(111) [51] and Pt(100) [52,68] under UHV conditions, characterizing the evolution of oxygen phases that eventually lead to bulk oxide growth. We find that several phases form on these surfaces in an intermediate coverage regime that roughly separates population of a dilute chemisorbed phase from bulk oxide formation. Our results show that at moderate coverages, oxygen atoms adsorb into a high-density, disordered phase on Pt(100) that converts to a “complex” ordered phase. This complex phase appears to be a 2D surface oxide based on similarities between its properties and those that form on Pd and Rh single crystal surfaces [93].

After accumulation of the surface oxide at 450 K, a distinct oxygen state develops on Pt(100) in which the binding is weaker than in the surface oxide and in other phases that exist at

lower coverages. Specifically, the weakly bound state evolves in a broad peak centered at about 550 K in TPD while other states desorb above 630 K. Our experimental data suggests that the weakly bound state corresponds to oxygen atoms adsorbed on top of the surface oxide, and that this species serves as a necessary precursor to bulk oxide particle formation [52]. We base the assignment of this species as a precursor to bulk oxide formation firstly on the observation that the TPD feature arising from the weakly bound state diminishes as a new feature, due to bulk oxide particles, intensifies above coverages of about 1 ML, where 1 ML is equivalent to 1.28×10^{15} atoms cm^{-2} [9]. Additionally, we neither detected oxide particle formation nor precursor population during exposures at 573 K. Rather, for the incident oxygen-atom flux used, the surface effectively saturated at a coverage of 0.63 ML [68], apparently corresponding to the oxygen-atom density within the surface oxide. The measured temperature sensitivity of the oxidation rate is indeed characteristic of a precursor-mediated process for which a kinetic competition exists between desorption of the precursor species and reaction between the precursor and the surface oxide to produce a bulk oxide nucleus.

In the present study, we investigated Pt(100) oxidation as a function of the oxygen-atom incident flux and surface temperature to probe the role of the precursor species in bulk oxide formation. We show that a precursor-mediated model quantitatively describes the kinetics governing the formation of bulk oxide nuclei on Pt(100), supporting our assertion that a precursor mediates the transition from surface to bulk oxide growth. Furthermore, we estimate that the formation rate of a bulk oxide nucleus has a fourth-order dependence on the precursor coverage, implying that a critical configuration of four precursor oxygen atoms initiates nucleation of bulk oxide on Pt(100). The findings of this study may have broad implications

since similar precursor-mediated mechanisms could govern bulk oxide formation on other transition-metal surfaces.

4.2 Experimental Methods

Previous investigations [1,41,43,51] provide details of the three-level UHV system utilized for the present experiments. The Pt(100) crystal employed in this study is a circular disk (8 mm \times ~ 1 mm) spot-welded to W wires and attached to a copper sample holder in thermal contact with a liquid nitrogen cooled reservoir. Sample cleaning initially consisted of Ar⁺ sputtering/annealing cycles, followed by routine exposures at 800 K to an atomic oxygen beam to remove residual carbon and hydrogen.

Connected to the UHV chamber is a two-stage, differentially-pumped chamber that houses a plasma source used to generate beams containing oxygen atoms. In the present study, we achieved higher oxygen-atom incident fluxes than in our previous Pt(100) investigations utilizing a microwave generated plasma source [52,68] by partially dissociating pure O₂ (BOC gases 99.999%) in an inductively-coupled RF plasma source (Oxford Scientific Instruments) described elsewhere [43]. Additionally, we further controlled the atomic oxygen flux by adjusting the distance between the sample and the end of the quartz tube that collimates the beam before entering the UHV chamber. In all cases, the sample was between approximately 25 mm and 50 mm from the terminus of the quartz tube and rotated roughly 45° with respect to the tube axis during exposures to the beam, thus ensuring uniform impingement.

In the present study, all beams were generated using an RF power of 120 W and establishing a gas flow rate that yields a pressure of 3×10^{-6} Torr in the first pumping stage of the beam chamber. In our prior studies using the microwave source [52,68], we used an input power of 125 W and achieved a first stage pressure of 1×10^{-5} Torr. After allowing the plasma to reach steady state, we direct the beam into a QMS and finely adjust the gas flow rate to achieve a

given 16 amu signal intensity, which we relate to the oxygen-atom flux using the calibration procedure described below. Throughout the day, we periodically measure the 16 amu signal intensity and find that the beam flux remains steady to within less than 5%. By reproducing oxygen uptake data, we have also confirmed that the direct 16 amu signal provides a reliable measure of the oxygen-atom beam flux for the experimental conditions that we have employed.

Following each beam exposure, we analyzed the resulting surface using O₂ TPD by first cooling the sample to 300 K, then facing the sample toward the entrance of a QMS ionizer at a distance of about 10 mm, and lastly increasing the sample temperature at a linear rate of 1 K s⁻¹. Scaling the areas under the TPD traces with that obtained by dissociatively chemisorbing O₂ at 573 K until the saturation coverage of 0.63 ML [16] allowed estimating the absolute coverages. Finally, to estimate the fluxes reported in this study, we assumed that the initial probability of a gas-phase oxygen atom to adsorb on the clean Pt(100)-hex-*R0.7°* surface is unity and performed several short beam exposures, ranging from about 5 seconds to 20 seconds, to establish an early uptake curve for each sample position. It then follows that the slopes of the resulting uptake curves give lower bound estimates of the oxygen-atom fluxes. Given the highly reactive nature of gaseous oxygen atoms, assuming an initial sticking probability of unity seems reasonable, especially considering that we calculate very similar values using the same approach with different metal surfaces. Indeed, the linearity of the initial uptake curves reported previously suggest that the sticking probability remains relatively constant regardless of surface temperature and coverage until approximately 0.5 ML [52].

4.3 Results

To determine the influence of the oxygen-atom incident flux on the oxidation kinetics, we first performed TPD measurements following adsorption at 450 K using a flux of approximately 2.7×10^{-2} ML s⁻¹ generated with the RF plasma source. We then compared this data with that

reported in our previous investigation using a flux of about 3.6×10^{-3} ML s^{-1} produced with the microwave plasma source [52]. Figure 4-1a and Figure 4-1b show uptake curves giving the coverage obtained as a function of the beam exposure at a surface temperature of 450 K for the two fluxes investigated. Multiplying the time of each dose by the respective incident flux establishes the amount per unit area of oxygen atoms that strike the sample during each exposure. As seen in Figure 4-1a, the uptake curves show very close agreement for the overlapping coverages (up to about 3.5 ML) generated with these incident fluxes, demonstrating that the uptake curves are flux independent at 450 K. The slope of a coverage vs. exposure uptake-curve is given by Equation 4-1, where $[O]$, ε , R , and Φ_O represent the total coverage, the exposure in ML, the uptake rate, and the O incident flux, respectively.

$$\frac{\partial[O]}{\partial\varepsilon} = \frac{R}{\Phi_O} \quad (4-1)$$

Therefore, the flux independence of the uptake curves suggests that the uptake rate at 450 K depends linearly on the incident flux.

The uptake curves also exhibit regions with distinct slopes, indicating changes in the predominant uptake mechanism(s) at specific coverages. In the expanded view (Figure 4-1a), the uptake rate is initially rapid but decreases considerably after an oxygen coverage of about 2.5 ML. Close inspection also reveals an earlier break in the uptake curves. As seen in Figure 4-1b, the uptake curves are initially linear and then exhibit a sudden decrease in slope at a coverage of approximately 0.60 ML after which the uptake continues to rise linearly but at about 40% of the initially observed rate. The break in linearity in the uptake curves at $[O] \sim 0.60$ ML coincides with the appearance of a low-temperature desorption feature in O_2 TPD that we previously identified as a precursor to bulk oxide formation [52]. The uptake curves remain linear up to a total coverage of about 1.7 ML, but rise more slowly at higher coverage. The linearity of the

uptake curves from $[O] \sim 0.60$ ML to 1.7 ML suggests that a given mechanism controls the oxygen uptake on Pt(100) over the coverage regime at which bulk oxide particles begin to form at 450 K.

Comparing the TPD spectra (not shown) obtained following the higher flux doses with those reported in our previous investigation [52] reveals only slight differences. Most notably, the TPD traces from surface coverages greater than about 3.5 ML prepared with the higher flux exhibit a slight desorption feature on the high-temperature side of the intense, autocatalytic oxide peak. Evolving at roughly 720 K, this small feature is consistent with desorption of less than 0.1 ML subsurface oxygen [59,94,95], suggesting that atomic oxygen uptake on Pt(100) beyond approximately 3.5 ML at 450 K occurs via two pathways. Primarily, continued adsorption causes further oxidation, but small amounts of oxygen are also able to access a secondary pathway whereby subsurface oxygen forms.

We also performed TPD measurements following adsorption at 575 K using fluxes of approximately 2.3×10^{-2} ML s⁻¹ and 3.5×10^{-2} ML s⁻¹ generated with the RF plasma source. We then compared this data with that reported in our previous investigation using a flux of about 3.6×10^{-3} ML s⁻¹ produced with the microwave plasma source [52]. For all three fluxes, the uptake curves increase sharply until 0.63 ML coverage and then exhibit a sudden decrease in slope (Figure 4-2), signaling a change in the uptake mechanism analogous to the behavior observed at 450 K. The slopes of the uptake curves for all three fluxes also show remarkable agreement up to 0.63 ML coverage, but the slopes increase with increasing incident flux above 0.63 ML. Thus, the uptake rate appears to scale linearly with flux at low temperature (450 K), but has a stronger dependence on flux at higher temperature (~ 575 K) beyond the saturation coverage of the 2D oxide.

In our previous investigation detailing oxygen adsorption at 573 K using an incident flux of approximately 3.6×10^{-3} ML s^{-1} [68], we determined that the sample effectively saturates at 0.63 ML, yielding TPD spectra that are similar to traces obtained following O_2 dissociative chemisorption. However, in the present case, we find that higher oxygen-atom fluxes allow for overcoming this apparent saturation limit. Figure 4-3 shows TPD traces obtained following exposures to an incident flux of approximately 3.5×10^{-2} ML s^{-1} from the atomic oxygen beam at 575 K. Interestingly, the TPD measurements show excellent agreement with those previously presented for both oxygen-atom adsorption [68] and O_2 dissociative chemisorption [15,25,26] until 0.63 ML. In these cases, desorption occurs from oxygen adsorbed in the “complex” 2D oxide (β_1), a dilute phase with apparent (3×1) symmetry (β_2), and surface defects (β_3). The structure of the 2D oxide on Pt(100) is not known; however, its characteristics are similar to the surface oxide on Pd(100) which a recent study [90] predicts is a single layer of Pd and oxygen atoms in an arrangement similar to the PdO(101) crystallographic plane. Beyond the apparent saturation coverage, Figure 4-2 shows that the uptake on Pt(100) slows and two additional desorption features simultaneously appear in the TPD spectra (Figure 4-3). One peak is small and evolves at roughly 720 K, while the other is intense and appears to grow from the high-temperature side of the β_1 feature, shifting to higher temperatures with increasing coverage until desorbing at approximately 655 K from a surface covered with 1.6 ML of oxygen atoms. As with the data collected following the 450 K exposures, the small feature is consistent with desorption of less than 0.1 ML subsurface oxygen [59,94,95]. However, XPS, LEED, and ELS measurements are consistent with our prior study of Pt(100) oxidation [52], showing that the more prominent feature arises from bulk oxide particles. Therefore, continued adsorption with higher atomic oxygen incident fluxes at 575 K primarily causes oxide particle formation and

growth, but small amounts of oxygen are also able to access a subsurface state. Interestingly, Norton and coworkers [96] previously observed clear evidence for the formation of oxide at similar high temperatures after exposing Pt(100) to 10^7 L (Langmuir) O_2 .

Finally, we performed experiments to test the influence of the surface temperature on the oxidation kinetics. As seen in Figure 4-4, the coverage obtained following an approximately 124.3 ML exposure generated with a flux of about 3.5×10^{-2} ML s^{-1} increases slightly with increasing surface temperature from 450 K to 475 K. However, the coverage decreases sharply with increasing surface temperature above 475 K. This behavior suggests a change in the rate-limiting step for bulk oxide formation near 475 K, above which the effective activation energy for bulk oxide formation becomes negative; this is a classic sign of precursor-mediated kinetics.

4.4 Kinetic Model and Analysis

The initial formation of bulk-like oxide on Pt(100) appears to occur through a precursor-mediated process involving oxygen atoms adsorbed on top of a 2D oxide [52]. The flux dependence of the uptake curves obtained at fixed temperatures of 450 K (Figure 4-1) and ~ 575 K (Figure 4-2) gives rise to two conditions that a kinetic model for bulk oxide formation must satisfy. First, if the slope of the uptake curve is independent of flux (450 K), then Equation 4-2 holds.

$$\frac{\partial R}{\partial \Phi_O} = \frac{R}{\Phi_O} \quad (4-2)$$

Otherwise, if the slope of the uptake curve increases with increasing flux (~ 575 K), then Equation 4-3 must be satisfied.

$$\frac{\partial R}{\partial \Phi_O} > \frac{R}{\Phi_O} \quad (4-3)$$

In addition, the temperature dependence shown in Figure 4-4 suggests that the expression given in Equation 4-4 holds at relatively low temperatures, where T_S represents the surface temperature.

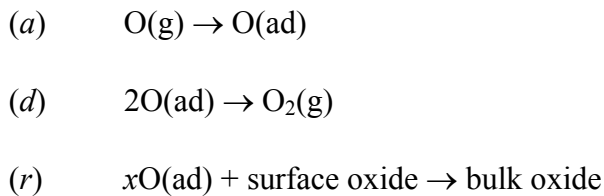
$$\frac{\partial \ln R}{\partial(1/T_S)} \approx 0 \quad (4-4)$$

Likewise, the relationship given by Equation 4-5 is true at higher temperatures.

$$\frac{\partial \ln R}{\partial(1/T_S)} > 0 \quad (4-5)$$

Thus, for the oxygen-atom fluxes studied, the effective activation energy is negative at high temperature and positive, though small, at low temperature. While we obtained only two data points in the low-temperature regime, the model discussed below provides additional support for the condition given in Equation 4-4.

In complying with these conditions, we develop a kinetic description of the initial formation of bulk oxide particles on Pt(100) based on a precursor-mediated mechanism. We emphasize that the intention of this model is only to describe the early stages of 3D oxide formation when the 2D oxide predominantly covers the surface. The following reaction steps represent the proposed precursor-mediated mechanism:



Here, steps (a) and (d) represent the adsorption of a gas-phase oxygen atom into the precursor state and the associative desorption of oxygen atoms from the precursor, respectively. Step (r) represents the reaction between the oxide precursor and the 2D oxide to form a 3D oxide particle.

A mass balance on adsorbed oxygen in the oxide precursor state then gives the time, t , derivative in Equation 4-6.

$$\frac{d\Theta_a}{dt} = r_a - r_d - r_r \quad (4-6)$$

In Equation 4-6, Θ_a is the surface concentration of precursor oxygen and r_a , r_d , and r_r are the rates for steps (a), (d), and (r), respectively, where each quantity is defined for a unit area of the 2D oxide. For the analysis, we describe the adsorption rate of a gas-phase oxygen atom into the precursor state using the expression in Equation 4-7, where S_{2D} is the probability that an incident oxygen atom will adsorb on the 2D oxide in the limit of zero precursor coverage.

$$r_a = \Phi_O S_{2D} \quad (4-7)$$

Equation 4-7 assumes that the adsorption rate is independent of the precursor coverage, which appears to be reasonable based on the linear dependence of the coverage on the beam exposure in the coverage range from about 0.60 ML to 1.7 ML (Figure 4-1b). By assuming that the desorption and reaction rates follow power law forms, the rates for reaction steps (d) and (r) may be written as Equation 4-8 and Equation 4-9, respectively, where k_d and k_r denote the rate coefficients for these reactions.

$$r_d = k_d \Theta_a^m \quad (4-8)$$

$$r_r = k_r \Theta_a^n \quad (4-9)$$

Before comparing the model to experimental data, it is important to recognize that the measured rate of 3D oxide formation represents an integrated quantity over the entire surface. For the proposed model, the measured rate of 3D oxide formation, R_{3D} , may be written as Equation 4-10.

$$R_{3D} = \frac{d[O]_{3D}}{dt} = r_{r,3D} f_{2D} \quad (4-10)$$

In Equation 4-10, $r_{r,3D}$ is the generation rate of oxygen atoms in the 3D oxide per 2D oxide surface area, f_{2D} is the fractional area of the surface covered by the 2D oxide, and $[O]_{3D}$ is the coverage of 3D oxide per total surface area. To facilitate comparisons between the experimental data and the predicted kinetics, we initially assume that f_{2D} remains approximately constant and that the intrinsic rate r_r dominates the kinetics during the early stages of 3D oxide formation. Notice that $[O]_{3D}$ increases linearly in time according to Equation 4-11 if we assume that both $r_{r,3D}$ and f_{2D} are time invariant. We discuss these approximations in more detail below.

$$[O]_{3D} = r_{r,3D} f_{2D} t \quad (4-11)$$

We first consider the kinetics in the low-temperature limit and assume that the precursor coverage reaches a steady value during the early stages of oxide particle formation. To obtain a rate expression for the low-temperature limit, we assume that the oxide formation rate greatly exceeds the rate of precursor desorption, or $r_r \gg r_d$, at low enough surface temperature. This approximation is reasonable given that Pt oxide forms at temperatures as low as 100 K [43], whereas the precursor species desorbs near 550 K in TPD [52,68]. Therefore, in the limit of low temperature, the rates of oxide formation and precursor adsorption are essentially equivalent such that r_r is given by Equation 4-7. As such, the condition given by Equation 4-2 holds for constant f_{2D} , suggesting that the slope of the uptake curve is independent of the incident flux over the regime of initial bulk oxide formation. This is consistent with the condition discussed previously for the uptake curves collected at 450 K and the characteristics observed in Figure 4-1. Moreover, since gaseous oxygen atoms are highly reactive, it is reasonable to assume that S_{2D} depends only weakly on the surface temperature as supported by prior data [52]. Thus, the condition of weak surface temperature dependence (Equation 4-4) is valid in the low-temperature

limit, consistent with the previously discussed conditions and the data presented in Figure 4-4. We note that our prior observation of oxide formation at 100 K [43] suggests that the reaction step also has a very small activation energy. This is consistent with the unactivated place exchange mechanism for initial oxidation advanced in the classic theory of Mott and Cabrera [97-99].

According to our precursor-mediated model, the uptake curve in the low-temperature limit should depend linearly on the oxygen exposure, increasing with a slope equal to S_{2D} , for coverages corresponding to initial bulk oxide formation. The dashed line in Figure 4-1b shows that for coverages from about 0.60 ML to 1.7 ML the uptake curve is very well approximated by a line with a slope of $S_{2D} = 0.42$. Note that the uptake below about 0.50 ML is also linear (solid line), and that we use this initial linear uptake to estimate the oxygen-atom incident flux assuming an initial adsorption probability of $S_0 = 1$ in this coverage range. Within the context of the model, the smaller slope in the region above $[O] \sim 0.60$ ML indicates that the atomic oxygen adsorption probability on the 2D oxide is lower than on the metal. This suggests that energy dissipation is less efficient during oxygen-atom collisions with the 2D oxide, resulting possibly from a shallower well depth for the oxygen atom-2D oxide interaction and/or smaller corrugation in the interaction potential.

Turning focus to the high-temperature limit, we can assume that at high enough surface temperature, the rate of precursor associative desorption will become much greater than the oxide formation rate, or $r_d \gg r_r$. Since the TPD feature attributed to precursor desorption occurs at approximately 550 K [52,68], the uptake data collected at ~ 575 K should fall within this regime. In this case, we have that the adsorption and desorption rates are essentially equivalent at steady state. Therefore, we obtain the relationships given by Equation 4-12 and Equation 4-13.

$$\Theta_a \approx \left(\frac{\Phi_O S_{2D}}{k_d} \right)^{1/m} \quad (4-12)$$

$$r_r \approx k_r \left(\frac{\Phi_O S_{2D}}{k_d} \right)^{n/m} \quad (4-13)$$

Imposing the earlier requirement of Equation 4-3 leads to the constraint that $n > m$. Furthermore, it is possible to estimate n/m from the data by noticing that Equation 4-14 is true for constant f_{2D} , where $[O]_{3D}$ is estimated as the total coverage less the saturation value for the surface oxide of 0.63 ML [16], and the derivative performed at constant exposure time and surface temperature (575 K).

$$\left(\frac{\partial \ln [O]_{3D}}{\partial \ln \Phi_O} \right)_{t, T_s} = \frac{n}{m} \quad (4-14)$$

After analyzing the data, we predict that the ratio $n/m \approx 2$. Thus, if the desorption of precursor oxygen atoms follows second-order kinetics as suggested in our previous text [52], then $n \approx 4$ and the condition $n > m$ holds.

Determining that $n \approx 4$ is interesting since it may relate to the reactive configurations of adsorbed oxygen atoms as well as the critical size of 3D oxide nuclei. Specifically, if oxygen atoms randomly occupy sites on the 2D oxide surface, then the probability of finding four oxygen atoms adsorbed on nearest neighbor sites is proportional to Θ_a^4 . Thus, the dependence of the reaction rate on Θ_a^4 suggests that formation of a 3D oxide particle occurs primarily in adsorbate configurations containing four nearest neighbor oxygen atoms. One might envision the reaction as involving concerted repositioning of four nearest-neighbor adsorbed oxygen atoms and Pt and oxygen atoms of the 2D oxide to produce a 3D oxide cluster, possibly with PtO_2 stoichiometry as suggested previously [52]. A possible explanation for the fourth-order

dependence is that reaction of a four-atom adsorbate configuration and the 2D oxide produces a 3D oxide cluster of the minimum size required for stability. In this case, local configurations with less than four adsorbed oxygen atoms would make a negligible contribution to the reaction rate since they would produce unstable 3D oxide clusters that rapidly dissociate back to the 2D oxide. Interestingly, a recent computational study [100] predicts significant differences among the relative stabilities of oxidized Pt clusters, particularly among clusters containing less than five Pt atoms.

Given $n/m \approx 2$, it is possible to estimate effective rate parameters from the temperature dependent data shown in Figure 4-4. Assuming an Arrhenius form for the rate coefficients k_d and k_r , the effective pre-exponential factor and activation energy for oxide particle formation are given by v_r/v_d^2 and $(E_r - 2E_d)$, respectively, in the high-temperature limit. Here, v_r and E_r represent the pre-exponential factor and activation energy for step (r), while v_d and E_d are the pre-exponential factor and activation energy for step (d). Likewise, the expression for r_r can be rewritten as Equation 4-15.

$$r_r = \left(\frac{v_r}{v_d^2} \right) (\Phi_{\text{O}} S_{2D})^2 \exp \left[\frac{-(E_r - 2E_d)}{RT_s} \right] \quad (4-15)$$

To analyze the temperature dependent data, we firstly assume that reaction (r) consumes one precursor oxygen atom for every two oxygen atoms generated in the 3D oxide so that $r_{r,3D} = 2r_r$. This stoichiometry is consistent with one mole of adsorbed oxygen reacting with one mole of PtO to produce one mole of PtO₂. We further assume that the 2D oxide covers the entire surface at the onset of 3D oxide formation and that the fractional area of the 2D oxide remains approximately constant as the 3D oxide develops, which gives $f_{2D} = f_{2D,0} \sim 1$, where $f_{2D,0}$ is the initial value of f_{2D} . The assumption of constant f_{2D} may be reasonable for the coverage of 1.2 ML obtained at 575 K, but is certain to be invalid for the higher coverages of 4.9 ML and 2.4 ML

obtained at 525 K and 550 K, respectively (Figure 4-4). We nevertheless proceed with the analysis but consider the rate parameters estimated from this data as approximate.

For the approximations considered, the total 3D oxide coverage is given by the expression in Equation 4-16, where ε_0 is the exposure at which the 3D oxide begins to form.

$$[\text{O}]_{3\text{D}} = \frac{2r_r f_{2\text{D},0} (\varepsilon - \varepsilon_0)}{\Phi_{\text{O}}} \quad (4-16)$$

Writing Equation 4-16 for an Arrhenius construction gives Equation 4-17, where the high-temperature form of the rate equation is explicitly included.

$$\ln[\text{O}]_{3\text{D}} = \ln \left[\frac{2v_r f_{2\text{D},0} (\varepsilon - \varepsilon_0)}{\Phi_{\text{O}}} \left(\frac{\Phi_{\text{O}} S_{2\text{D}}}{v_d} \right)^2 \right] - \frac{(E_r - 2E_d)}{RT_{\text{S}}} \quad (4-17)$$

From a plot of $\ln[\text{O}]_{3\text{D}}$ vs. T_{S}^{-1} for the high-temperature data shown in Figure 4-4, and using $S_{2\text{D}} = 0.42$, we estimate that $(E_r - 2E_d) = -102.6 \text{ kJ mol}^{-1}$ and $v_r/v_d^2 = 1.8 \times 10^{-10} \text{ s ML}^{-1}$. With these parameters, Equation 4-15 predicts the dashed lines shown in Figure 4-2 for each of the incident fluxes investigated at $\sim 575 \text{ K}$. The predictions show very good agreement with the experimental data, overestimating the data by at most 15% at the longer exposures examined. This overestimation of $[\text{O}]_{3\text{D}}$ is expected because the total rate should decrease with increasing coverage due to consumption of the 2D oxide, which the analysis neglects. Overall, the agreement is quite good considering the approximate nature of the analysis.

Since a key approximation made in the data analysis is that the fractional area of the 2D oxide remains constant during the early stages of bulk oxide formation, it is useful to consider in more detail the effect that 2D oxide consumption could have on the oxidation kinetics. As an extreme case, we first assume that only reaction (r) affects the total 2D oxide coverage and hence

that the fractional 2D oxide area decreases with time according to Equation 4-18, where Θ_{2D} , the oxygen density within the 2D oxide, is assumed constant at 0.63 ML.

$$f_{2D} = f_{2D,0} \exp\left[\frac{-r_r t}{\Theta_{2D}}\right] \quad (4-18)$$

A linear approximation of Equation 4-18 is reasonable for $t \ll \Theta_{2D}/r_r$, and results in the expression given by Equation 4-19 for the time evolution of the 3D oxide coverage.

$$[O]_{3D} = 2r_r f_{2D,0} t \quad (4-19)$$

Notice that Equation 4-19 is the same as that obtained assuming that f_{2D} is time invariant (Equation 4-11), but here we find that the approximations leading to the $[O]_{3D}$ equation are less stringent. In particular, the linear approximation is reasonable when the exposure time is much shorter than the characteristic time for reaction. Using the rate parameters derived from the data, we estimate characteristic reaction exposures, or $\Phi_O \Theta_{2D}/r_r$, of about 135 ML and 195 ML for oxidation at 575 K and fluxes of $3.5 \times 10^{-2} \text{ ML s}^{-1}$ and $2.3 \times 10^{-2} \text{ ML s}^{-1}$, respectively. Similarly, we estimate a characteristic reaction exposure of about 1.5 ML for oxidation at 450 K. As seen in Figure 4-1b and Figure 4-3, the data agrees well with the predicted lines below the characteristic exposures, suggesting that the linear approximation is indeed reasonable over those ranges of exposure and coverage.

It is also instructive to consider how regeneration of 2D oxide domains during the initial formation of 3D oxide could influence the oxidation kinetics. Regeneration of 2D oxide is plausible if the local density of the 3D oxide is greater than that of the 2D oxide. For example, if reaction between the precursor and the 2D oxide produces a single α -PtO₂ trilayer with the favored (0001) surface orientation [5], then the local oxygen density of the 3D oxide is $\Theta_{3D} = 1.76 \text{ ML}$. For the oxygen stoichiometry stated above, we estimate that the 3D oxide would

occupy about 70% of the area covered by the 2D oxide, suggesting that bare metal covers the remaining 30% immediately after 2D to 3D oxide conversion. This is a significant decrease in the oxygen-covered surface area. Oxygen atoms from the gas-phase are certain to adsorb rapidly on newly generated metallic domains, where they likely produce new domains of 2D oxide. Generation of new 2D oxide domains would mean that the fractional area covered by the 2D oxide decreases more slowly than predicted by the exponential decay discussed above, providing further support of the approximations employed in the data analysis and suggesting that the model is accurate over a moderate range of coverage beyond the onset of bulk oxide formation.

While the precursor-mediated mechanism explains the data rather well, a few issues require further investigation. Firstly, the exact nature of the precursor state is not fully resolved. Based on extensive TPD, XPS and ELS data as well as logical arguments [52], we previously attributed the precursor state to oxygen atoms adsorbed on top of the 2D oxide. However, experiments or computations that can more directly probe this state are necessary to provide a more stringent test of our interpretation. In addition, the fourth-order dependence of the oxide formation rate on the precursor coverage assumes that desorption of precursor oxygen atoms is a second-order process. Analysis of O₂ TPD spectra to determine the order of desorption for this state is complicated because it requires knowledge of the *local* oxygen coverage within the low-temperature state, which in principle depends on the fraction of the surface covered by the 2D oxide. Since the amount of 2D oxide continues to increase slightly as the precursor state populates [52], the local coverage within the precursor state cannot be simply equated with the area of the low-temperature desorption feature. However, we consistently find desorption orders greater than unity when the analysis assumes that the amount of 2D oxide continues to increase as the low-temperature state initially appears. This finding supports the logical conclusion that

desorption of the precursor state is second-order, but we emphasize that the desorption order is difficult to determine accurately from the available data. As such, we consider the conclusion that the oxide formation rate is fourth-order in the coverage of precursor oxygen atoms as approximate.

Despite these complications, the precursor-mediated mechanism describes the data accurately over a wide range of conditions, and provides a simple model for understanding the rate processes that govern the initial transition from surface to bulk oxide growth on Pt(100). Interestingly, previous TPD data suggests that a precursor state also populates on Pt(111) prior to the growth of bulk oxide particles [51]. We have also recently observed O₂ TPD spectra from Pd(111) that are qualitatively similar to those reported for oxygen-covered Pt(100) in that a low-temperature peak grows and then diminishes as a sharp feature due to bulk-like PdO appears. Indeed, these similarities suggest that the precursor-mediated mechanism for initial bulk oxide formation is a general characteristic of the oxidation of late transition-metal surfaces.

4.5 Conclusions

In this work we demonstrated that the kinetics governing the transition from surface to bulk oxide growth on Pt(100) is well-described within the context of a precursor-mediated mechanism with oxygen atoms adsorbed on top of the surface oxide acting as the precursor species. In the limit of low surface temperature, the model predicts that the oxidation rate is approximately equal to the adsorption rate on the 2D oxide, and hence that the oxidation rate depends linearly on the incident oxygen-atom flux and only weakly on the surface temperature. At sufficiently high surface temperature, a quasi-equilibrium between adsorption and desorption establishes the precursor coverage. In this limit, we find that the oxidation rate depends on the incident flux to the power of two, and follows an Arrhenius dependence on the surface temperature with a negative, apparent activation energy. From the measured flux dependence, we

estimate that the rate of initial bulk oxide formation has a fourth-order dependence on the coverage of precursor oxygen atoms, implying that a critical configuration of four oxygen atoms initiates oxide nucleus formation on the Pt(100) surface. This work is the first to report a model based on a precursor-mediated mechanism that quantitatively reproduces the kinetics of bulk oxide formation on a transition-metal surface. Given that surface oxides are also known to precede bulk oxide growth on the (111) and (100) surfaces of Pd and Rh [89-93], precursor-mediated kinetics may be a general feature in the initial formation of bulk oxides on late transition-metal surfaces.

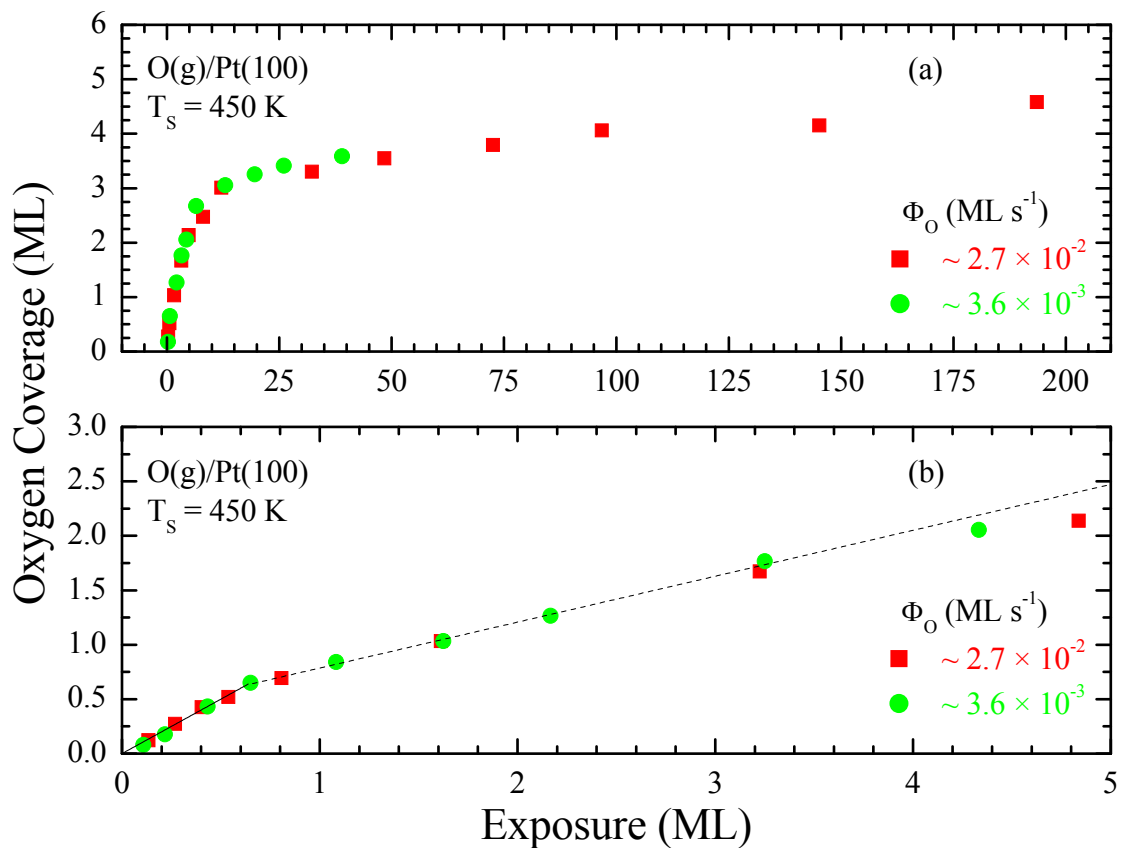


Figure 4-1. (a) Uptake curves showing the coverages generated on Pt(100) at 450 K as a function of the oxygen-atom exposure for different incident fluxes, and (b) a close-up view of the uptake curves for exposures up to 5 ML. The solid and dashed lines represent linear fits to the data over the coverage ranges discussed in the text.

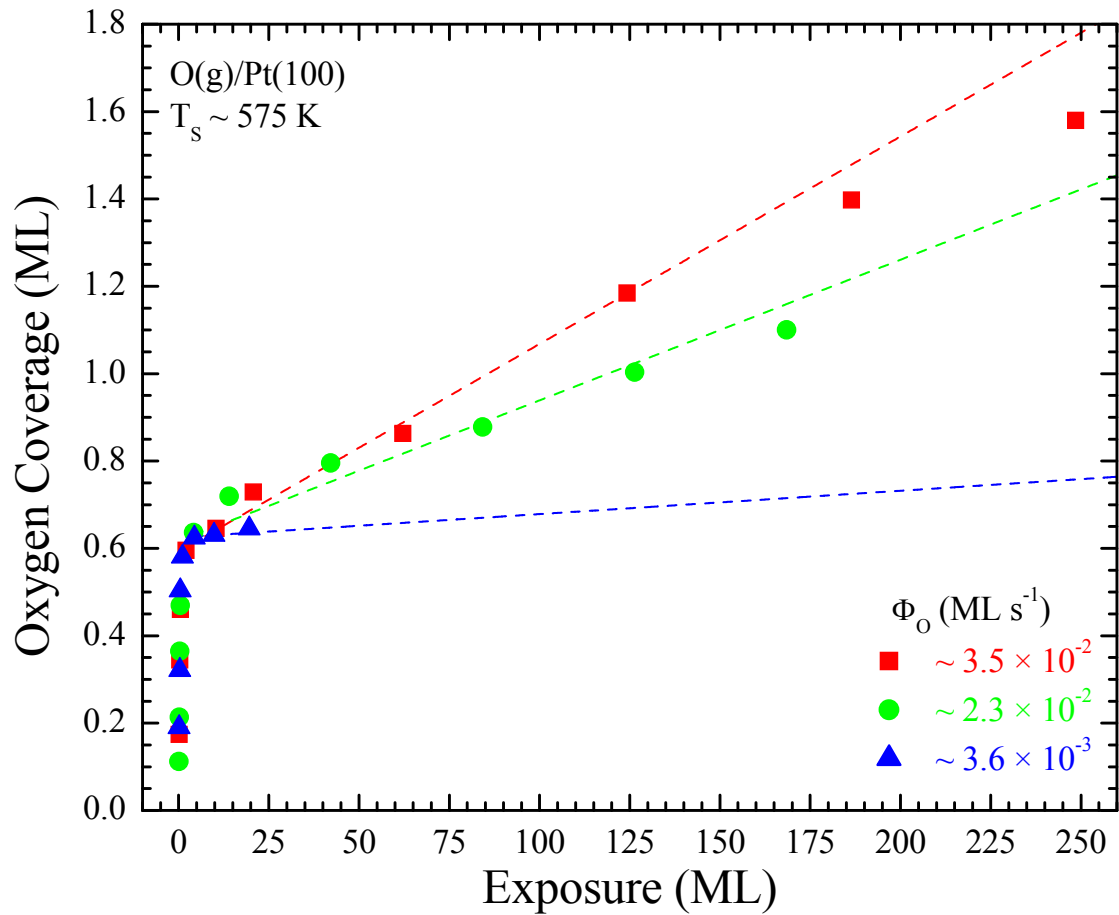


Figure 4-2. Uptake curves showing the coverages generated on Pt(100) at $\sim 575 \text{ K}$ as a function of the oxygen-atom exposure for different incident fluxes. The dashed lines give the predictions of the kinetic model described in the text.

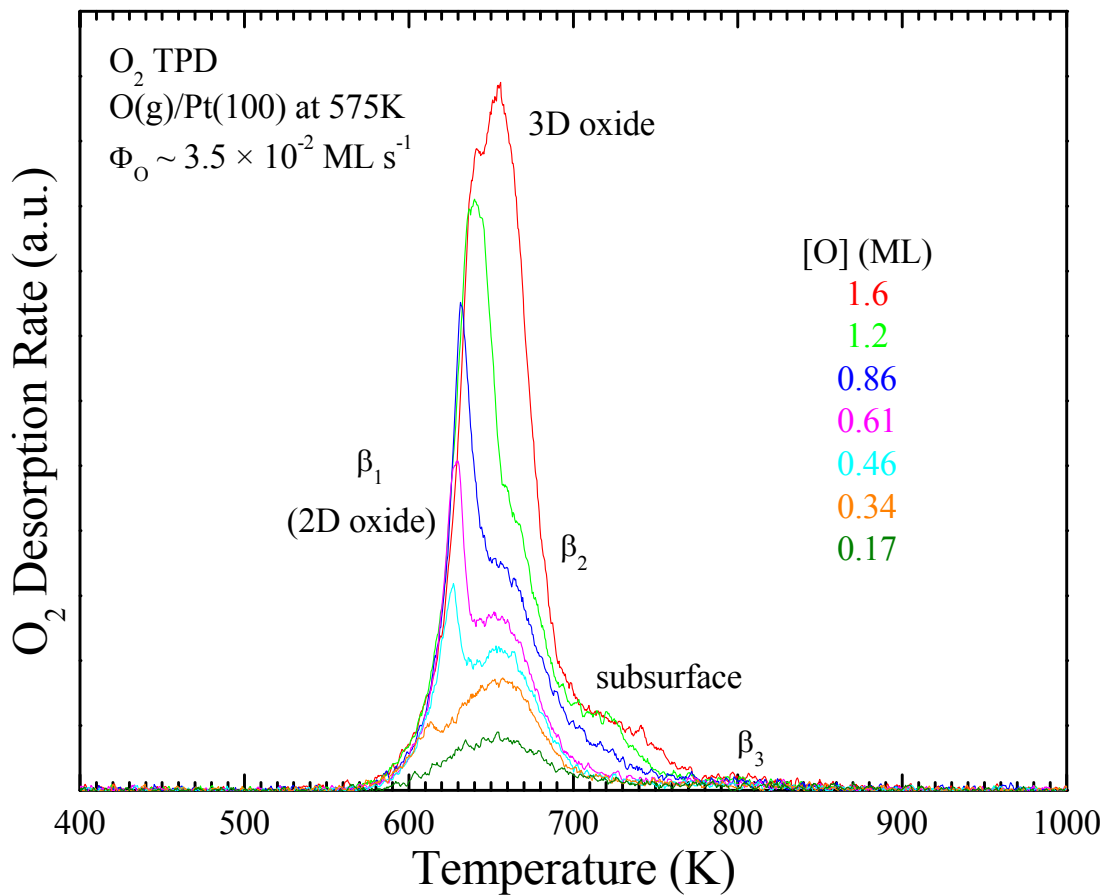


Figure 4-3. O_2 TPD spectra (temperature ramp = 1 K s^{-1}) obtained after exposing Pt(100)-hex- $R0.7^\circ$ at 575 K to an atomic oxygen beam with an incident flux of approximately $3.5 \times 10^{-2} \text{ ML s}^{-1}$.

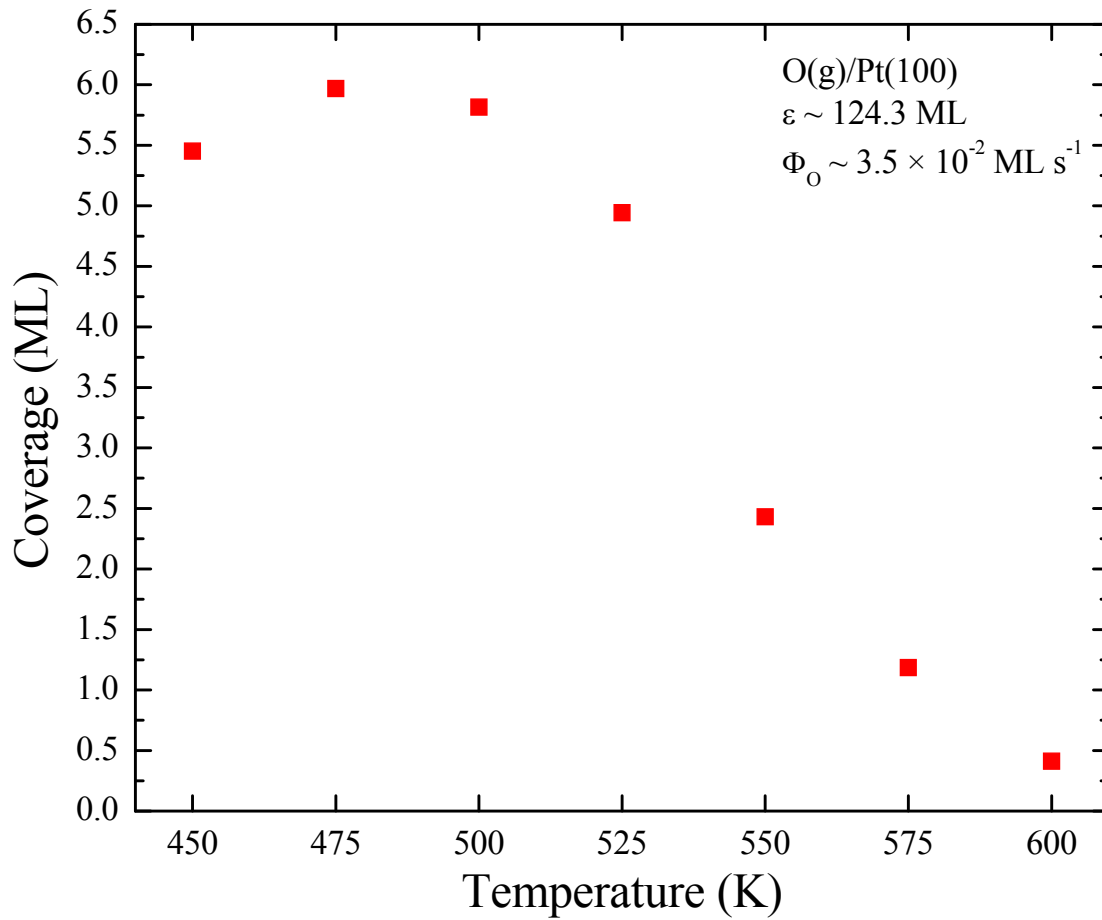


Figure 4-4. Oxygen coverages generated on Pt(100) as a function of the surface temperature for an approximately 124.3 ML exposure using an oxygen incident flux of about $3.5 \times 10^{-2} \text{ ML s}^{-1}$.

CHAPTER 5
TEMPERATURE PROGRAMMED REACTION OF CO ADSORBED ON OXYGEN-
COVERED Pt(100): REACTIVITY OF HIGH-COVERAGE OXYGEN PHASES

This chapter reproduced with permission from Journal of Physical Chemistry C, Volume 112, R.B. Shumbara, H.H. Kan, J.F. Weaver, Temperature programmed reaction of CO adsorbed on oxygen-covered Pt(100): Reactivity of high-coverage oxygen phases, Pages 4232-4241, Copyright 2008 American Chemical Society.

We utilized TPRS to investigate the reactivity of oxygen-covered Pt(100) toward the oxidation of CO. The reaction is facile on oxygen phases that form below coverages of about 1 ML, producing complicated CO₂ desorption traces. However, the reaction is inefficient when 3D oxide particles cover the surface. We observe CO₂ production in roughly three temperature regimes during TPRS. Between 120 K and 220 K, oxygen atoms react with CO molecules adsorbed within oxygen phase domains. In this regime, the reactivity toward CO is highest for 2D surface oxide, and decreases in the order of metastable oxygen phase, oxygen chemisorbed in a disordered (3×1) phase, and 3D oxide. Decreases in the CO and oxygen binding strengths generally correlate with increasing reactivity of the oxygen phases below 220 K. At temperatures from about 225 K to 335 K, reaction involves species at the boundaries of separate oxygen and CO domains. As the temperature surpasses 335 K, CO₂ production occurs between CO and disordered or isolated oxygen adatoms. Within the second temperature regime, our data suggests that both Pt and oxygen atoms migrate away from 2D and 3D oxide domains and into CO domains where reaction occurs. Kinetic barriers associated with the creation and transport of Pt adatoms likely inhibit CO oxidation by the 3D oxide. We also find that the generation of Pt adatoms facilitates significant surface defect formation and oxygen loss to the bulk during reaction. The results of this investigation clearly demonstrate that the surface oxygen phase

distribution strongly influences the temperature programmed reaction of coadsorbed CO and oxygen on Pt(100).

5.1 Introduction

The oxidation of CO on Pt and Pt-group metals remains one of the most widely studied and technologically relevant catalytic reactions dating back to the classic work by Langmuir [28]. Indeed, the active components of automobile catalytic converters, commonly used to remove CO and other pollutants from exhaust emissions, are transition metals such as Pt, Pd, and Rh supported on metal oxides. An in-depth review by Engel and Ertl [29] highlights the significant advances made in understanding the details of CO adsorption and reaction on the surfaces of Pt-group metals, establishing that CO oxidation occurs via a Langmuir-Hinshelwood mechanism whereby both reactants fully adsorb on the surface during the reaction. As such, the distribution of surface oxygen phases could play a central role in the reaction kinetics. Unfortunately, however, the relative inactivity of late transition-metal surfaces toward dissociating O₂ generally limits UHV studies to low coverages of chemisorbed oxygen atoms. In this investigation, we utilized plasma-generated atomic oxygen beams to overcome this “pressure gap” and used TPRS to examine the oxidation of CO on Pt(100) over a wide range of surface oxygen coverages that are likely relevant to commercial applications.

CO oxidation on Pt(100) has attracted considerable interest since, under certain conditions, the catalytic activity can exhibit temporal oscillations and spatio-temporal pattern formation [30]. Specifically, Ertl and coworkers [31] present clear evidence that dramatic differences in the sticking coefficient for dissociative O₂ adsorption on the surface’s hex and (1×1) reconstructions are responsible for the observed kinetic oscillations. The chemisorption of CO removes the quasihexagonal surface reconstruction, passing through $c(2\times 2)$ and $(\sqrt{2}\times 3\sqrt{2})R45^\circ$ phases before saturating in $c(4\times 2)$ domains at 0.75 ML [9,18,32], where 1 ML is equivalent to 1.28×10^{15}

atoms cm^{-2} [9]. Likewise, O_2 dissociative adsorption causes deconstruction as oxygen atoms initially chemisorb on surface defects and then arrange into “disordered” (3×1) domains, likely binding on bridge sites [101], before forming a “complex” phase that saturates at 0.63 ML [15,16,26]. Interestingly, Behm et al. [33] did not observe phase mixing or compression during CO oxidation on Pt(100) at 355 K, instead reporting coexisting $c(2\times 2)$ CO and (3×1) oxygen domains. Moreover, Barteau et al. [34] showed that adsorbed CO inhibits dissociative O_2 adsorption, effectively blocking it at CO coverages greater than 0.5 ML, while chemisorbed oxygen does not inhibit CO adsorption.

For surface temperatures greater than 300 K, Barteau et al. [34] suggested that the reaction of CO with preadsorbed oxygen atoms on Pt(100) occurs at the boundaries of oxygen islands with an activation energy of $131.4 \text{ kJ mol}^{-1}$, although the mechanistic details are not fully resolved [35]. Unfortunately, there is a lack of information concerning CO oxidation via reaction between CO and oxygen coadsorbed on Pt(100) at low initial surface temperatures, especially as it pertains to the influence of high oxygen coverages. Indeed, only two previous investigations [36,37] report the low-temperature reaction between CO and oxygen on Pt(100), finding two CO_2 TPRS features at approximately 290 K and 350 K for relatively low oxygen precoverages.

Recently, we utilized oxygen-atom beams to adsorb high oxygen concentrations on Pt(100) under UHV conditions, while characterizing the evolution of oxygen phases eventually leading to bulk oxide growth [52,68]. For low oxygen coverages, we reported that the types and relative populations of the oxygen phases that develop strongly depend on the surface temperature during adsorption. Our results show that at 573 K, gas-phase oxygen atoms behave much like gaseous O_2 with adsorption into a disordered (3×1) state and then a complex phase, which appears to be a 2D surface oxide given similarities between its properties [16] and those that exist on Pd and Rh

single crystal surfaces [93]. Furthermore, higher incident atomic oxygen fluxes facilitate the formation of 3D bulk-like oxide particles at 573 K via a precursor-mediated mechanism [102]. Interestingly, at 450 K, a disordered high-concentration state preferentially forms at the expense of the 2D oxide, implying that the disordered high-concentration state is metastable relative to the 2D oxide [68]. After accumulation of the 2D oxide, a weakly bound precursor develops that proves necessary to 3D bulk oxide formation [52,102].

In this study, we created various surface oxygen phase distributions on Pt(100) in UHV, including relatively high oxide coverages, using a plasma-generated atomic oxygen source. We then adsorbed CO on the resulting surfaces using a CO molecular beam and investigated their reactivity towards CO oxidation with TPRS. We find that the reaction occurs in roughly three temperature regimes, corresponding to reaction in mixed phases at low temperature, followed by reaction between segregated CO and oxygen domains, and finally reaction between CO and isolated oxygen atoms above 350 K. The 2D surface oxide exhibits the greatest reactivity toward CO oxidation below 200 K and the reactivity decreases in the order of metastable oxygen, (3×1) oxygen, and 3D bulk oxide. Furthermore, Pt mass transport associated with reducing the 2D and 3D oxides facilitates significant surface defect formation and oxygen loss to the bulk during reaction. Kinetic barriers to generating and removing Pt adatoms likely contribute to the low reactivity of the 3D oxide.

5.2 Experimental Methods

Previous studies [1,41,43,51] provide details of the three-level UHV system utilized for the present experiments. The Pt(100) crystal employed in this investigation is a circular disk (8 mm × ~1 mm) spot-welded to W wires and attached to a copper sample holder in thermal contact with a liquid nitrogen cooled reservoir. A type K thermocouple spot-welded to the backside of the crystal allows sample temperature measurements. Resistive heating, controlled using a PID

controller that varies the output of a programmable DC power supply, supports maintaining or linearly ramping the sample temperature from approximately 80 K to 1250 K. Initially, sample cleaning consisted of sputtering with 600 eV Ar⁺ ions at a surface temperature of 800 K, followed by annealing at 1200 K for several minutes. Subsequent cleaning involved routinely exposing the sample held at 800 K to an atomic oxygen beam for several minutes, followed by flashing the sample to 1150 K to desorb oxygen and carbon oxides. We considered the sample clean when we could no longer detect contaminants with XPS, obtain sharp LEED patterns consistent with Pt(100)-hex-*R*0.7° [13], and reproduce the established TPD spectra for both O₂ [26] and CO [18].

We prepared various surface oxygen phase distributions over a wide range of coverages on Pt(100) using a RF plasma source that generates atomic oxygen beams by partially dissociating pure O₂ (BOC gases 99.999%). Specifically, the surfaces were prepared at either 450 K or 575 K with the sample located between approximately 25 mm and 50 mm from the terminus of the quartz tube that collimates the oxygen-atom beam and rotated roughly 45° with respect to the tube axis. The incident atomic oxygen fluxes utilized ranged from about 0.023 ML s⁻¹ to 0.035 ML s⁻¹ as determined using the procedure discussed previously [102]. After each beam exposure, we cooled the sample to 100 K and exposed it to 27 ML of CO (Praxair 99.99%) at a flux of 0.03 ML s⁻¹ using a calibrated molecular beam doser. We chose 27 ML as the total CO exposure since it exceeded that needed to saturate clean Pt(100)-hex-*R*0.7° with 0.75 ML CO at 315 K [9,18,32]. Following the procedure outlined previously [1] and assuming that the initial sticking coefficient of CO at 315 K is 0.78 [18], we estimate that the surface intercepts 16.4% of the CO molecular beam for a sample-to-doser distance of about 15 mm, in close agreement with prior measurements and estimates for similar geometries [42,103]. It is worth noting that we never

observed CO₂ production during the CO dose at 100 K, and that contributions from the sample mount were generally negligible.

With the coadsorbed surfaces prepared, we performed TPRS to determine the influence of the surface oxygen phase distribution on the CO oxidation reaction. All measurements began by first facing the sample towards the entrance of a QMS ionizer at a distance of about 10 mm, cooling it to approximately 80 K, and raising the temperature at a linear rate of 1 K s⁻¹. Cooling the sample prior to beginning the temperature ramp minimizes an initial transient heating response by the PID controller such that the temperature ramp becomes linear by about 145 K. During all measurements, we simultaneously monitored the evolution of CO, O₂, and CO₂. We processed the spectra by smoothing with a 5-point adjacent averaging procedure and then performing a linear background subtraction. Scaling the areas under the CO and O₂ traces with those obtained by saturating with 0.75 ML of CO at 315 K [9,18,32] and 0.63 ML of oxygen at 573 K [16], respectively, allowed estimating the unreacted CO and oxygen coverages. Finally, we estimated the CO₂ produced by calibrating the average areas obtained from a few measurements with relatively low oxygen precoverages (excess CO), such that no significant amount of oxygen remained.

5.3 Results

5.3.1 Oxygen Preadsorbed at 575 K

To determine the influence of the surface oxygen phase distribution on the temperature programmed reaction of coadsorbed CO and oxygen on Pt(100), we first investigated oxygen-covered surfaces prepared at 575 K. Oxidation at this temperature suppresses formation of the metastable oxygen phase that we observed previously, favoring the development of an ordered surface oxide instead [68]. We investigated CO oxidation on surfaces with oxygen precoverages of 0.36 ML, 0.61 ML, and 1.6 ML to examine the reactivity of specific oxygen phases. Figure 5-

1 shows O₂ TPD spectra obtained from the initial oxygen-covered surfaces examined (dashed lines). At 0.36 ML, oxygen atoms mainly populate a “disordered” (3×1) phase, though surface oxide domains are present in small quantities. The surface oxide effectively covers the entire surface at an oxygen coverage of 0.61 ML, while both surface and bulk oxide domains exist at 1.6 ML.

The solid lines in Figure 5-1 show the O₂ TPD spectra obtained during TPRS of coadsorbed CO and oxygen (575 K). For an oxygen precoverage of 0.36 ML, we do not observe O₂ desorption during the TPRS measurement, indicating that all of the surface oxygen atoms react with CO. Interestingly, while we do not observe significant O₂ desorption, we do see very slight intensification near 850 K following the reaction with the surface initially covered by 0.61 ML of oxygen atoms. Previously, Norton et al. [26] assigned an O₂ feature at this temperature to desorption from defects associated with the surface reconstruction, suggesting that the temperature programmed reaction of coadsorbed CO and oxygen on Pt(100) may introduce additional surface defects. Finally, we note that there is relatively substantial O₂ desorption for an oxygen precoverage of 1.6 ML. Here, it appears that desorption occurs mainly from unreacted 3D oxide domains, and, to a lesser extent, from subsurface oxygen [59,94,95] and surface defects introduced by the reaction.

Figure 5-2 and Figure 5-3 show the CO₂ and CO spectra obtained during TPRS of coadsorbed CO and oxygen (575 K) on Pt(100), respectively. Interestingly, the CO₂ spectra show as many as six distinguishable desorption features that must be reaction-limited since any CO₂ produced is physisorbed and immediately desorbs [104,105]. Looking first to the CO₂ traces (Figure 5-2), it is apparent that reaction-limited CO₂ production occurs in roughly three

temperature regimes (separated by dashed lines). Specifically, the regimes correspond to production occurring at temperatures below 215 K, between 215 K and 335 K, and above 335 K.

The first regime begins with a sharp CO₂ peak ranging from 115 K to 120 K. We observe a similar CO₂ rate maximum when performing TPD from a surface initially saturated solely with CO at 100 K (not shown), suggesting that this peak is due to desorption from the sample mount with possible contributions from the initial transient heating response. After the artifact peak, two additional rate maxima appear in the first regime for all initial oxygen coverages examined. Here, the first peak desorbs at about 135 K for a surface initially covered by 0.36 ML of oxygen and shifts toward higher temperatures with increasing oxygen precoverages, desorbing at approximately 145 K for a precoverage of 1.6 ML. The second peak desorbs at about 163 K for an oxygen precoverage of 0.36 ML and more rapidly shifts to higher temperatures such that it desorbs at roughly 180 K when starting with 1.6 ML of oxygen. It is worth mentioning that complexity resulting from the superposition of the many observed reaction-limited CO₂ features restricts the utility of comparing the maximum desorption rates of each. As such, comparing the relative intensity between peaks can be much more informative. In this case, we find that the latter of the two peaks in the first regime is slightly more intense for an oxygen precoverage of 0.36 ML, but the situation reverses when the preadsorbed oxygen coverage increases to 0.61 ML with the former peak noticeably more intense. Further increasing the precoverage to 1.6 ML again causes a reversal such that the second peak becomes marginally more intense than the first. As discussed above, the 2D oxide replaces the (3×1) oxygen phase with increasing precoverage from 0.36 ML to 0.61 ML [68], while the 3D oxide replaces the 2D oxide at higher oxygen precoverages [102]. Thus, this behavior suggests that, in the first regime, the first peak is due to CO reacting with the 2D oxide and the second peak results from reaction with (3×1) oxygen.

This second peak occurs even for an initial oxygen coverage of 0.61 ML for which (3×1) oxygen domains initially exist in only small quantities. Thus, reduction of the 2D oxide by CO must create (3×1) oxygen domains that then react further during TPRS. Finally, the presence of the 3D oxide appears to either suppress the reaction of CO on the 2D oxide or enhance the reaction on the (3×1) oxygen phase since the second peak is taller for the highest oxygen precoverage. A possible explanation is that CO molecules diffuse from the 3D oxide onto (3×1) oxygen domains, thereby raising the CO coverage on the (3×1) oxygen domains beyond that produced in the absence of 3D oxide particles.

The second regime, ranging from 215 K to 335 K, also exhibits two distinct reaction-limited CO₂ peaks for all initial oxygen coverages investigated. The first of these desorbs at approximately 250 K for all oxygen precoverages, displaying only slight change in desorption temperature. Exhibiting a slightly greater range of desorption temperatures, presumably due to superposition effects, the second of these peaks occurs between about 275 K and 285 K. As before, comparing relative peak intensities is likely more informative than absolute intensities. Here, the first peak begins slightly greater than the second peak at an oxygen precoverage of 0.36 ML, but the latter peak intensifies significantly as the initial oxygen coverage increases to 0.61 ML. Again, further increasing the precovered oxygen to 1.6 ML causes this relationship to reverse such that the first peak is markedly more intense than the second peak and slightly broader than those observed for lower initial oxygen coverages. Therefore, by the same arguments presented for the first regime, within the second regime the first peak corresponds to CO reacting with the (3×1) oxygen phase and the second peak to reaction with the 2D oxide. The return of CO₂ due to CO reacting with (3×1) oxygen at a precoverage of 1.6 ML shows that the

initial presence of the 3D oxide leads to enhanced CO oxidation on the (3×1) phase during the second regime of CO₂ production as well.

The third regime, corresponding to CO₂ production above 335 K, exhibits different behavior than the two lower temperature regimes discussed above. In this case, we observe a reaction-limited peak that desorbs at approximately 385 K for an oxygen precoverage of 0.36 ML and shifts to roughly 375 K as 0.61 ML of oxygen initially covers the surface. Interestingly, this peak is no longer distinguishable when the oxygen precoverage increases to 1.6 ML. We also observe a second feature in this regime that extends to almost 530 K, only occurring when the oxygen precoverage is 0.36 ML. This second feature terminates as the desorption of unreacted CO ends (Figure 5-3) so it likely represents an oxygen-limited peak. Given the response of these features to changes in oxygen precoverage, it appears that the first CO₂ peak in the third regime corresponds to reaction conditions of relatively high CO coverages and low oxygen coverages, while the second CO₂ feature occurs under conditions where the CO and oxygen coverages are both low. We do not observe distinct CO₂ features that can be attributed to reaction with the 3D oxide, indicating that this phase has a low reactivity toward CO during TPRS. However, there is a slight level of nearly constant CO₂ production up to about 500 K for an oxygen precoverage of 1.6 ML. This CO₂ likely corresponds to a slow reaction between CO and oxygen contained within the 3D oxide as detailed below.

Shifting focus to the CO (Figure 5-3) traces, we note a few interesting observations. For comparative purposes, a spectrum obtained following a CO dose at 100 K on an initially clean sample is included to serve as a control experiment. In the desorption traces, we observe two unique features that cannot be wholly explained by the CO₂ cracking pattern. The first of these is a relatively intense peak that desorbs at about 129 K for an oxygen precoverage of 0.36 ML,

slightly shifting towards higher temperatures, broadening, and intensifying with increasing initial oxygen coverage. The second CO feature appears as a shoulder on the high-temperature side of the first peak, with the center located at approximately 165 K and 180 K for oxygen precoverages of 0.36 ML and 1.6 ML, respectively. Considering the phase distributions of the initial oxygen coverages (Figure 5-1), we attribute the earlier intense peak to CO desorption from 2D oxide domains, while the higher temperature shoulder corresponds to desorption from (3×1) oxygen regimes. Intriguingly, the desorption temperatures of these CO features agree nicely with the CO₂ features that desorb in the first regime as discussed above, suggesting similarities in the rates of desorption and reaction of CO adsorbed in the interior of oxygen domains. At higher temperatures, we only observe CO desorption for the lowest initial oxygen coverage investigated, with the peak located at about 500 K and concluding by roughly 530 K, similar to clean CO adlayers generated at 315 K [18]. Since all of the surface oxygen appears to react (Figure 5-1), we conclude that oxygen is the limiting reactant for an oxygen precoverage of 0.36 ML.

5.3.2 Oxygen Preadsorbed at 450 K

Continuing to investigate the influence of the surface oxygen phase distribution on the temperature programmed reaction of coadsorbed CO and oxygen on Pt(100), we performed experiments after preparing oxygen precoverages at 450 K. In a previous study [68], we found that reducing the preparation temperature causes dramatic differences in the surface oxygen phase distribution, with a disordered metastable phase partially replacing the 2D oxide. In the present experiments, we investigated CO oxidation on surfaces with oxygen precoverages of 0.27 ML, 0.52 ML, 1.0 ML, 2.5 ML, and 4.6 ML. The O₂ TPD spectra obtained from these initial surfaces are shown as dashed lines in Figure 5-4. At 0.27 ML, oxygen atoms exist mainly in the (3×1) oxygen and metastable phases, and only small quantities of surface oxide are

present. The surface is covered with both metastable and surface oxide phase domains at 0.52 ML, with the metastable phase being predominant. Increasing the coverage to 1 ML produces more surface oxide as well as a state that we previously attributed to oxygen atoms adsorbed on top of the surface oxide, which acts as a necessary precursor to 3D oxide formation [52,102]. Finally, 3D oxide domains are present on the surface at oxygen coverages of 2.5 ML and 4.5 ML, coexisting with domains of the 2D oxide.

Figure 5-4 also shows the O₂ traces obtained during the TPRS measurements with coadsorbed CO and oxygen precoverages prepared at 450 K (solid lines). At the lowest precoverage of 0.27 ML, we do not observe O₂ desorption, suggesting that all of the surface oxygen atoms react with CO in this case. For oxygen precoverages above 0.50 ML, we again observe an O₂ TPD feature at 850 K due to desorption from defect sites created during surface reduction by CO. In addition, O₂ desorption from precoverages greater than about 1.0 ML exhibit autocatalytic peaks characteristic of oxide island decomposition [51,52]. Here, the post-reaction peaks are less intense than and shifted towards higher temperature by roughly 5 K to 10 K from those obtained without coadsorbed CO. Given that CO reacted away some of the initial oxygen from the oxidized surface, we expect that the peak would shift towards lower temperatures as described previously [51]. Therefore, the rightward shift of a peak from lower oxygen coverages provides further support that the surface surrounding the oxide domains is defect-laden because the oxygen desorption barrier from defects is higher than from terrace sites, thereby raising the barrier for the island decomposition mechanism invoked to describe desorption from the oxide [51].

Figure 5-5 and Figure 5-6 show the CO₂ and CO spectra obtained during TPRS of coadsorbed CO and oxygen (450 K) on Pt(100), respectively. Similar to the measurements

obtained for oxygen precoverages prepared at 575 K, we observe multiple reaction-limited CO₂ peaks from the lower oxygen precoverages (≤ 1 ML), while the CO₂ spectra obtained from surfaces initially covered with 3D oxide appear less complex. Also, reaction-limited CO₂ production for precoverages prepared at 450 K (Figure 5-5) occurs in roughly three temperature regimes (dashed lines). However, compared with the results obtained from the oxygen (575 K) surfaces, the apparent boundary between the first and second regimes occurs at a slightly higher temperature of 240 K, whereas the boundary between the second and third regimes remains near 335 K. Again, we observe an artifact CO₂ peak ranging from 110 K to 120 K likely caused by desorption from the sample holder and the initial transient heating response. After the artifact peak and up to oxygen precoverages of 1.0 ML, we notice three distinct CO₂ features in the first regime. The first of these appears as a shoulder at 145 K, corresponding to reaction between CO and the 2D oxide as argued above. After the shoulder desorbs, we observe a peak that ranges from 165 K to 170 K, intensifying and broadening with increasing oxygen precoverage and likely corresponding to reaction between CO and metastable oxygen. The third peak in the first regime desorbs at 190 K and is consistent with CO oxidizing within the (3 \times 1) oxygen phase. This temperature is slightly higher than that found for oxygen precoverages prepared at 575 K, possibly indicating that CO spillover from the metastable phase onto the (3 \times 1) phase is slower than from the 2D oxide. This interpretation is consistent with the higher temperature for CO desorption from the metastable phase than the 2D oxide shown in Figure 5-6.

Unlike for precoverages generated at 575 K (Figure 5-2), we observe a single, broad reaction-limited CO₂ peak for oxygen precoverages up to about 1.0 ML prepared at 450 K (Figure 5-5) in the second regime. Interestingly, the broadness of this peak causes it to extend into the third regime for the lowest initial oxygen coverages. The peak substantially narrows and

shifts to lower temperatures with increasing oxygen precoverage. Specifically, the peak center occurs at roughly 310 K for a precoverage of 0.27 ML and shifts to approximately 285 K for a precoverage of 1.0 ML. Given the broad range of temperatures and that it extends into the third regime, this feature likely corresponds to the superposition of several CO₂ peaks originating from multiple reaction pathways with similar activation barriers, a fraction of which are higher energy pathways, such that it is not possible to resolve distinct contributions. Indeed, this explanation is plausible given the disordered nature of the metastable oxygen phase and if the surface becomes defect laden as suggested by the O₂ TPD data. Reaction of CO with the precursor oxygen atoms may also contribute to CO₂ production in the second regime, but it is difficult to discern a specific CO₂ feature associated with such a reaction. Aside from CO₂ desorption extending from the second regime into the third regime, we observe a distinct feature at 500 K that persists until about 530 K for an oxygen precoverage of 0.27 ML. Note that we observed a similar feature for the lowest initial oxygen coverage prepared at 575 K (Figure 5-2). In this case, the CO₂ feature again coincides with desorption of unreacted CO (Figure 5-6) so it is reasonable to conclude that it represents an oxygen-limited reaction pathway. As before, this CO₂ appears to desorb under conditions where the CO and oxygen coverages are both low.

While the CO₂ traces from initial oxygen coverages ranging up to 1.0 ML are rather complicated, those from 3D oxide precoverages of 2.5 ML and 4.6 ML exhibit less complexity. In both cases, we observe an initial sharp peak at about 118 K and an extremely broad feature that begins immediately after the sharp peak and extends to roughly 550 K. While the temperature of the sharp peak is indicative of desorption from the sample mount or an artifact of the transient heating response, a portion of the trailing edge appears to originate from CO reaction with 2D oxide domains. Interestingly, the intensity of the broad feature is only about 7%

of that exhibited by the most intense CO₂ TPRS feature observed in these experiments (obtained with an initial oxygen coverage of 0.52 ML) and remains nearly constant up to about 470 K, independent of oxide precoverage. As mentioned previously, we also observe a slight CO₂ feature extending to high temperature from the 1.6 ML oxygen-covered surface prepared at 575 K (Figure 5-2) that is indicative of a slow reaction between CO and oxygen contained within the 3D oxide. Clearly, the dramatic decrease in CO₂ production seen when 3D oxide dominates the surface indicates that the 3D oxide is less active toward CO oxidation than the lower coverage oxygen phases. Relatively large activation barriers associated with moving Pt atoms away from decomposing 3D oxide domains may kinetically inhibit the reaction between CO and oxygen within the oxide, as suggested in a recent study of CO oxidation on oxidized Pd(111) [106]. We speculate that the relatively constant and low CO₂ production occurs as CO reacts with oxygen in low-coverage phases located near 3D oxide boundaries and that the 3D oxide replenishes the oxygen-atom concentration within these phases, similar to previous observations [1,107]. That the intensity of the broad CO₂ feature does not vary and appears to be independent of 3D oxide precoverage suggests that the reaction front size does not significantly change during the reaction.

Looking at the CO traces (Figure 5-6) obtained during the TPRS measurements from oxygen precoverages prepared at 450 K, we observe as many as four distinct features suggesting that CO binding on an oxygen-covered Pt(100) surface is very sensitive to the oxygen phase distribution. For comparative purposes, a spectrum obtained following a CO dose at 100 K on an initially clean sample is included to serve as a control experiment. At an oxygen precoverage of 0.27 ML, CO desorbs first in a relatively sharp peak at about 140 K and then desorbs at approximately 157 K in a shoulder feature. Increasing the initial oxygen coverage to 0.52 ML

causes an additional feature to develop at about 133 K, the relative intensity of the 140 K peak to decrease, and the feature at 157 K to intensify and become more prominent. The initially sharp CO peak at 140 K probably corresponds to desorption from compressed CO on relatively clean metal sites [108] as supported by a similar peak observed after adsorbing CO on the clean surface at 100 K. Since the metastable oxygen phase is present until 3D oxide formation occurs and makes up a substantial amount of the oxygen on the surface at an oxygen coverage of 0.52 ML (Figure 5-4), we attribute the 157 K CO peak to desorption from the metastable oxygen phase. Likewise, we attribute the CO peak at 133 K to CO desorption from the 2D oxide, consistent with our assignment of CO desorption peaks from the oxygen (575 K) surfaces (Figure 5-3). Notice that this peak remains relatively intense even at high 3D oxide precoverages. The desorption of CO again occurs at temperatures close to that for CO₂ evolution in the low-temperature regime. This is indicative of a close kinetic competition between CO desorption and reaction from the 2D oxide and metastable phases.

Above an oxygen precoverage of 1.0 ML, the 157 K CO peak disappears, while at the highest precoverage of 4.6 ML we observe a pronounced peak at about 182 K. The relatively high temperature of this CO peak is intriguing since it implies that CO is more stable on top of the 3D oxide than on the 2D oxide and metastable phases. Nevertheless, this adsorbed CO does not appear to react directly with the 3D oxide, at least not to an appreciable extent, since we do not observe a distinct CO₂ feature near 180 K. This implies that CO desorption and migration away from the 3D oxide are more facile than CO reacting directly with the 3D oxide during TPRS. Again, the slow evolution of CO₂ is consistent with CO reacting within lower coverage oxygen phases while the 3D oxide continually replenishes these phases with oxygen atoms

[1,107]. This process appears to introduce significant surface defects as evidenced by relatively intense O₂ desorption (Figure 5-4) around 850 K with increasing precoverage [26].

5.3.3 Mass Balance Considerations

We performed mass balances on the desorbing species to quantify the reactivity of the different oxygen phase distributions with respect to CO adsorption and oxidation to CO₂. We did not attempt to distinguish desorption from the sample mount in our calculations but we estimate the deviations introduced by such effects to be a few percent and thus negligible for all but the highest oxygen coverages. For initial oxygen coverages of 2.5 ML and 4.6 ML, we estimate that desorption from the sample heating wires constitutes at most 20% of the total CO₂ yields so the values reported in Figure 5-7b could be overestimated by ~0.01 ML. We did attempt to account for CO₂ cracking within the ionizer of the QMS using values provided by O'Hanlon [38].

Figure 5-7a shows the CO₂ yields as a function of the initial oxygen coverage. Regardless of the preparation temperature, the CO₂ yield increases with increasing oxygen precoverage to about 0.5 ML and then decreases dramatically as the surface oxidizes. The initial increases in the CO₂ yields likely occur because oxygen is the limiting reactant at the lowest oxygen precoverages studied so more CO₂ can form when the oxygen coverage increases above about 0.40 ML. Interestingly, the maximum CO₂ yield of 0.41 ML that we observe coincides with the highest initial coverage of the disordered, metastable oxygen phase prepared at 450 K. For comparison, we observe a CO₂ yield of 0.34 ML for a surface mainly covered with the 2D oxide. After the initial drop in the CO₂ yield with initial 3D oxide formation, the CO₂ yield marginally increases from 0.04 to 0.10 ML as 3D oxide particles grow with increasing oxygen precoverage up to 4.6 ML.

Summing the CO desorbed with the CO₂ produced gives the total amount of adsorbed CO that can react during TPRS. Looking at Figure 5-7b, it appears that oxygen-covered surfaces

prepared at 450 K are able to accommodate more CO than those prepared at 575 K, especially in regards to comparing the metastable state and 3D oxide formed at 450 K with the 2D oxide generated at 575 K. In particular, there is nearly a one-to-one ratio of CO to oxygen for the surface covered primarily by the metastable oxygen phase (0.52 ML), whereas the surface initially covered mostly with 2D oxide (0.61 ML prepared at 575 K) adsorbs approximately 0.37 ML of CO. Increasing the oxygen coverage prepared at 450 K above 1 ML causes the amount of adsorbed CO to decrease significantly, reaching a value of 0.20 ML of CO for an oxygen coverage of 1.7 ML. This decrease coincides with the conversion of the metastable phase into 2D oxide, which exhibits a lower CO uptake capacity, as well as adsorption of oxygen atoms on top of the 2D oxide prior to the formation of 3D oxide. Thus, oxygen atoms adsorbed on the 2D oxide appear to contribute to lowering the CO uptake, possibly by blocking CO adsorption sites. As 3D oxide particles begin to grow on the surface, the CO coverage increases again to a final value of 0.44 ML for an oxygen precoverage of 4.6 ML. Clearly, this data shows that the disordered metastable oxygen phase and the 3D oxide provide higher concentrations of sites for CO binding compared with the 2D oxide. For the metastable phase in particular, such sites may be associated with coordinately-unsaturated Pt atoms or defect structures like oxygen vacancies.

Figure 5-7c shows the reaction probability as a function of the initial oxygen coverage where the reaction probability is defined as the amount of CO₂ produced per total amount of the limiting reactant. Adsorbed CO is the limiting reactant for all but the lowest oxygen precoverages studied. Thus, according to our definition, the reaction probability is unity for initial oxygen precoverages of 0.27 ML (575 K) and 0.36 ML (450 K) since reaction consumes all of the available surface oxygen atoms. For surfaces prepared at 450 K, the reaction probability is 76% at an initial oxygen coverage of 0.52 ML and then plummets as 3D oxide

forms, falling to only 18% at the highest oxygen precoverage. Interestingly, the reaction probability is 92% for an oxygen precoverage of 0.61 ML prepared at 575 K, and is slightly lower at 81% for an initial oxygen coverage of 1.6 ML also prepared at 575 K. Thus, a slightly higher fraction of the CO reacts when the CO is initially adsorbed on a surface covered mainly with the 2D oxide (0.61 ML at 575 K) versus the metastable phase (0.52 ML at 450 K). Finally, it is interesting that a significantly higher reaction probability is obtained on a surface covered initially with 1.6 ML of oxygen prepared at 575 K compared with nearly the same coverage (1.7 ML) prepared at 450 K. The surface prepared at 575 K consists of 2D and 3D oxide domains, whereas the surface prepared at 450 K is covered with more 3D oxide in addition to domains of the metastable phase and the 2D oxide on which oxygen atoms are adsorbed. This difference highlights the dramatic effect that the oxygen phase distribution can have on the surface reactivity.

Strikingly, performing an oxygen mass balance on the TPRS results in this study reveals that the system is not closed. Indeed, the reaction appears to facilitate significant oxygen loss to the bulk as shown in Figure 5-8. In particular, the amount of oxygen lost to the bulk remains relatively insignificant until the surface begins to oxidize, with 3D oxide leading to greater amounts of lost oxygen than the 2D oxide. For example, at the greatest oxygen precoverage of approximately 4.6 ML prepared at 450 K, we calculate that at least 0.82 ML of oxygen must be lost to the bulk because of the reaction. Since the concentration of oxygen lost correlates with the appearance of an O₂ desorption feature near 850 K (Figure 5-2 and Figure 5-4), the results suggest that the defect-laden surface caused by the reaction of CO with oxidized Pt plays a role in oxygen transport to the bulk.

5.4 Discussion

We find that the temperature programmed reaction of coadsorbed CO and oxygen on Pt(100) generally occurs in three temperature regimes. The first CO₂ production regime arises from reaction between CO and oxygen in mixed phases. Studies of CO oxidation on other metal surfaces also report that reaction between CO and oxygen in mixed phases yields CO₂ desorption features at low temperature [62,109-112]. Depending on the initial oxygen precoverage on Pt(100), CO can adsorb into or onto the (3×1) oxygen phase, the metastable oxygen phase, the 2D oxide, or the 3D oxide. Subsequent heating leads to nearly simultaneous CO and CO₂ evolution from a given oxygen phase, suggesting a close kinetic competition between CO desorption and reaction on each phase. The 3D oxide is the exception since CO₂ evolution does not appear to occur appreciably near the temperature for CO desorption from the 3D oxide. Spillover of CO from the high-density phases onto the (3×1) phase also occurs during the low-temperature reaction regime. As the reaction proceeds and the local oxygen concentration diminishes, the CO and oxygen species segregate into separate domains. Further reaction then involves species at the island boundaries, producing CO₂ in the second, or domain-boundary, regime. With oxygen islands diminishing in size, additional reaction can proceed between CO and relatively disordered or isolated oxygen in the third regime. The general mechanistic description suggested here is similar to those put forth for the temperature programmed reaction of coadsorbed CO and oxygen on Rh(100) [111], Pd(100) [62], and Ir(100) [110]. Throughout, CO₂ production likely occurs as CO approaches an oxygen adatom and causes the Pt-O bond to break via pathways similar to those previously reported [113-115].

Our data reveals distinct differences in the CO oxidation activity and binding strengths of the various surface oxygen phases on Pt(100). Based on the peak temperatures for CO₂ evolution in the low-temperature regime, the reactivity toward CO oxidation appears to be highest for the

2D oxide and decreases in the order of metastable oxygen, (3×1) oxygen, and 3D oxide. Interestingly, the CO TPD data suggests that the strength of CO binding on the oxygen phases is weakest on the 2D oxide and increases in the order of metastable oxygen, (3×1) oxygen, and 3D oxide. Looking at O₂ TPD from oxygen-covered surfaces [52,68], the peak desorption temperatures for the various oxygen phases increase in this same order. The implication is that the rate of CO₂ production increases as the CO and oxygen surface binding energies both weaken. Interestingly, the data does not reveal a distinct pathway for CO₂ production via reaction with oxygen atoms adsorbed on top of the 2D oxide, previously identified as a necessary precursor to 3D oxide formation, even though this state exhibits relatively weak binding to the surface [52,102]. It is conceivable, however, that precursor oxygen atoms preferentially replenish oxygen reacted from the highly reactive 2D oxide rather than reacting directly with coadsorbed CO under the conditions we examined, possibly due to a lower kinetic barrier to the replenishment pathway. In a similar observation, Kim et al. [116] suggested that weakly held oxygen atoms on top of the 3D oxide replenish oxygen vacancies during CO oxidation on RuO₂(110).

In addition to affecting the CO binding strength, the surface oxygen phase distribution significantly influences the amount of CO uptake at low temperature (Figure 5-7b), implying that each phase offers different concentrations of CO binding sites. In particular, our data suggests that the CO binding site concentration is highest on the metastable oxygen phase and then decreases in the order of 3D oxide, (3×1) oxygen, and 2D oxide. It is especially interesting that the site concentration on the metastable oxygen phase appears to be markedly higher than on the 2D oxide. In prior work, we suggested that the metastable phase forms when oxygen atoms adsorb into the (3×1) phase [68]. Recent studies with Au(111) [117] and Pd(111) [118] show that

disordered phases with “added” metal atoms develop as domains with chemisorbed oxygen atoms transform into ordered surface oxide. On Au(111), these disordered phases appear as 3D clusters dispersed across flat terraces. We speculate that the metastable phase on Pt(100) has a similar morphology as observed on these other surfaces. In this case, it is reasonable to expect that the metastable phase possesses relatively high concentrations of coordinately-unsaturated Pt atoms that exhibit relatively high affinity toward CO. The average Pt-O coordination likely increases as atoms in the metastable phase adopt the more ordered arrangement of the 2D oxide, perhaps resulting in lower concentrations of sites that can strongly bind CO. In addition, precursor oxygen atoms adsorbed on top of the 2D oxide may block CO binding sites.

We attribute the CO₂ evolution in the second temperature regime between about 220 K and 350 K to reaction involving species at the domain boundaries of distinct CO and oxygen phases. We note that reaction could occur between CO and oxygen at the domain boundaries or that oxygen atoms could diffuse into the interior of CO domains and then react. A similar interpretation has been given in prior studies of CO oxidation [62,110,111], and is consistent with the CO TPD data that we obtained (Figure 5-3 and Figure 5-6). Specifically, we observe that CO initially adsorbed on any of the surface oxygen phases desorbs below 200 K during TPD, whereas CO desorbs from metallic sites between 400 K and 500 K. This observation suggests that reaction in the second temperature regime (~220-350 K) involves CO molecules adsorbed within metallic domains. Since metallic sites only sparsely cover the surface at high initial oxygen coverages, metallic domains must be created below about 200 K during TPRS as CO removes oxygen from the surface. Given that CO molecules are initially located within the oxygen phases, CO spillover from the oxygen phases onto metallic domains must be rather facile, occurring in parallel to the desorption and reaction of CO present within oxygen phase

domains. Clearly, several coupled processes occurring within the mixed-phase regime determine the rates and yields of CO₂ produced in the domain-boundary regime during the TPRS experiments.

An interesting characteristic of the domain-boundary regime may be seen in the data obtained from oxygen-covered surfaces prepared at 575 K. Here, the CO₂ features in the second temperature regime (Figure 5-2) evolve with initial oxygen coverage in a manner that implies more facile reaction of CO with oxygen originating from the boundaries of the (3×1) oxygen phase than the 2D oxide, which is opposite to the behavior observed in the low-temperature, mixed-phase regime and hence contrary to the simple correlation between reactivity and binding strengths discussed above. This may arise from differences in the reactive configurations of CO and oxygen at domain boundaries compared with the configurations available inside the oxygen domains. However, removing oxygen from the perimeters of 2D and 3D oxide domains also produces Pt adatoms, which is likely to be energetically demanding and could significantly contribute to the energy barriers for CO reacting at the oxide domain boundaries.

Our data provides evidence for the creation and transport of Pt adatoms during reduction of the oxidized surfaces by CO. Firstly, we observe substantial loss of oxygen to the bulk (Figure 5-8) when the oxygen precoverage increases to values characteristic of 2D and 3D oxides. This result appears to coincide with the introduction of significant defect levels [26] as evidenced by a post-reaction O₂ desorption feature near 850 K (Figure 5-1 and Figure 5-4). These observations suggest large amounts of Pt and oxygen mass transport during the reaction of CO with oxygen contained in the 2D and 3D oxides. We speculate that reaction occurs directly at CO-oxide domain boundaries and also within metallic domains between CO and oxygen atoms that enter the metallic areas by migrating away from nearby oxide domains. In the latter reaction, the oxide

domains act as a source that sustains reaction by replenishing the metallic domains with oxygen atoms. Previous researchers similarly describe CO isothermally reacting with oxides on the Pt(111) [1] and Pd(100) [107] surfaces.

As CO₂ evolves from the reaction on metal sites and the oxide replenishes the reacted oxygen, Pt atoms release from the oxides, introducing surface roughness and increased levels of defect sites. Interestingly, recent STM images suggest that mass transport of metal atoms from oxide layers during reduction by CO roughens the Ag(111) surface [119]. Thus, the limited reactivity observed for the 3D oxide is probably due to large barriers associated with moving Pt atoms away from decomposing 3D oxide domains [106], the likelihood that reaction occurs on metal sites near domain boundaries [1,100], and the low barrier to CO desorption relative to reaction from the oxide (Figure 5-5 and Figure 5-6). Furthermore, we speculate that Pt mass transport associated with oxide reduction is also responsible for the relatively large concentrations of oxygen lost to the bulk. Indeed, similar Pt transport processes associated with the surface reconstruction are apparently responsible for oxygen populating subsurface sites several layers deep during CO oxidation on Pt(100) [50,59,94,95]. While future measurements may provide additional insight into the details of oxygen entering the bulk during CO oxidation via TPRS of coadsorbed CO and oxygen on Pt(100), the present results show that Pt adatoms are released from the oxides given the increased surface defect concentrations observed.

5.5 Summary

We utilized TPRS to examine the reaction between coadsorbed CO and oxygen atoms in various surface phase distributions on Pt(100) under UHV conditions. Specifically, we adsorbed CO at low temperatures on oxygen-covered surfaces generated at 450 K and 575 K to study the reactivity of oxygen atoms in a (3×1) chemisorbed phase, a disordered metastable phase, an ordered 2D oxide, and 3D oxide particles. Our results show that the temperature programmed

reaction between CO and oxygen generally occurs in three temperature regimes. Below about 220 K, reaction occurs between CO and oxygen in mixed phases such that CO is adsorbed within the interior of oxygen phase domains. Within the mixed-phase regime, the reactivity toward CO oxidation appears to be highest for the 2D oxide and decreases in the order of metastable oxygen, (3×1) oxygen, and 3D oxide. The strength of CO and oxygen binding in the oxygen phases increases in the same progression that the reactivity of the phases decreases, suggesting that reaction is more facile when the reactants are more weakly bound. We do not observe evidence for a direct reaction between CO adsorbed on the 3D oxide and oxygen atoms within the 3D oxide. The individual oxygen phases also exhibit differences in CO uptake, with the metastable phase accommodating more adsorbed CO than the 2D oxide. This finding supports the conclusion that the metastable phase possesses relatively high concentrations of added Pt atoms on which CO molecules bind.

At temperatures from about 225 K to 335 K, CO₂ production results from CO reacting with oxygen atoms that originate from boundaries separating oxygen phase domains from CO-containing metallic areas generated during surface reduction at low temperature. Additional reaction above 335 K proceeds between CO and disordered or isolated oxygen adatoms. The data shows that reaction in the domain-boundary regime involves transport of both Pt and oxygen atoms, with oxygen atoms migrating away from 2D and 3D oxide domains and into metallic domains where reaction occurs. The concurrent diffusion of Pt adatoms away from the oxide domains also significantly increases surface defect concentrations and appears to facilitate oxygen diffusion into the subsurface region. We speculate that energy barriers associated with the creation of Pt adatoms during reduction of 3D oxide domains contributes to the low reactivity of the 3D oxide on Pt(100). Additional work is needed to determine if the Pt adatoms play a role

in mediating CO oxidation in metallic surface domains. Collectively, these results demonstrate that the surface oxygen phase distribution strongly influences the temperature programmed reaction of coadsorbed CO and oxygen on Pt(100).

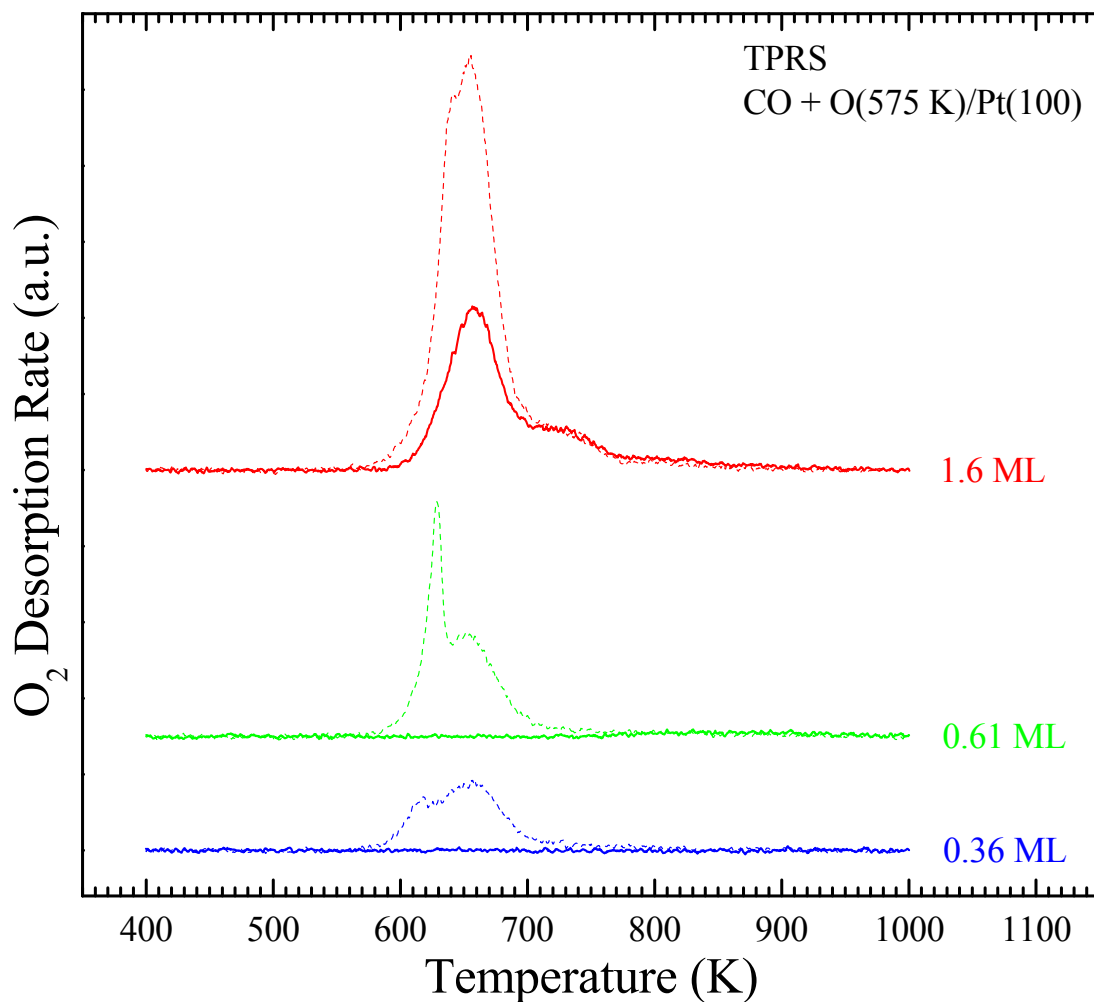


Figure 5-1. O₂ TPD traces (temperature ramp = 1 K s⁻¹) obtained from initial oxygen coverages of 0.36 ML, 0.61 ML, and 1.6 ML prepared on Pt(100) at 575 K without coadsorbed CO (dashed lines). O₂ TPRS traces obtained after exposing the oxygen-covered surfaces to 27 ML of CO at 100 K (solid lines), and simultaneously monitoring the CO₂ and CO partial pressures as shown in Figure 5-2 and Figure 5-3. Features at approximately 625 K, 653 K, 720 K, and 850 K are characteristic of desorption from 2D oxide, disordered (3×1), subsurface oxygen, and surface defects, respectively. The sharp peak at 655 K for the 1.6 ML precoverage corresponds to the decomposition of 3D oxide domains.

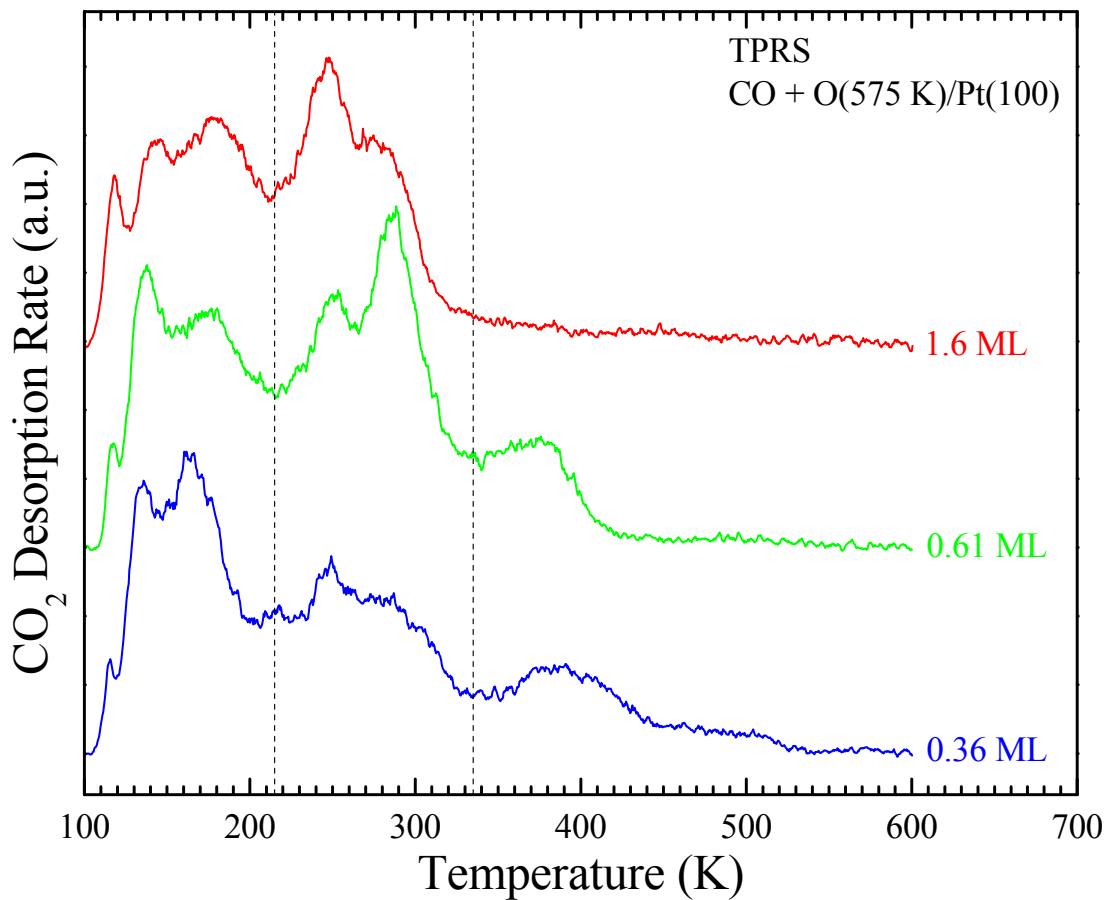


Figure 5-2. CO₂ TPRS traces (temperature ramp = 1 K s⁻¹) obtained after exposing 27 ML of CO at 100 K on Pt(100) with oxygen precoverages of 0.36 ML, 0.61 ML, and 1.6 ML prepared at 575 K. The vertical dashes approximately separate apparent CO₂ production regimes as discussed in the text.

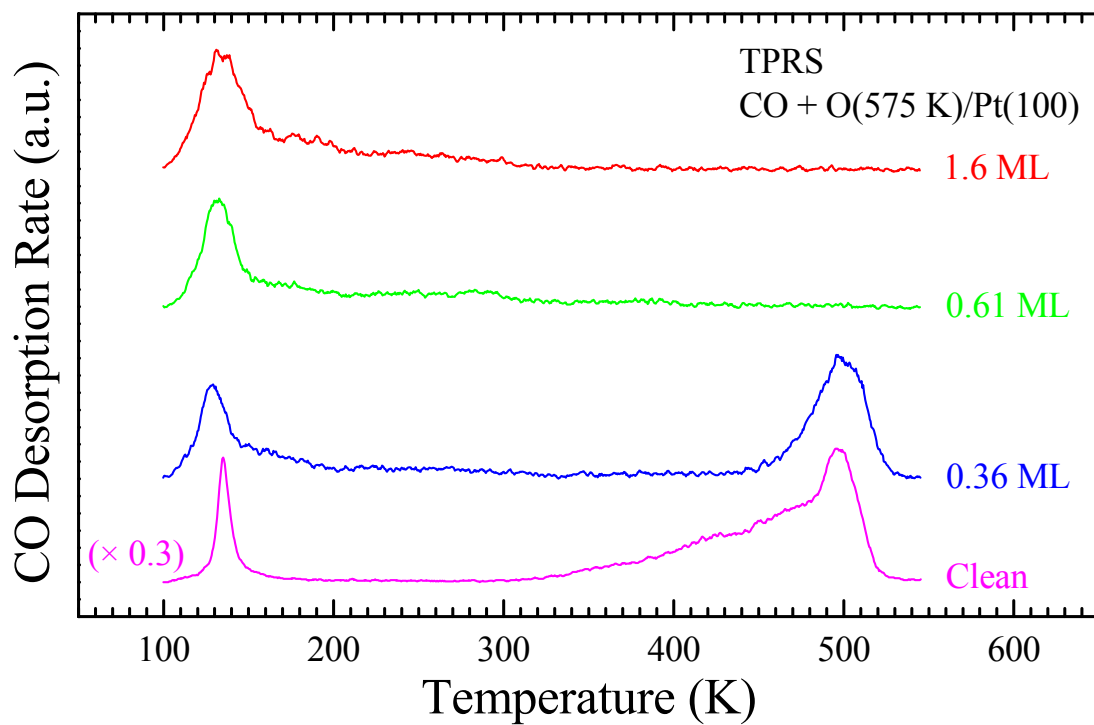


Figure 5-3. CO TPRS traces (temperature ramp = 1 K s^{-1}) simultaneously obtained with the CO_2 spectra shown in Figure 5-2. The surfaces were prepared by exposing 27 ML of CO at 100 K on clean Pt(100) and with oxygen precoverages of 0.36 ML, 0.61 ML, and 1.6 ML prepared at 575 K.

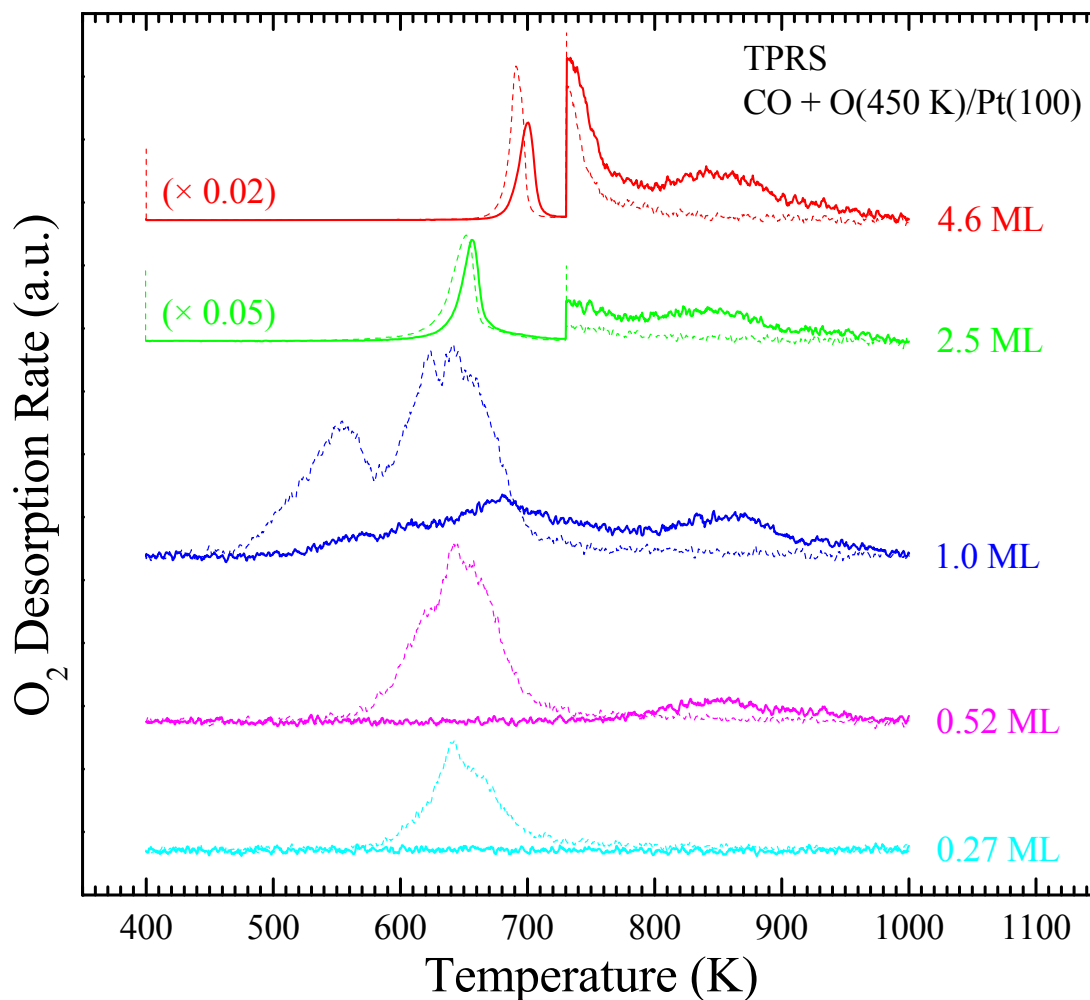


Figure 5-4. O_2 TPD traces (temperature ramp = 1 K s^{-1}) obtained from initial oxygen coverages of 0.27 ML, 0.52 ML, 1.0 ML, 2.5 ML, and 4.6 ML prepared at 450 K without coadsorbed CO (dashed lines). O_2 TPRS traces obtained after exposing the oxygen-covered surfaces to 27 ML of CO at 100 K (solid lines), and simultaneously monitoring the CO_2 and CO partial pressures as shown in Figure 5-5 and Figure 5-6. Features at approximately 555 K, 625 K, 642 K, 655 K, and 850 K are characteristic of desorption from precursor oxygen atoms, 2D oxide, metastable oxygen, disordered (3×1), and surface defects, respectively. The intense peaks for precoverages of 2.5 ML and 4.6 ML correspond to the decomposition of 3D oxide domains.

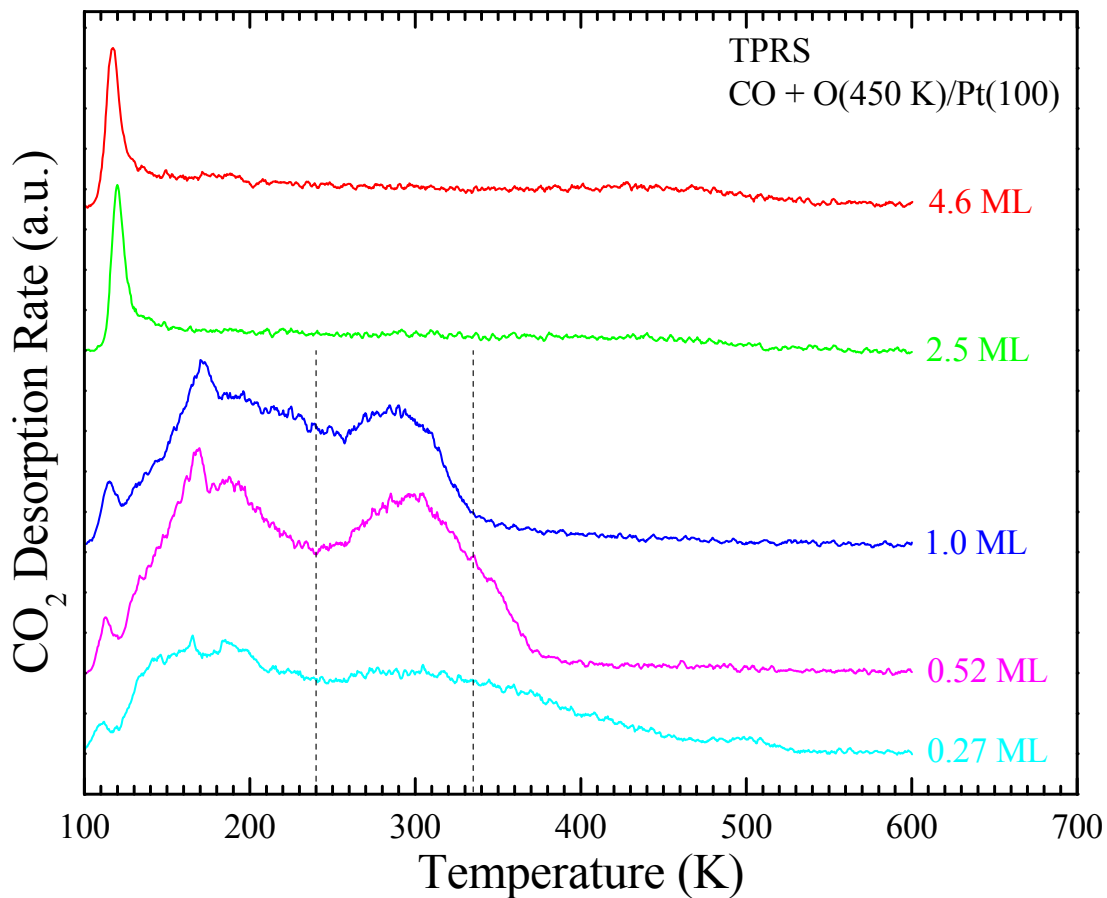


Figure 5-5. CO₂ TPRS traces (temperature ramp = 1 K s⁻¹) obtained after exposing 27 ML of CO at 100 K on Pt(100) with oxygen precoverages of 0.27 ML, 0.52 ML, 1.0 ML, 2.5 ML, and 4.6 ML prepared at 450 K. The vertical dashes approximately separate apparent CO₂ production regimes as discussed in the text.

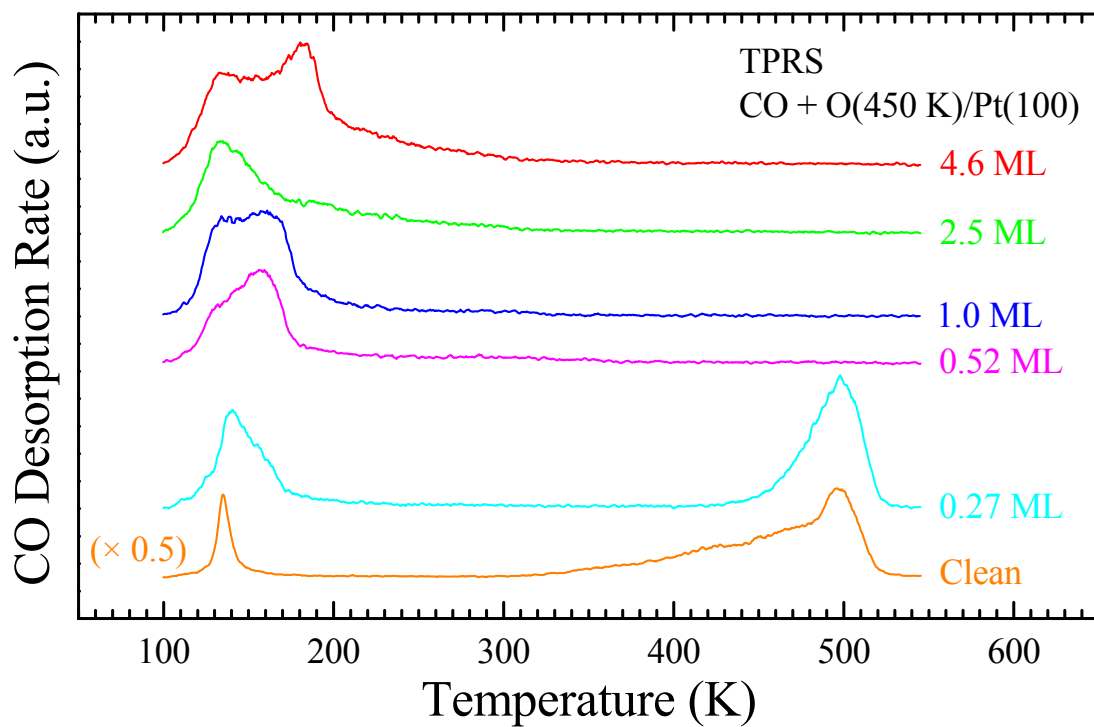


Figure 5-6. CO TPRS traces (temperature ramp = 1 K s^{-1}) simultaneously obtained with the CO_2 spectra shown in Figure 5-5. The surfaces were prepared by exposing 27 ML of CO at 100 K on clean Pt(100) and with oxygen precoverages of 0.27 ML, 0.52 ML, 1.0 ML, 2.5 ML, and 4.6 ML prepared at 450 K.

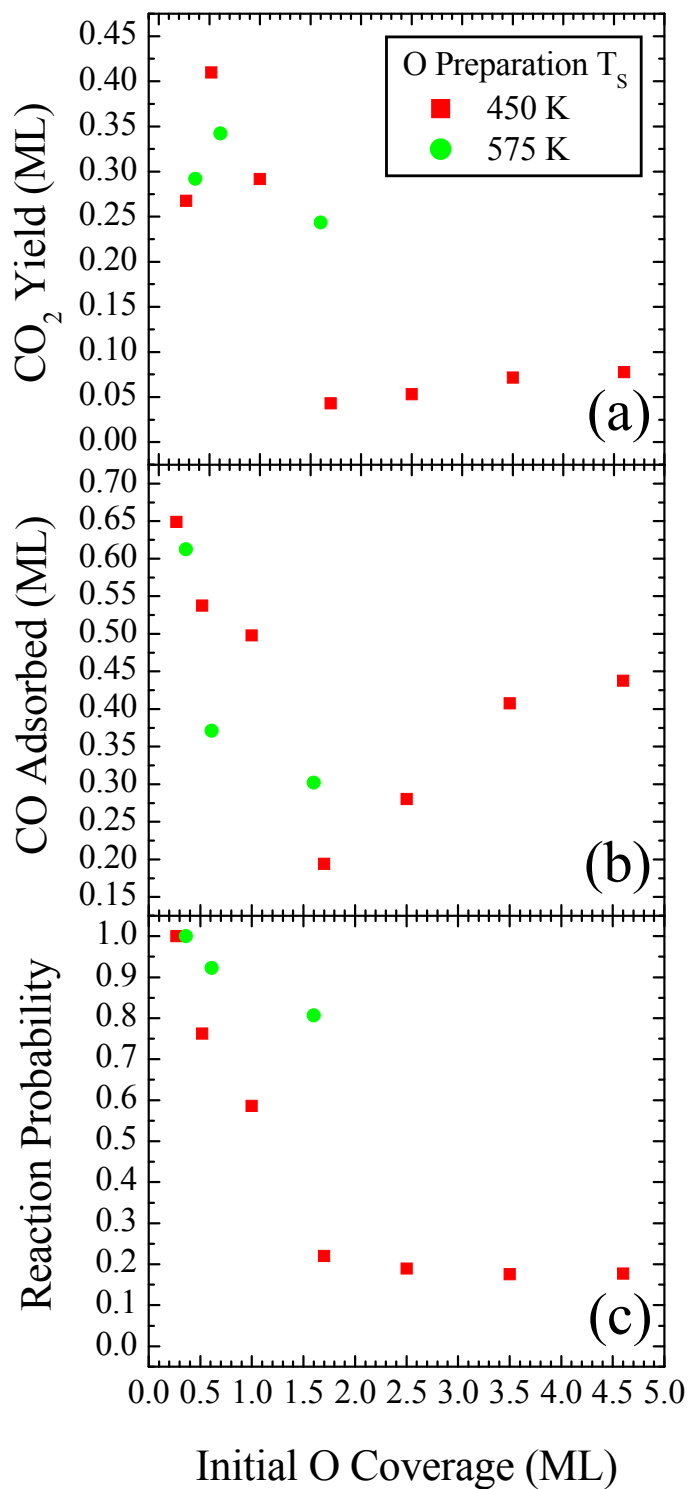


Figure 5-7. Estimated (a) CO₂ yields, (b) total CO adsorbed, and (c) reaction probability for TPRS of coadsorbed CO and oxygen on Pt(100) as a function of the initial oxygen coverage and the precoverage preparation temperature. The reaction probability is defined as the ratio of the CO₂ yield to the coverage of the limiting reactant.

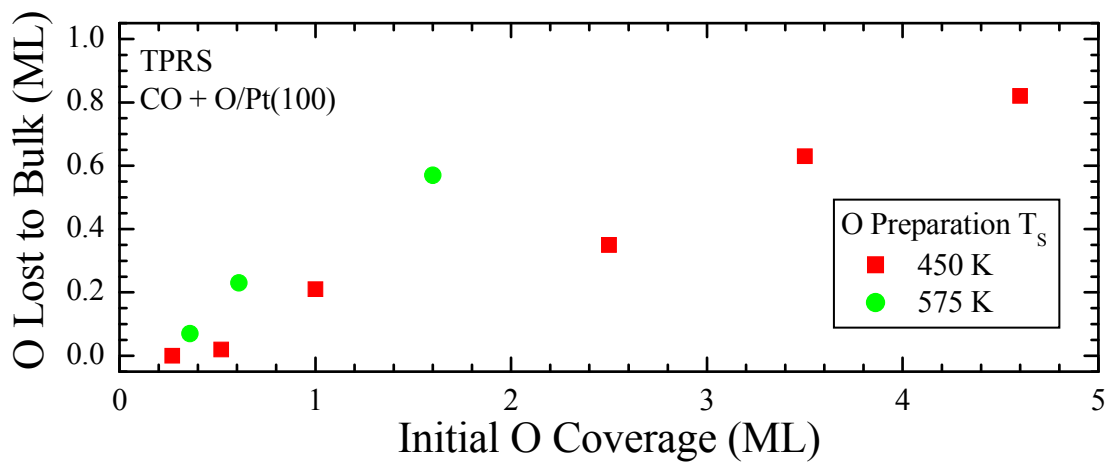


Figure 5-8. Estimated concentration of oxygen lost to the bulk during TPRS of coadsorbed CO and oxygen on Pt(100) as a function of the initial oxygen coverage and the precoverage preparation temperature.

CHAPTER 6
ISOTHERMAL OXIDATION OF CO MOLECULAR BEAMS ON OXYGEN-COVERED
Pt(100)

This chapter reproduced with permission from Journal of Physical Chemistry C, R.B. Shumbera, H.H. Kan, J.F. Weaver, Isothermal oxidation of CO molecular beams on oxygen-covered Pt(100), submitted for publication, Unpublished work, Copyright 2008 American Chemical Society.

We utilized direct, isothermal rate measurements to investigate the reactivity of oxygen-covered Pt(100) toward the oxidation of CO above 300 K, finding that the reaction is facile on oxygen phases that form below coverages of about 1 ML and inefficient when 3D oxide particles cover the surface. For relatively low oxygen coverages, the CO₂ production rate as a function of the CO beam exposure exhibits a nearly linear increase toward a maximum and slow decay thereafter. At fixed CO incident flux, the time required to reach the rate maximum increases with increasing initial oxygen coverage. Despite their inability to adsorb CO strongly, we find that the metastable oxygen state and the 2D surface oxide are active toward CO oxidation between 400 K and 550 K, with the 2D oxide exhibiting greater reactivity. After initially consuming these phases, the reaction then also takes place at higher rates on metallic regions of the surface covered with relatively low coverages of chemisorbed oxygen atoms. On surfaces partially covered with 3D oxide, the CO exposure needed to reach the rate maximum increases significantly with increases in the initial oxygen coverage and the temperature, since the fraction of the surface covered by more reactive oxygen phases decreases. Moreover, we speculate that oxygen migration from the 3D oxide into an adsorbed state on the 2D oxide competes with CO adsorption, thereby further suppressing the CO oxidation rate at relatively high 3D oxide coverages. Finally, we present evidence that CO reacts directly with the 3D oxide, although at

much lower rates compared with the other oxygen phases, and that the morphology of the 3D oxide strongly influences the reaction kinetics.

6.1 Introduction

The oxidation of CO on Pt and Pt-group metals remains one of the most widely studied and technologically relevant catalytic reactions dating back to the classic work by Langmuir [28]. A better comprehension of this reaction on Pt surfaces is central to many applications of heterogeneous catalysis; the most notable being the catalytic conversion of CO to CO₂ in automobile exhausts. Significant progress has been made in understanding the mechanistic details of CO adsorption and reaction on Pt surfaces. Indeed, an in-depth review by Engel and Ertl [29] highlights these advances, establishing that CO oxidation occurs via a Langmuir-Hinshelwood mechanism whereby both reactants fully chemisorb prior to reacting. As such, the distribution and morphology of surface oxygen phases could play a critical role in the reaction kinetics. Unfortunately, however, challenges in preparing high oxygen concentrations on noble-metal surfaces in UHV generally limit studies to low coverages of chemisorbed oxygen atoms. In this investigation, we utilized plasma-generated oxygen-atom beams to reproducibly generate oxygen-covered Pt(100) surfaces and employed beam reflectivity techniques to examine the isothermal oxidation of CO on these surfaces, paying particular focus to the influences of the surface oxygen phase distribution and morphology for coverages ranging from low concentrations of chemisorbed oxygen to bulk-like oxides.

CO oxidation on Pt(100) is of particular interest since, under certain conditions, the catalytic activity can exhibit temporal oscillations and spatio-temporal pattern formation [30]. Specifically, work by Ertl and coworkers [31] provides convincing evidence that dramatic variations in the O₂ dissociative adsorption probability on the quasihexagonal surface reconstruction and the bulk-terminated (1×1) surface are responsible for the observed kinetic

oscillations. The chemisorption of CO removes the quasihexagonal surface reconstruction, passing through $c(2\times 2)$ and $(\sqrt{2}\times 3\sqrt{2})R45^\circ$ phases before saturating in $c(4\times 2)$ domains at 0.75 ML [9,18,32], where 1 ML is equivalent to 1.28×10^{15} atoms cm^{-2} [9]. Likewise, O_2 dissociative adsorption causes deconstruction as oxygen atoms initially chemisorb on surface defects and then arrange into “disordered” (3×1) domains, likely binding on bridge sites [101], before forming a “complex” phase that saturates at 0.63 ML [15,16,26]. Interestingly, Behm et al. [33] did not observe phase mixing or compression when exposing CO-covered Pt(100) to gas-phase O_2 at 355 K, instead reporting coexisting $c(2\times 2)$ CO and (3×1) oxygen states. Moreover, Barteau et al. [34] showed that adsorbed CO inhibits dissociative O_2 adsorption, effectively blocking it at CO coverages greater than 0.5 ML, while chemisorbed oxygen does not inhibit CO adsorption.

Recently, we utilized oxygen-atom beams to examine the temperature programmed reaction of coadsorbed CO and oxygen on Pt(100), finding that the surface oxygen phase distribution strongly influences the reaction [120]. While our results indicate that the reaction is facile on oxygen phases that form below coverages of about 1 ML, the reaction is inefficient when 3D oxide particles cover the surface. Moreover, we find that CO readily adsorbs on oxygen-covered Pt(100) at 100 K, with the oxygen phase distribution affecting the CO binding energy and the amount of CO accommodated. Regardless of the oxygen state within which CO binds, it desorbs below temperatures of about 220 K, suggesting that the CO desorption rate from these mixed states will be relatively high under typical reaction conditions above room temperature.

In studying the kinetics of CO oxidation over Pt(100) at temperatures above room temperature, Barteau et al. [34] concluded that, during exposure to CO, adsorbed oxygen remains in islands and only CO which adsorbs at the perimeter of these islands participates in the reaction

with an activation energy of $131.4 \text{ kJ mol}^{-1}$. However, Bechtold [35] later questioned whether Barteau et al.'s results necessarily indicate that CO must directly adsorb at the perimeter of oxygen islands to react. Indeed, Behm and coworkers [33] report that during the reaction of adsorbed oxygen with gas-phase CO, the CO coverage remains negligible for oxygen coverages greater than 0.05 ML at 355 K, indicating that the rates of CO desorption and reaction must be at least as fast as the CO adsorption rate. Furthermore, their data suggests that oxygen does not remain in (3×1) islands, but is uniformly reduced in density leaving a (1×1) surface covered with relatively isolated oxygen atoms.

In the present study, we prepared various surface oxygen phase distributions on Pt(100) in UHV, including relatively high oxide coverages, using a plasma-generated atomic oxygen source. We then conducted direct, isothermal rate measurements using a CO molecular beam to investigate the oxidation of CO on the resulting oxygen-covered surfaces. As with Pt(111) [1], the results reveal that the CO oxidation rate diminishes as the surface coverage of atomic oxygen increases, and that the presence of Pt oxide domains significantly inhibits the reaction. Furthermore, we find that the morphology of bulk oxide domains and the distribution of surface oxygen phases can greatly influence the reaction. These results provide continuing support to the growing experimental evidence that oxidized Pt is less reactive toward CO oxidation than chemisorbed oxygen atoms adsorbed on the Pt surface as well as the intermediate oxygen phases that form below 1 ML.

6.2 Experimental Methods

Previous studies [1,41,43,51] provide details of the three-level UHV system utilized for the present experiments. The Pt(100) crystal employed in this investigation is a circular disk (8 mm \times \sim 1 mm) spot-welded to W wires and attached to a copper sample holder in thermal contact with a liquid nitrogen cooled reservoir. A type K thermocouple spot-welded to the backside of

the crystal allows sample temperature measurements. Resistive heating, controlled using a PID controller that varies the output of a programmable DC power supply, supports maintaining or linearly ramping the sample temperature from approximately 80 K to 1250 K. Initially, sample cleaning consisted of sputtering with 600 eV Ar⁺ ions at a surface temperature of 800 K, followed by annealing at 1200 K for several minutes. Subsequent cleaning involved routinely exposing the sample held at 800 K to an atomic oxygen beam for several minutes, followed by flashing the sample to 1150 K to desorb oxygen and carbon oxides. We considered the sample clean when we could no longer detect contaminants with XPS, obtain sharp LEED patterns consistent with Pt(100)-hex-R0.7° [13], and reproduce the established TPD spectra for both O₂ [26] and CO [18].

We prepared various surface oxygen phase distributions over a wide range of coverages on Pt(100) using a RF plasma source that generates atomic oxygen beams by partially dissociating pure O₂ (BOC gases 99.999%). Specifically, the surfaces were prepared at either 450 K or 575 K with the sample located between approximately 25 mm and 50 mm from the terminus of the quartz tube that collimates the oxygen-atom beam and rotated roughly 45° with respect to the tube axis. The incident atomic oxygen fluxes utilized ranged from about 0.023 ML s⁻¹ to 0.035 ML s⁻¹ as determined using the procedure discussed previously [102]. After generating the oxygen-covered surfaces, we conducted beam reflectivity experiments to directly measure the rate of CO oxidation. In these experiments, oxygen-covered Pt(100) is held at a fixed temperature and exposed to a CO (Praxair 99.99%) beam at a flux of 0.03 ML s⁻¹ using a calibrated molecular beam doser while monitoring the temporal evolution of the CO₂ partial pressure. We positioned the QMS such that species that scatter or desorb from the surface randomize in the chamber before entering the ionizer. Under the conditions employed, the CO₂

partial pressure is linearly proportional to the total reflection rate of CO₂ from the surface. Since CO oxidation on the sample surface is the predominant source of CO₂ production and the CO₂ desorbs rapidly upon forming, the temporal evolution of the CO₂ partial pressure provides a direct measure of the CO₂ production rate on the surface. It is worth noting that following the procedure outlined previously [1] and assuming that the initial sticking coefficient of CO at 315 K is 0.78 [18], we estimate that the surface intercepts 16.4% of the CO molecular beam for a sample-to-doser distance of about 15 mm, in close agreement with prior measurements and estimates for similar geometries [42,103].

Given that relatively long times were required for the beam reflectivity experiments, we calibrated the amount of CO₂ produced in each measurement using mass balances on the initial and final surface oxygen concentrations to account for any variation in the pumping speed throughout the study. Interestingly, unlike similar investigations of CO oxidation on Pt(111) [1] and Pd(100) [107] surfaces, we found that our reaction conditions were not always sufficient to completely reduce oxygen-covered Pt(100), particularly for the higher initial oxygen coverages. In these cases, the remaining oxygen was consistent with subsurface oxygen [59,94,95] populated during the initial exposure to the oxygen-atom beam [102]. We processed the beam reflectivity data by first applying 21-point Savitzky-Golay [72] smoothing, followed by a linear background subtraction. To facilitate the mass balances, we performed TPD after each beam reflectivity experiment. All TPD measurements began by first facing the sample towards the entrance of a QMS ionizer at a distance of about 10 mm, cooling it to approximately 80 K, and raising the temperature at a linear rate of 1 K s⁻¹. Cooling the sample prior to beginning the temperature ramp minimizes an initial transient heating response by the PID controller such that the temperature ramp becomes linear by about 145 K. For all measurements, we simultaneously

monitored the evolution of CO, O₂, and CO₂, and processed the spectra by smoothing with a 5-point adjacent averaging procedure and then performing a linear background subtraction. CO and O₂ desorption were calibrated by scaling the areas under the traces with those obtained by saturating a clean sample with 0.75 ML of CO at 315 K [9,18,32] and 0.63 ML of oxygen at 573 K [16], respectively.

6.3 Results

6.3.1 Oxygen Phase Development on Pt(100)

In recent work [52,68,102], we provided extensive details regarding the development of oxygen phases on Pt(100) using a gaseous oxygen-atom beam. In these investigations, we found that oxygen coverages of several ML can be prepared on Pt(100), and that 3D oxide particles form on the surface above coverages of about 1 ML. Figure 6-1 shows representative O₂ TPD traces obtained after adsorbing different amounts of atomic oxygen using the beam. Here, Figure 6-1a displays measurements from oxygen-covered surfaces prepared at 575 K, while Figure 6-1b and Figure 6-1c show TPD spectra from surfaces with relatively low and relatively high oxygen coverages prepared at 450 K, respectively.

Figure 6-1a shows O₂ TPD spectra obtained from Pt(100) after preparing different oxygen-atom coverages at a surface temperature of 573 K. Briefly, three states populate nearly sequentially with increasing oxygen coverage. Initially, oxygen adsorbs on surface defects associated with the surface reconstruction and gives rise to a small desorption feature, labeled β_3 , which extends to approximately 950 K. Desorbing at approximately 672 K, the β_2 peak intensifies with increasing coverage from 0.10 ML to 0.32 ML and is characteristic of oxygen atoms arranged into “disordered” (3×1) domains [16]. Further increasing the coverage to 0.63 ML causes autocatalytic desorption as exhibited by the β_1 feature, whose maximum shifts from about 631 K to 642 K at higher coverages. Traditionally referred to as a “complex” ordered state

[15,16], measurements indicating that the work-function change decreases as the β_1 peak grows [16] and investigations exhibiting similar desorption characteristics from the 2D surface oxide that forms on Pd(100) over a similar coverage range [63,77] strongly suggest that the β_1 state represents a 2D oxide on Pt(100). With higher incident atomic oxygen fluxes, it becomes possible to form 3D oxide domains at 575 K for oxygen coverages greater than 0.63 ML [102].

As shown in Figure 6-1b, the distribution of oxygen states that evolve with increasing coverage changes dramatically when adsorbing at a slightly lower temperature of 450 K. In this case, a new desorption feature at about 650 K, labeled α_2 , intensifies simultaneously with the β_2 peak for coverages ranging from 0.10 ML to 0.40 ML. The α_2 feature continues to grow as the β_1 feature evolves from coverages of 0.40 ML to 0.65 ML. Interestingly, the α_2 state appears to be a disordered oxygen phase that transforms to the surface oxide at a rate that depends on the surface temperature and the oxygen coverage. As discussed previously [68], observing that the α_2 state partially replaces the surface oxide during adsorption at a lower temperature suggests that surface oxide formation is relatively slow at 450 K, and therefore that oxygen atoms become kinetically trapped in the α_2 phase. Given these results, we concluded that the α_2 phase is metastable relative to the surface oxide [68]. Recent studies with Au(111) [117] and Pd(111) [118] show that disordered phases with “added” metal atoms develop as domains with chemisorbed oxygen atoms transform into an ordered surface oxide. We speculate that the metastable phase on Pt(100) has a similar morphology as observed on these other surfaces.

Also seen in Figure 6-1b, there is a small desorption feature, labeled α_1 , that becomes evident at coverages above about 0.50 ML. The α_1 state intensifies as the coverage increases from approximately 0.50 ML to 1.0 ML and exhibits characteristics of second-order desorption. Above 1 ML, the α_1 state appears to diminish while a new desorption feature grows and begins

to shift toward higher temperature, undercutting the traces obtained from lower oxygen coverages. This main desorption peak continues to shift toward higher temperature as the coverage further increases, evolving into an explosive desorption feature as shown in Figure 6-1c. XPS and ELS confirm that the onset of explosive desorption coincides with the initial formation of Pt oxide particles, believed to be PtO₂ [52]. Interestingly, the α_1 state appears to serve as a precursor to bulk 3D oxide formation. Indeed, we recently reported [102] a precursor-mediated mechanism for forming bulk oxide particles on Pt(100) by assuming that the precursor state corresponds to oxygen atoms adsorbed on top of the surface oxide and that these atoms can then either desorb or react with the surface oxide to form 3D oxide.

6.3.2 CO Adsorption on Pt(100)

Before performing CO oxidation rate measurements, we first adsorbed CO on the clean metal at 315 K and conducted TPD. Figure 6-2 shows the TPD traces obtained during these measurements. As expected, the CO TPD spectra are in good agreement with many previous studies [15,18,19,121-124]. We refer the reader to these investigations for additional information regarding CO adsorption on Pt(100). For the present work, we note that CO desorption from the 0.75 ML saturated sample begins at approximately 320 K and that desorption from all coverages is nearly complete by about 550 K. In addition, we note that CO desorption from oxygen-covered Pt(100) (not shown) is complete below room temperature [120] such that we would expect CO concentrations to be very small on regions covered with relatively high oxygen coverages above room temperature.

6.3.3 Reaction with Low Initial Oxygen Coverages

To determine the influence of the oxygen phase distribution on the isothermal oxidation of CO on oxygen-covered Pt(100), we first focused on relatively low initial oxygen coverages generated at 450 K and 575 K. In particular, we generated oxygen coverages up to 1.7 ML using

the atomic oxygen beam, and then performed direct rate measurements by holding the surface at constant temperature and exposing it to a CO molecular beam while monitoring the CO₂ production rate with a QMS. In each measurement, the CO₂ production rate increases abruptly on initiating the CO beam exposure to the surface. Then, the reaction rate increases toward a maximum and decays thereafter to a steady level that is slightly greater than the values obtained before introducing CO into the UHV chamber due to oxidation of CO on the chamber walls. Although not shown in the figures that follow, the CO₂ pressure rapidly returns to its initial value when terminating the CO flow into the chamber. We estimate absolute reaction rates by integrating the 44 amu signal intensity as a function of time and assuming that the signal obtained immediately before terminating the beam flow corresponds to zero reaction rate at the crystal surface. The signal intensity, $I(t)$, is then converted to a rate, $R(t)$, using Equation 6-1, where $[O]_{\text{react}}$ is the amount of adsorbed oxygen that reacts and the upper bound of the integral is taken to be the time just before terminating the CO flow.

$$R(t) = \frac{I(t)[O]_{\text{react}}}{\int_0^{\infty} I(t)dt}, \quad (6-1)$$

More specifically, $[O]_{\text{react}}$ is defined as the initial atomic oxygen coverage less any oxygen atoms that desorb as O₂ and CO₂ in post-reaction TPD measurements. In most cases, this leftover oxygen is less than 0.1 ML and most of this desorbs from subsurface oxygen states as O₂ [59,94,95]. We note that the calculation of $[O]_{\text{react}}$ assumes that oxygen dissolution into the bulk is negligible for the conditions studied here. As discussed below, post-reaction O₂ TPD experiments support this assumption. For convenience, we define apparent CO reaction probabilities as the CO₂ production rates divided by the CO incident flux.

Figure 6-3 shows the temporal evolution of the CO₂ production rates and corresponding reaction probabilities obtained by exposing various oxygen-covered surfaces held at 400 K to a CO molecular beam. Specifically, we examined CO oxidation over surfaces of similar oxygen coverages generated at 575 K and 450 K as depicted in Figure 6-3a and Figure 6-3b, respectively. As seen in the data, the dramatic changes in the oxygen phase distribution associated with the preparation temperature [68] strongly affect the CO₂ production rates. For precoverages less than about 1 ML, the CO₂ production rates increase abruptly upon initiating the CO beam exposure, although the initial rates from surfaces prepared at 575 K are slightly higher than from those prepared at 450 K. Interestingly, increasing the initial oxygen coverage causes the initial CO₂ rate to decrease substantially for precoverages generated at 450 K, while those generated at 575 K appear unaffected. For example, the initial rate from a precoverage of 1.7 ML generated at 450 K is more than an order of magnitude lower than the initial rate from a precoverage of 1.6 ML generated at 575 K.

After beginning the CO exposure, the CO₂ production rates increase almost linearly toward their maximum values, and then decrease rapidly. In all cases, the maximum CO₂ production rates are greater from precoverages prepared at 575 K than those prepared at 450 K for similar oxygen coverages. For example, the maximum rate obtained from a 0.61 ML covered surface generated at 575 K is approximately 0.018 ML s⁻¹, while the maximum rate obtained from a 0.52 ML covered surface generated at 450 K is about 0.012 ML s⁻¹. These rate maxima correspond to reaction probabilities of about 0.58 and 0.41, respectively. With increasing initial oxygen coverage, the exposure required to reach the maximum CO₂ production rate increases. Recently, investigations of CO oxidation on oxygen-covered Pd(100) [107] and Pt(111) [1] surfaces yielded similar results. This effect is substantially more apparent in the data obtained from

surfaces prepared at 450 K. Indeed, comparing a precoverage of 1.6 ML prepared at 575 K with a precoverage of 1.7 ML prepared at 450 K, we find that the exposures required to reach the maximum CO₂ production rates are approximately 0.51 ML and 4.2 ML, respectively. Moreover, the data obtained from an initial oxygen coverage of 1.6 ML (575 K) exhibits a relatively slow decay, similar to that observed for a precoverage of 1.7 ML (450 K), towards the baseline steady-state rate following the maximum, suggesting a slower reaction pathway with 3D oxide. Assuming these two surfaces contain similar total amounts of 3D oxide [102], the data suggests that the local oxide arrangements strongly influence the CO oxidation kinetics. It is worth noting that the general shape of the maxima from the surfaces prepared at the two temperatures also exhibit qualitative differences. Specifically, the maxima obtained from precoverages generated at 575 K are sharp, while those from precoverages generated at 450 K are quite broad. This observation provides further support to concluding there are multiple reaction pathways for CO oxidation with the disordered metastable oxygen state [120] since the individual contributions from different pathways would lead to broader reaction peaks.

To further probe the isothermal oxidation of CO on oxygen-covered Pt(100), we also investigated the influence of the surface temperature during the CO exposure. Figure 6-4 shows the temporal evolution of the CO₂ production rates and corresponding reaction probabilities obtained by exposing (a) a 0.61 ML covered surface prepared at 575 K and (b) a 0.52 ML covered surface prepared at 450 K to a CO molecular beam with the surfaces held at temperatures ranging from 300 K to 550 K. For all temperatures investigated, the general trends discussed above regarding the CO₂ production regimes, shapes, and intensities persist. Regardless of the adlayer preparation temperature, the maximum CO₂ production rate intensifies slightly and occurs at longer CO exposures with increasing sample temperature from 300 K to

400 K. Over this temperature range, the peak slightly narrows with increasing temperature for the 0.61 ML (575 K) covered surface, while the peak broadens for the 0.52 ML (450 K) covered surface. Further increasing the temperature to 450 K during the measurement causes the maximum CO₂ production rates to shift toward even higher CO exposures and the peaks to continue broadening without noticeably affecting the intensities. Interestingly, for both oxygen precoverages there appears to be little difference in the CO₂ production rates for measurements obtained with the sample held at 450 K and 500 K. Finally, increasing the temperature to 550 K causes the maximum intensities to decrease for both oxygen precoverages. However, the maximum continues shifting to higher CO exposures and the peak further broadens for a precoverage of 0.61 ML prepared at 575 K, while for a precoverage of 0.52 ML prepared at 450 K, the peak narrows and sharpens without shifting. Given that the activation energy for CO desorption from oxygen-covered domains is much lower than from the clean metal [120], our data suggests that the CO₂ production rate becomes limited by the steady-state CO concentration on metallic domains since CO desorption begins to compete effectively with adsorption above about 400 K (Figure 6-2).

6.3.4 Reaction with High Initial Oxygen Coverages

We also investigated the reactivity of CO toward 3D bulk-like Pt oxide grown on Pt(100) using direct rate measurements. Figure 6-5 shows the temporal evolution of the CO₂ production rates and corresponding reaction probabilities obtained by exposing Pt(100) surfaces covered with relatively high oxygen concentrations and held at 400 K to a CO molecular beam. Specifically, we examined CO oxidation over surfaces with initial oxygen coverages ranging up to about 4.6 ML prepared at 450 K. Note that the data shown for initial oxygen coverages of 1.0 ML and 1.7 ML represents the same data shown in Figure 6-3.

Figure 6-5 shows that the rate maxima occur after much longer CO exposures when 3D oxide domains are present on the surface. Indeed, the maximum production rate dramatically shifts toward longer exposures with increasing oxygen precoverages, or with greater concentrations of 3D oxide. For example, the rate maxima appear at CO exposures of approximately 7.1 ML, 11.7 ML, and 18.9 ML for initial oxygen coverages of 2.1 ML, 3.0 ML, and 4.2 ML, respectively. With increasing oxygen precoverage, the CO₂ rate curves also broaden significantly. Interestingly, the rate curves appear to be asymmetric, with the leading portion of the curve being a steep function of CO exposure and the trailing portion exhibiting relatively slow decay towards steady state. In other words, the rate curves are skewed towards higher CO exposures. The general trends observed in the oxidation of CO on Pt(100) covered with relatively high initial oxygen concentrations are similar to those reported by Gerrard and Weaver [1] for Pt(111) and Zheng and Altman [107] for Pd(100), although the Pd(100) results appear skewed in the opposite direction toward lower CO exposures.

As mentioned above, the maximum CO₂ production rates shift towards longer CO exposures with increasing initial oxygen coverage. In addition, the rate curves broaden as the initial surface oxygen coverage increases. Interestingly, Figure 6-6 shows that the CO exposure required to reach the maximum CO₂ production rate and the full width at half-maximum of the rate curves both increase linearly with the initial oxygen coverage when the surface is covered with 3D oxide. Specifically, we find that the CO exposure required to reach the rate maximum increases by about 6 ML for each additional monolayer of initial oxygen coverage above 1 ML. Moreover, the full width at half-maximum of the rate curves increases by approximately 2.7 ML for each additional monolayer of oxygen precoverage. Recently, Gerrard and Weaver [1] introduced a model to describe CO oxidation on partially oxidized Pt(111) that predicts that the

CO exposure required to reach the rate maximum increases nearly exponentially with oxygen precoverage. In the present case, we speculate that this model also generally describes CO oxidation on oxygen-covered Pt(100), but the relative rates governing the different reaction steps may strongly affect the observed functional relationship between the initial oxygen coverage and the CO exposure required to reach the rate maxima.

Similar to the measurements detailed above for relatively low oxygen precoverages, we investigated the influence of the surface temperature during the CO exposure for surfaces with relatively high initial oxygen coverages. Specifically, Figure 6-7 shows the temporal evolution of the CO₂ production rates and corresponding reaction probabilities obtained by exposing Pt(100) precovered with (a) 2.1 ML and (b) 4.2 ML of oxygen to a CO molecular beam with the surfaces held at temperatures ranging from 400 K to 550 K. Unlike the data presented in Figure 6-4, we did not observe CO₂ production for oxide-covered surfaces held at 300 K and measured only marginal production for the 2.1 ML precoverage held at 350 K during reasonable CO exposures up to about 60 ML. In general, increasing the surface temperature has a similar effect on the rate behavior as does increasing the initial oxygen coverage at fixed temperature during the exposure. Indeed, for an initial oxygen coverage of 2.1 ML, the rate maxima shift toward longer CO exposures, the maximum production rates decrease, and the rate curves slightly broaden as the temperature increases from 400 K to 550 K. For example, the maximum CO₂ production rate is approximately 0.01 ML s⁻¹ and occurs at an exposure of about 7 ML when the measurement is performed at 400 K, while the maximum rate is approximately 0.006 ML s⁻¹ and occurs at an exposure of about 13.4 ML when the measurement is performed at 550 K. These maximum production rates correspond to reaction probabilities of about 0.33 and 0.2, respectively.

Figure 6-7b shows that the situation is slightly more complex for a surface initially covered by 4.2 ML of oxygen atoms. Here, the maximum CO₂ production rate intensifies and shifts toward shorter CO exposures while the rate curve narrows when increasing the temperature from 400 K to 450 K during the measurement. Thereafter, the general trends seen in Figure 6-7a continue with the rate maxima shifting toward longer CO exposures, the maximum production rate decreasing, and the rate curves broadening with increasing temperature to 550 K. This more general behavior is consistent with previous reports of CO oxidation on Pt(111) [1] and Pd(100) [107] surfaces with relatively high initial oxygen coverages, where the reaction is proposed to occur on lower coverage oxygen phases that coexist with oxide domains. Furthermore, oxygen atoms are thought to migrate from the oxide to these lower coverage regions. Since we expect the surface precovered with 2.1 ML oxygen to contain a mixture of oxide particles and regions with lower oxygen coverage and the surface precovered with 4.2 ML oxygen to be closer to a film of 3D oxide [52], the deviating behavior at low temperature suggests that a slow, direct reaction between CO and bulk-like oxide contributes to the initial reactivity observed at high coverages. Thus, the morphology of the 3D oxide domains appears important in describing the overall reaction mechanism, an observation that is in addition to our previous investigation [120] regarding the influence of the surface oxygen phase distribution.

6.3.5 Partial Reduction of an Oxidized Surface

Finally, we performed TPD after partially reducing a surface initially covered with 4.2 ML of oxygen atoms by exposing it to 23.4 ML CO with the surface held at 400 K. We estimate that 0.59 ML of oxygen remains on the surface following this experiment. Figure 6-8 shows O₂ TPD spectra obtained from surfaces prepared at 450 K with 0.69 ML and 4.2 ML of oxygen atoms and no CO exposure, along with the O₂ TPD spectrum obtained from the partial reduction experiment. Note that the feature observed near 710 K and 720 K from the partially reduced and

initial surfaces, respectively, is consistent with desorption from subsurface oxygen states [59,94,95]. As expected, the primary O₂ desorption feature after partial reduction is much smaller and desorbs about 36 K lower than that obtained from the initial surface.

Strikingly, the TPD trace obtained following the partial reduction experiment appears significantly different from that observed from a similar oxygen coverage prepared with an atomic oxygen beam. Indeed, the desorption feature following reaction remains sharp, while that obtained after adsorbing 0.69 ML of oxygen atoms exhibits multiple peaks. Recall from Figure 6-1 that these peaks correspond to desorption of oxygen atoms adsorbed in an oxide precursor state, 2D surface oxide, and in metastable and disordered (3×1) phases. Thus, the absence of distinct α_1 , β_1 , α_2 , and β_2 desorption features and the sharpness of the O₂ peak suggests that the majority of surface oxygen atoms reside in oxide domains when the oxygen coverage is decreased to at least 0.59 ML by reaction with CO at 400 K. That the partially reduced surface does not appear to decompose and produce the phases exhibited by surfaces covered with similar oxygen coverages without a CO exposure step strongly suggests that the oxide is more stable. These observations agree well with a similar partial reduction measurement performed on Pt(111) [1] and is consistent with prior interpretations of oxygen phase development on Pt(111) [51] and Pt(100) [52]. In these cases, the oxide state is suggested to be thermodynamically preferred over intermediate oxygen phases, but kinetic limitations prevent the 3D oxide from forming [102].

In recent TPRS measurements [120], we observed that CO oxidation on oxygen-covered Pt(100) introduces surface defects that seem to facilitate the diffusion of oxygen atoms into the bulk of the solid. In that case, increasing the initial 3D oxide coverage results in greater amounts of oxygen lost to the bulk as well as higher concentration of surface defects as evidenced by a

distinct desorption feature near 850 K in the O₂ TPD spectra. Unlike these prior results, however, the O₂ desorption rate near 850 K is roughly the same in TPD spectra obtained before and after partial reduction of oxidized Pt(100) for the conditions studied here (Figure 6-8), suggesting that the surface defect levels change negligibly during the isothermal oxidation of CO on Pt(100) above 400 K. Furthermore, since we previously observed a correlation between the oxygen lost to the bulk and the surface defect levels created during reaction [120], the present results also imply that oxygen diffusion into the bulk is relatively unimportant for the reaction conditions studied here. Indeed, this comparison suggests that reaction conditions strongly influence the dissolution of oxygen into the bulk and the associated generation of defect sites. Specifically, the results suggest that CO oxidation at low temperature and relatively high CO coverage enhances the dissolution of oxygen into the bulk and the creation of surface defects, whereas these processes are suppressed when reaction occurs above 400 K and at low CO coverages. While we believe that these results help to justify our assumption that oxygen dissolution was negligible during the isothermal measurements, we emphasize that the absolute CO₂ production rates reported here may represent upper bounds.

6.4 Discussion

The isothermal rate measurements reported here reveal that the oxygen phases which form on Pt(100) below 1 ML are quite active toward CO oxidation whereas the 3D oxide that forms at higher coverage is much less reactive. The results further demonstrate that the CO oxidation kinetics and surface reactivity can depend sensitively on the initial distribution of surface oxygen phases as determined by both the oxygen coverage and the surface temperature during oxygen adsorption. These findings agree well with a recent study in which we used TPRS to investigate CO oxidation on oxygen-covered Pt(100) [120]. Briefly, we found that CO oxidation occurs in roughly three temperature regimes. Between 120 K and 220 K, CO and oxygen react in the

interior of high-density oxygen phase domains, producing CO₂ that evolves into the gas-phase. In this so-called mixed phase regime, reaction occurs readily on the 2D oxide, the metastable oxygen phase, and the (3×1) oxygen phase, whereas direct oxidation of CO adsorbed on the 3D oxide was not observed. The mixed phase regime is followed by a domain-boundary regime from 220 K to 350 K wherein CO adsorbed on metallic surface regions reacts with oxygen atoms that originate from the periphery of oxygen phase domains. These metal regions form as the high-density oxygen phases decompose and likely constitute a mixed state of CO coadsorbed with relatively low concentrations of chemisorbed oxygen atoms, as supported by previous observations [33]. Finally, reaction occurs between CO and relatively isolated oxygen atoms at temperatures above 350 K. We also found that CO desorption from the high-density oxygen phases is complete below 200 K, whereas CO desorbs from the metal surface between 400 K and 500 K (Figure 6-2).

6.4.1 Reactivity of Pt(100) with Initial Oxygen Coverages Below 1 ML

To aid the present discussion, we consider that the total CO₂ production rate, R , can be approximately represented as a sum of local reaction rates on each of the various oxygen phases present on the surface, scaled by the fraction of the surface covered by the respective oxygen phase. Assuming elementary reactions occur between CO and each of the oxygen states, R is then given by Equation 6-2, where A_j is the fractional area of the surface covered by the j^{th} oxygen phase, $k_{r,j}$ is the rate coefficient for reaction on the j^{th} oxygen phase, and $[O]_j$ and $[CO]_j$ are the local oxygen and CO coverages in the j^{th} oxygen phase, respectively.

$$R = \sum_j A_j k_{r,j} [O]_j [CO]_j, \quad (6-2)$$

Based on our recent TPRS results [120], the local CO coverage within each of the high-density oxygen phases will be much lower than on metal regions at surface temperatures greater than

400 K, or $[\text{CO}]_j \ll [\text{CO}]_{\text{metal}}$ where the subscript “metal” signifies metal regions of the surface containing low oxygen concentrations. Thus, the reaction rate coefficients would need to be quite high for direct reaction in the high-density oxygen phases to make an appreciable contribution to the reaction rates observed above 400 K in the current work.

For oxygen-covered surfaces initially containing no metal regions, the initial CO_2 production rate represents reaction directly on the oxygen phases present. Comparing the surfaces initially covered with 0.61 ML (575 K) of primarily 2D oxide and with 0.52 ML (450 K) of a mixture of 2D oxide and metastable oxygen (Figure 6-3), both exhibit initial reaction rates that are relatively high. As such, our results imply that reaction is facile on both the metastable oxygen state and 2D oxide at 400 K; though higher rates obtained from the surface covered solely by 2D oxide suggests that it is more reactive than the metastable oxygen state. These findings are consistent with our previous TPRS investigation [120] reporting that the 2D surface oxide exhibits greater reactivity toward CO oxidation than metastable oxygen. These relatively high initial reaction rates demonstrate that CO oxidation continues to compete effectively with CO desorption from the high-density oxygen phases up to surface temperatures of at least 550 K, even though the CO coverages and surface residence times become very small. For example, CO desorbs from the 2D oxide at about 130 K in TPD [120]; therefore, assuming a normal pre-factor for desorption, we estimate that the characteristic residence time of a CO molecule on the 2D oxide is on the order of 10^{-9} s, and the CO coverage is near 10^{-10} ML at surface temperatures between 400 K and 550 K and a CO incident flux of 0.03 ML s^{-1} .

Consumption of the 2D oxide and the metastable oxygen phase via direct reaction with CO also produces metal regions on which CO can continue to chemisorb and react with oxygen [120], thereby offering an additional CO_2 production pathway. According to Equation 6-2, if

$k_{r,\text{metal}}[\text{CO}]_{\text{metal}}[\text{O}]_{\text{metal}} > k_{r,j}[\text{CO}]_j[\text{O}]_j$, then the total CO_2 production rate will increase during the CO exposure since A_{metal} increases as the fraction of the surface covered by the high-density oxygen phases decreases. Indeed, this agrees with our current results showing that the reaction rates increase nearly linearly upon initiating the CO exposure until reaching their maximum values (Figure 6-3). Thus, the local rate of CO oxidation appears to be higher on metal surface regions than on the 2D oxide and metastable oxygen phases at the conditions of our measurements. This produces autocatalytic kinetics where the measured reaction rate increases as the total oxygen coverage decreases during early reaction times.

While CO oxidation can occur concurrently on the high-density oxygen phases and metal regions, species transport between surface phases may influence the reactive contributions made by the various surface domains. In particular, species transport between phases is likely to reduce the contribution from high-density oxygen phases. For example, our previous TPRS results [120] show that spillover of CO from the high-density oxygen phases onto metallic regions is facile below 200 K. Such spillover depletes the CO concentration within the high-density oxygen phases, thereby lowering the reaction rates within these domains. The additional CO flux into the metal regions can also enhance the reaction rate within the metal domains, but this effect is likely to be small in the present experiments due to the low CO concentrations within the high-density phases. Similarly, oxygen migration from high to low oxygen coverage domains appears to be rapid near the temperatures for appreciable oxygen desorption [52,68], and hence could also influence the CO oxidation kinetics at the lower temperatures studied here. A recent STM investigation by Zheng and Altman [107] provides compelling evidence that oxygen migration is the dominant mechanism governing consumption of the 2D oxide during CO oxidation on Pd(100). Specifically, those researchers observed that 2D oxide domains on Pd(100) diminish in

size rather than breaking apart during reduction by CO at 500 K, implying that direct reaction on the 2D oxide is negligible and that CO reacts primarily within dilute regions of chemisorbed oxygen atoms that are rapidly replenished with oxygen atoms from neighboring 2D oxide domains. As discussed below, oxygen migration appears to play a central role in determining the CO oxidation kinetics when 3D oxide domains are present on Pt(100). However, because of the close kinetic competition between desorption and reaction [120], it is difficult to ascertain the extent to which transport between phases influences the contribution of direct CO oxidation on the 2D oxide and metastable oxygen phases as reaction progresses on Pt(100). STM experiments similar to those reported by Zheng and Altman for Pd(100) [107] could help to illuminate this issue.

6.4.2 Reactivity of Pt(100) Partially Covered by 3D Oxide

The CO₂ production rates observed at high oxygen coverages (Figure 6-5) strongly indicate that the 3D oxide is less reactive toward CO than the oxygen phases that exist at lower coverages. Here, the absolute reaction rates decrease and the rate maxima occur at increasingly longer CO exposures as the amount of 3D oxide on the surface increases. Moreover, the reaction rates remain low for a long time, reaching maximum values at much longer CO exposures than observed in experiments with lower initial oxygen coverages. The low reactivity of the 3D oxide is consistent with our recent study where we did not observe a distinct CO₂ desorption feature associated with direct reaction of CO adsorbed on the 3D oxide during TPRS [120]. In that work, we found that the 3D oxide can accommodate relatively large quantities of adsorbed CO and that the CO desorbs at slightly higher temperatures from the 3D oxide than from the 2D oxide and the metastable oxygen phase. Specifically, the CO desorption temperatures from the 2D oxide, the metastable oxygen phase, and the 3D oxide are 130 K, 157 K and 182 K, respectively. Stronger CO binding yet lower reactivity indicates that the 3D oxide is intrinsically less reactive than the

other high-density oxygen phases toward the direct oxidation of CO, a conclusion that the present isothermal results support. Within the context of Equation 6-2, this implies that the reaction rate coefficient for CO oxidation is lower in the 3D oxide than in the other high-density oxygen phases.

The kinetics for CO oxidation on Pt(100) covered by 3D oxide is analogous to that observed at lower initial oxygen coverages in that the measured reaction rate eventually increases as the oxygen coverage decreases during reaction. However, the surface reactivity appears to decrease more dramatically with increasing initial oxygen coverage when 3D oxide partially covers the surface. Indeed, the time required to reach the maximum reaction rate becomes more sensitive to the initial oxygen coverage above the 1 ML threshold corresponding to the onset of 3D oxide formation (Figure 6-1), as evidenced by a distinct slope change exhibited in Figure 6-6 near this coverage.

As an initial approximation, the observed autocatalytic reaction kinetics may be attributed solely to changes in the surface areas covered by the various oxygen phases. Within the context of Equation 6-2, only the fractional areas of the oxygen phases (A_j) then govern the influence of the total oxygen coverage on the total reaction rate while the local reaction rates on each of the oxygen phases remain constant. Therefore, the total reaction rate increases as the 3D oxide is consumed by reaction with CO since the fractional area of the surface covered by the 3D oxide decreases while that covered by more reactive oxygen domains increases. Given that the 3D oxide has an intrinsic low reactivity toward CO oxidation, 3D oxide reduction will occur relatively slowly, thus requiring longer CO exposures for the measured reaction rates to attain their maximum values than for surfaces with initial oxygen coverages below about 1 ML. Moreover, 3D oxides appear to be more likely to transform into intermediate oxygen phases

during reduction by CO rather than converting directly to metallic regions [107]. As such, the formation of these intermediate phases, such as 2D oxide and the metastable oxygen state, would also delay the onset of high reaction rates since our data suggests that they are less reactive than metal regions of the surface containing relatively low concentrations of chemisorbed oxygen atoms.

The simple approximation offered above assumes that the reaction occurs independently on the various oxygen phases present on the surface at a given total coverage, and that the local reaction rates remain constant during the early reduction period. Under this assumption, the total reaction rate should increase continuously toward a maximum; however, we only observe such behavior for initial oxygen coverages below about 2 ML (Figure 6-5). At higher initial oxygen coverages, the measured reaction rates decay from their initial values and then remain steady for some time before increasing toward a maximum, suggesting that other factors such as kinetic couplings between coexisting surface phases and changing local reaction rates influence the overall reactivity at high oxygen coverages. For these high initial oxygen coverages, it is reasonable to attribute the initial reactivity to direct reaction on the 3D oxide since the surface is primarily covered by 3D oxide. Consequently, the initial rate decays observed for high initial oxygen coverages may indicate that direct CO oxidation depletes the 3D oxide of surface oxygen atoms more quickly than the rates at which these domains transform to intermediate oxygen phases on which reaction can continue. Within the context of Equation 6-2, the total reaction rate initially decreases with time because the contribution offered by the local reaction rate on the 3D oxide decreases initially and the slow formation of intermediate oxygen phases causes the fractional area of the surface covered by these phases to remain low when the total oxygen coverage is high.

Our prior TPRS investigation indicates that migration of Pt and oxygen atoms from high- to low-coverage phases can also play a role in the CO oxidation kinetics [120]. Indeed, such migration provides an alternate pathway for the transformation of the 3D oxide into more reactive oxygen phases that can affect the measured reaction rate. Recently, Gerrard and Weaver [1] presented a kinetic model that assumes that 3D oxide domains on Pt(111) transform directly into metal regions and that oxygen atoms migrate from the 3D oxide to these metal regions to sustain the reaction. While their model seems to capture key mechanistic aspects of CO oxidation on the Pt(111) surface partially covered by 3D oxide, our prior studies of Pt(100) oxidation [102] suggest that the 3D oxide is more likely to transform to intermediate oxygen phases rather than decomposing directly to metal regions. In that work, we reported that the kinetics for 3D oxide formation on Pt(100) is well described by a precursor-mediated mechanism whereby oxygen atoms adsorbed on top of the 2D oxide react with the 2D oxide to produce a 3D oxide particle. Furthermore, we have also described the self-accelerating decomposition of oxidized Pt(100), which gives rise to sharp O₂ desorption peaks (Figure 6-1), in terms of a mechanism where oxygen atoms migrate from 3D oxide domains to a dilute phase from which associative desorption occurs [51,52]. Taken together, and considering microscopic reversibility, these studies suggest that the 3D oxide thermally decomposes by generating 2D oxide domains and precursor oxygen atoms adsorbed on top of the 2D oxide, and that oxygen desorbs predominately from this precursor state until the 3D oxide domains are nearly exhausted. In other words, the same precursor state likely mediates both 3D oxide formation and decomposition.

It is reasonable to assume that this indirect pathway for 3D oxide consumption involving oxygen migration onto neighboring 2D oxide domains occurs during surface reduction by CO

and plays an important role in determining the observed CO oxidation kinetics. In particular, precursor oxygen atoms adsorbed on top of the 2D oxide may compete with CO for binding sites on the 2D oxide, thereby impeding reaction on an otherwise reactive oxygen phase. Such site blocking may explain the low initial CO oxidation rate obtained for an initial oxygen coverage of 1 ML prepared at 450 K compared with that exhibited by a surface precovered with 0.52 ML of oxygen atoms at 450 K (Figure 6-4). Indeed, the initial CO₂ production rate is as low for the 1 ML oxygen-covered surface as those observed from surfaces with higher initial oxygen coverages even though the 3D oxide covers only a small fraction of the surface. However, the O₂ TPD spectra also show significant desorption in the low-temperature precursor state (Figure 6-1), which we have attributed previously to oxygen atoms adsorbed on top of the 2D oxide [52,102]. Therefore, the concentration of the precursor oxygen state is relatively high for the 1 ML covered surface, effectively lowering the reactivity of the 2D oxide domains by keeping the CO concentration low. Interestingly, we did not observe evidence for a reaction between CO and oxygen adsorbed on top of the 2D oxide in our TPRS study [120], which may indicate that the adsorbed oxygen atoms tend to preferentially fill vacancies in the 2D oxide created by reaction with CO.

The model reported by Gerrard and Weaver [1] predicts that site blocking is largely responsible for the long CO exposures required to achieve high CO oxidation rates when 3D oxide is initially present on the surface. According to the model, when the fractional surface area covered by the 3D oxide, A_{3D} , is sufficiently large, rapid oxygen migration maintains high oxygen concentrations in the dilute phase that impede CO adsorption and keep the CO oxidation rate low. Once A_{3D} drops below a critical value, the oxygen migration rate falls below the CO adsorption rate, causing CO to consume oxygen atoms in the dilute phase faster than they are

supplied. As a result, the CO oxidation rate begins to increase rapidly with CO exposure time, similar to the experimental observations. It is conceivable that a similar migration of oxygen atoms from the 3D oxide into the precursor state on top of the 2D oxide also occurs during CO oxidation on Pt(100), and is partly responsible for the long exposure times required for the CO oxidation rate to begin increasing appreciably. A potential shortcoming of this interpretation is that the model presented by Gerrard and Weaver [1] significantly overestimates the CO exposures required to reach the maximum CO₂ production rates, predicting a nearly exponential increase with increasing initial oxygen coverage as opposed to the linear dependence observed in the present investigation (Figure 6-6). Nevertheless, the model likely correctly captures many of the key mechanistic features of the reaction, but the details regarding the dependence of CO adsorption and oxygen migration rates on local coverages may differ from those invoked by the model. In addition, the manner in which the fraction of the surface covered by the 3D oxide evolves during oxygen uptake and reduction may be different from that assumed. Ultimately, detailed structural information, perhaps utilizing STM, is required to test these ideas and better understand the reaction mechanism.

Intriguingly, the data shown in Figure 6-3 indicates that the morphology of oxide domains is also important in describing the CO oxidation reaction. In this case, comparing oxygen precoverages of 1.6 ML and 1.7 ML prepared at 575 K and 450 K, respectively, we find that the CO exposure required to reach the maximum CO₂ production rate is markedly higher for the oxygen-covered surface generated at 450 K. If we assume that these two surfaces contain the same total amounts of 3D oxide as suggested previously [102], and that the CO oxidation reaction proceeds as discussed above, then the data indicates that the local arrangement of the 3D oxide strongly influences the reaction kinetics. For instance, the short CO exposure required to

reach the maximum rate for the 1.6 ML precovered surface prepared at 575 K suggests that reactive oxygen phases occupy a relatively larger area of the surface, and the 3D oxide a relatively smaller area, than the surface initially prepared at 450 K with 1.7 ML of oxygen. In other words, we speculate that the 3D oxide domains on the surface generated at 575 K are taller, or their projection onto the surface is smaller, than the domains on the surface generated at 450 K, which cover a larger area of the surface. Therefore, these findings indicate that, in addition to the total oxygen coverage, the oxide morphology must also be considered when discussing the CO oxidation reaction on the oxygen-covered Pt(100) surface.

6.5 Summary

We utilized direct, isothermal rate measurements to examine the reaction between CO molecular beams and oxygen atoms adsorbed in various surface phase distributions on Pt(100) under UHV conditions. Specifically, we examined CO oxidation on oxygen-covered surfaces generated at 450 K and 575 K to study the reactivity of oxygen atoms in a (3×1) chemisorbed phase, a disordered metastable phase, an ordered 2D oxide, and 3D oxide particles at temperatures between 400 K and 550 K. We find that the metastable oxygen phase and the 2D surface oxide are active toward CO oxidation at the conditions investigated, with the 2D oxide exhibiting greater reactivity. This finding demonstrates that CO oxidation continues to compete effectively with desorption from the metastable oxygen phase and the 2D oxide up to at least 550 K and a CO incident flux of 0.03 ML s^{-1} , despite the weak binding of CO on these phases. Our results further reveal that the reaction takes place at higher rates on metallic regions of the surface that form as the 2D oxide and metastable oxygen phases are consumed by reaction, leading to reaction rates that increase as the total oxygen coverage initially decreases during reaction.

The CO oxidation rate diminishes significantly as the amount of 3D Pt oxide domains on the surface increases due to a strong preference for CO desorption versus reaction on the 3D oxide. Similar to the behavior observed at initial oxygen coverages below 1 ML, the measured CO oxidation kinetics is autocatalytic at high oxygen coverage, but much longer CO exposures are required to attain appreciable reaction rates. We attribute this behavior partly to the low rates of direct CO oxidation on the 3D oxide which delay the consumption of the 3D oxide and hence the generation of more reactive surface domains. The results at intermediate oxygen coverage suggest that site blocking may also be partly responsible for the low reaction rates observed at high coverage. Prior results [120] show that the 3D oxide decomposes concurrently by an indirect pathway involving the migration of oxygen atoms from the 3D oxide onto coexisting oxygen phases. We speculate that oxygen-atom migration from the 3D oxide into an adsorbed state on top of the 2D oxide competes with CO adsorption onto the 2D oxide, and that this competition suppresses CO adsorption and hence reaction on the 2D oxide when the 3D oxide coverage is relatively high. Finally, our results demonstrate that the morphology of the 3D oxide on the surface can strongly influence the kinetics, and should therefore be considered in a kinetic description of CO oxidation on partially oxidized Pt(100). Collectively, these results provide continuing support to the growing experimental evidence that oxidized Pt is less reactive toward CO oxidation than chemisorbed oxygen atoms adsorbed on the Pt surface.

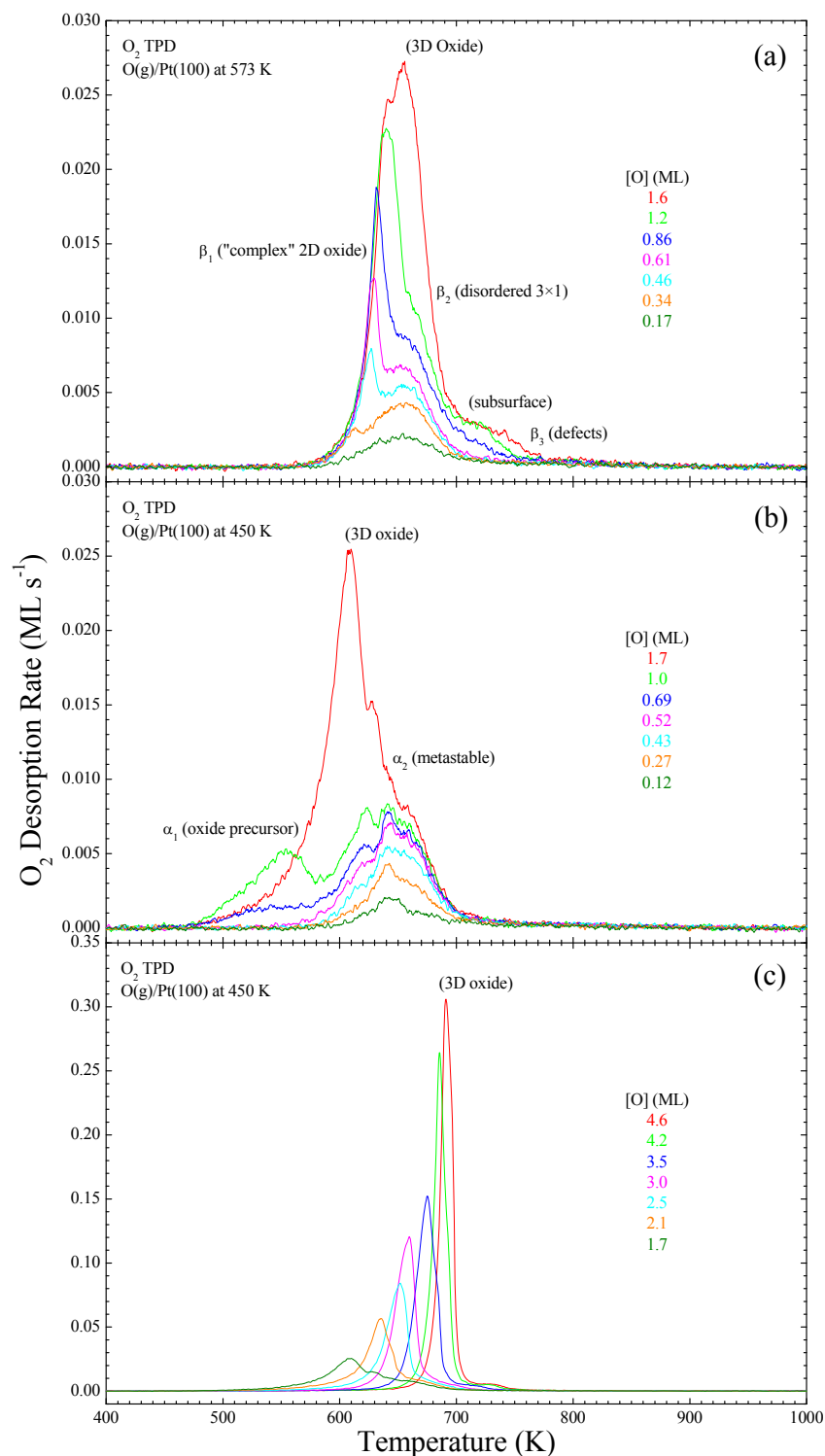


Figure 6-1. O_2 TPD spectra (temperature ramp = $1\ K\ s^{-1}$) obtained after exposing Pt(100) at (a) 575 K and (b, c) 450 K to an atomic oxygen beam. Note that the data from the highest coverage presented in (b) is the same as that for the lowest coverage presented in (c).

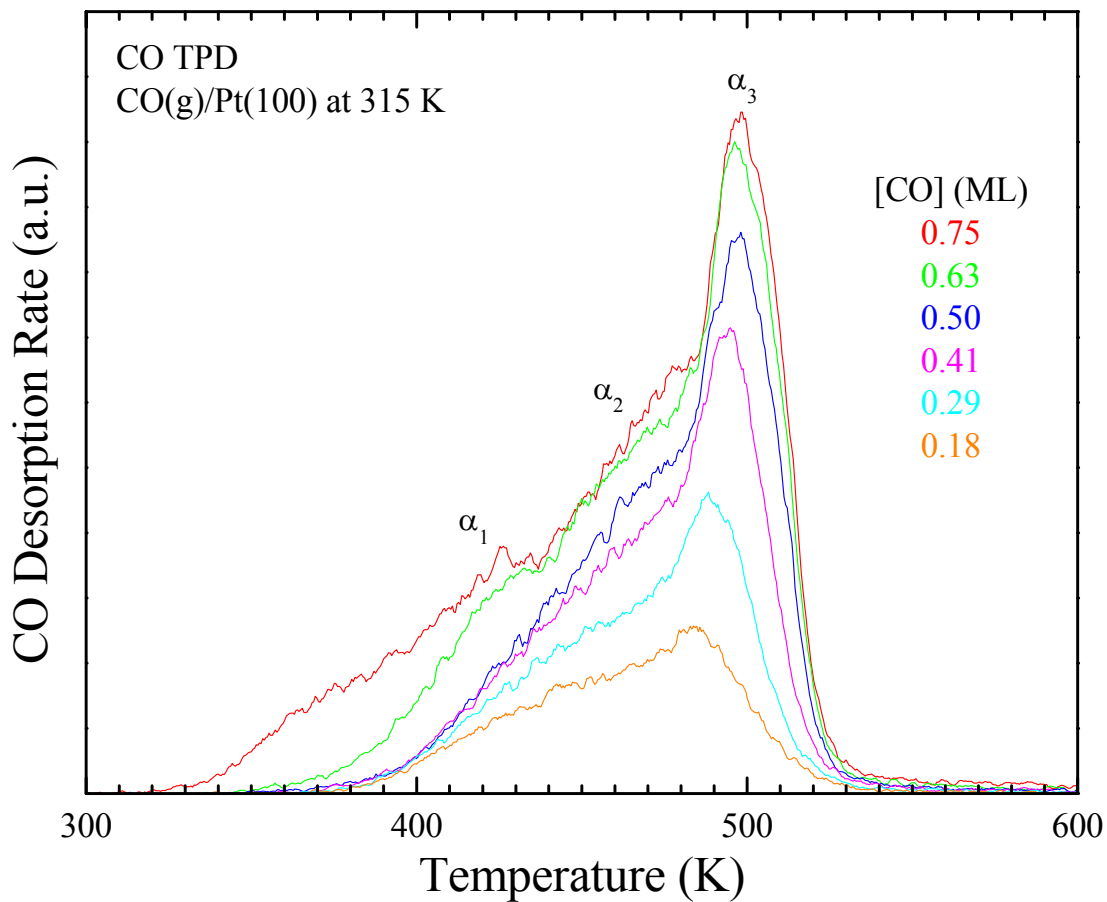


Figure 6-2. CO TPD spectra (temperature ramp = 1 K s^{-1}) obtained after exposing Pt(100) at 315 K to a CO molecular beam.

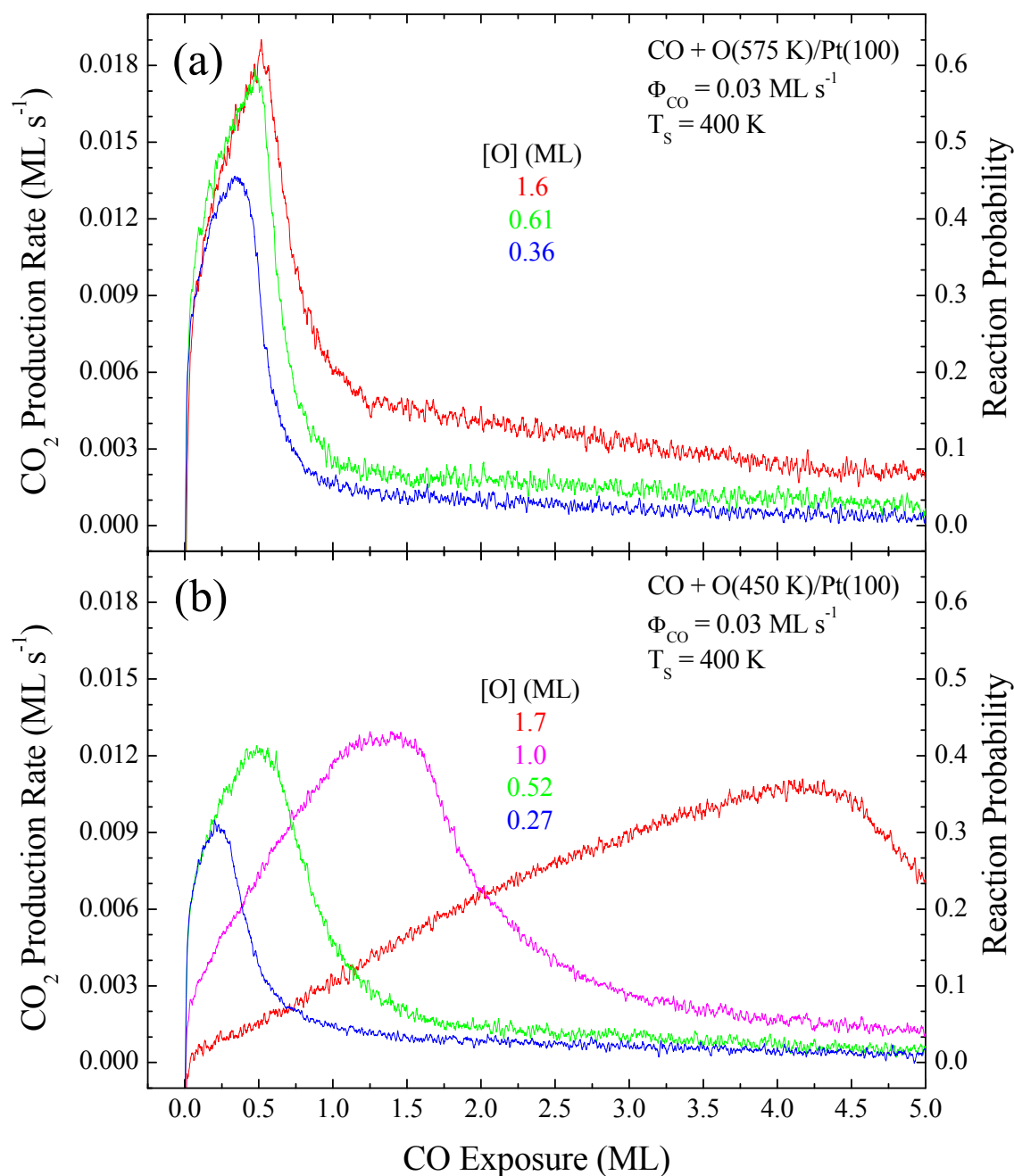


Figure 6-3. CO₂ production rates and corresponding reaction probabilities obtained by exposing various oxygen-covered surfaces held at 400 K to a CO molecular beam. The measurements started with initial oxygen coverages of (a) 0.36 ML, 0.61 ML, and 1.6 ML generated at 575 K and (b) 0.27 ML, 0.52 ML, 1.0 ML, and 1.7 ML generated at 450 K.

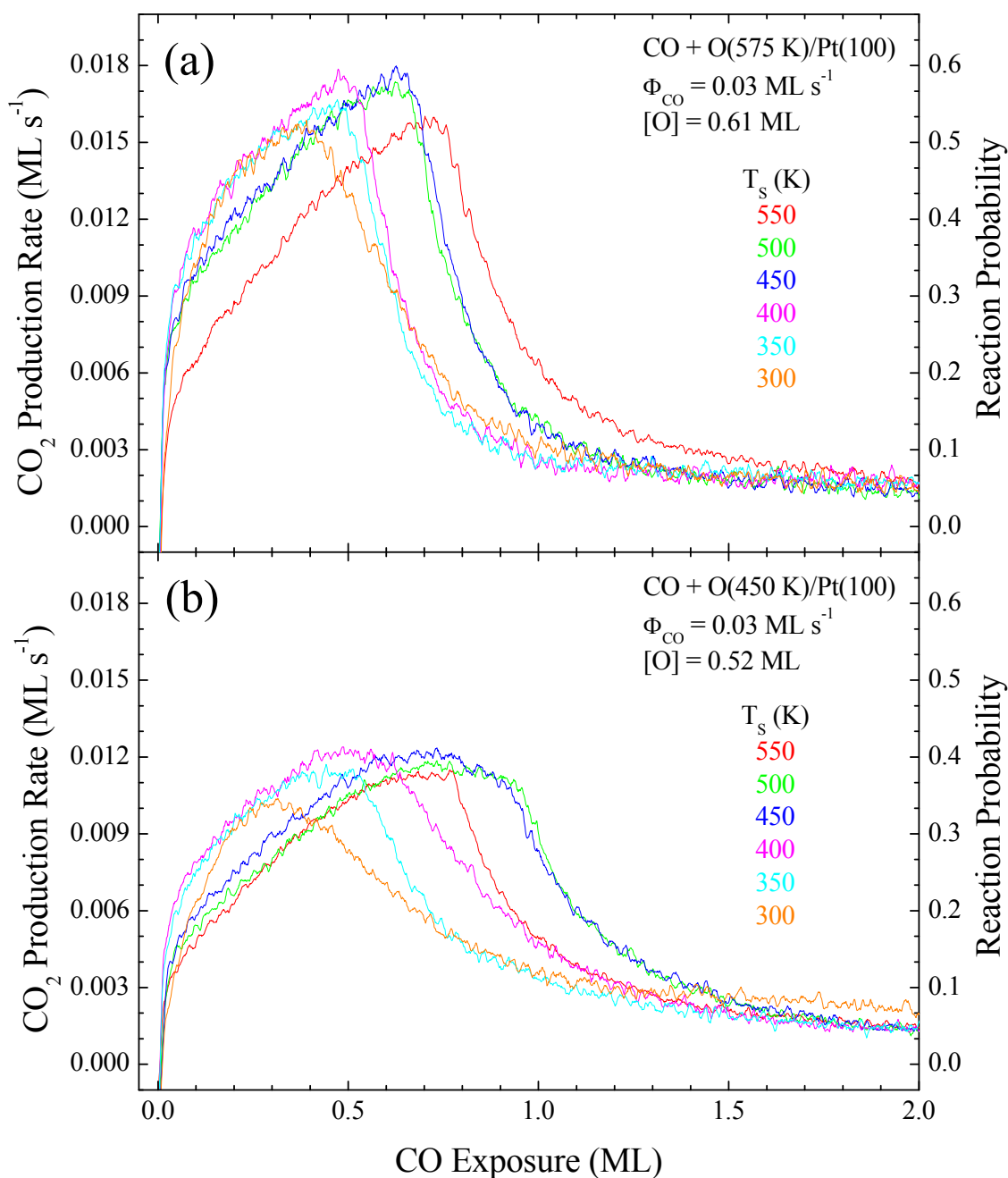


Figure 6-4. CO₂ production rates and corresponding reaction probabilities obtained by exposing (a) a 0.61 ML oxygen-covered surface prepared at 575 K and (b) a 0.52 ML oxygen-covered surface prepared at 450 K to a CO molecular beam with the surfaces held at temperatures ranging from 300 K to 550 K.

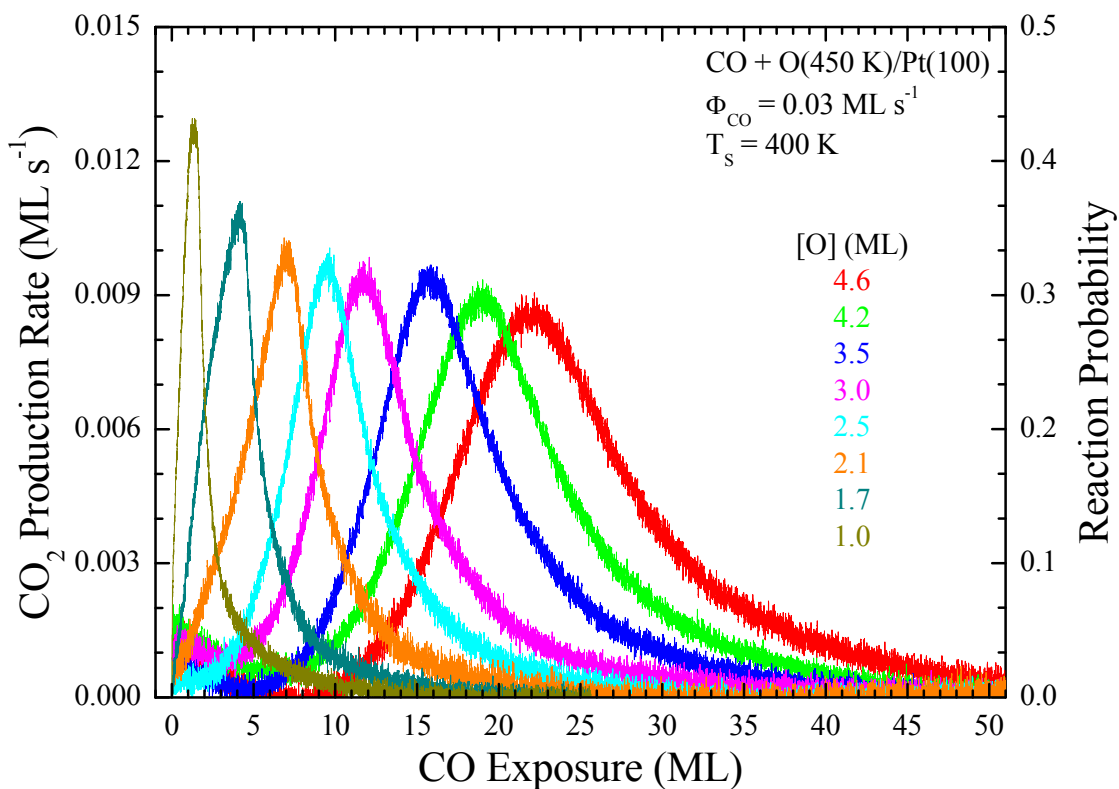


Figure 6-5. CO₂ production rates and corresponding reaction probabilities obtained by exposing oxygen-covered Pt(100) surfaces held at 400 K to a CO molecular beam. The measurements started with initial oxygen coverages of 1.0 ML, 1.7 ML, 2.1 ML, 2.5 ML, 3.0 ML, 3.5 ML, 4.2 ML, and 4.6 ML generated at 450 K.

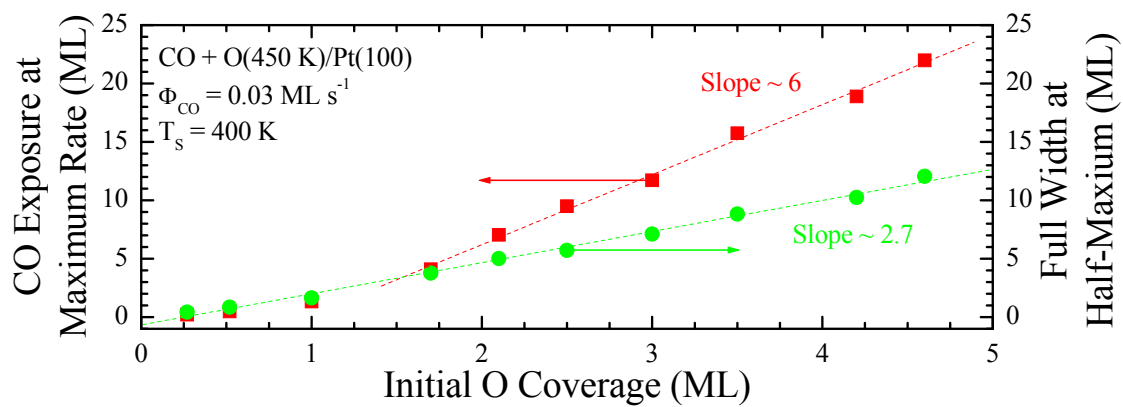


Figure 6-6. Plot showing that the CO exposure required to reach the maximum CO_2 production rate and the full width at half-maximum of the rate curves both increase linearly with the initial oxygen coverage when the Pt(100) surface is partially covered with 3D oxide.

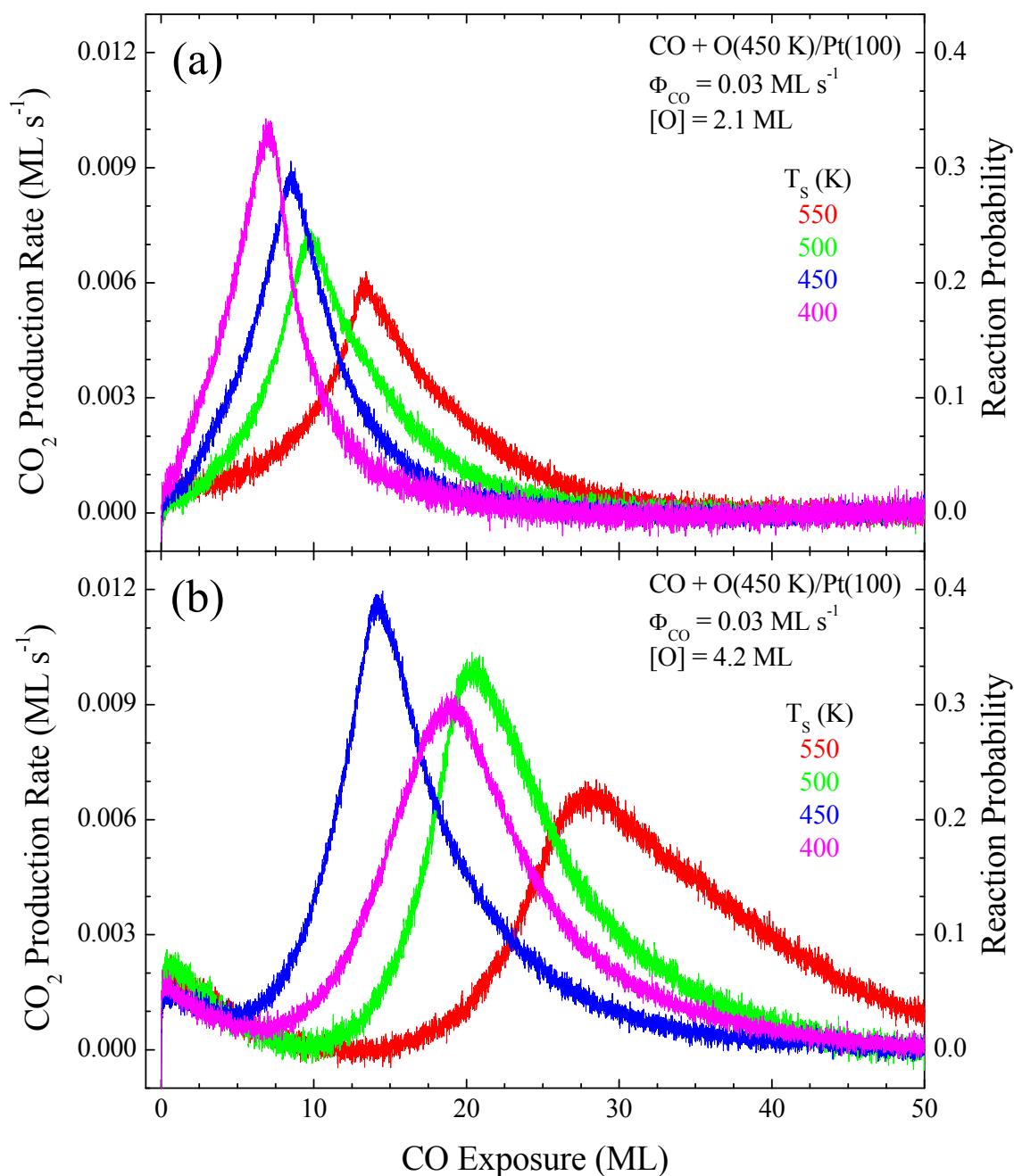


Figure 6-7. CO₂ production rates and corresponding reaction probabilities obtained by exposing Pt(100) precovered with (a) 2.1 ML and (b) 4.2 ML of oxygen generated at 450 K to a CO molecular beam with the surfaces held at temperatures ranging from 400 K to 550 K.

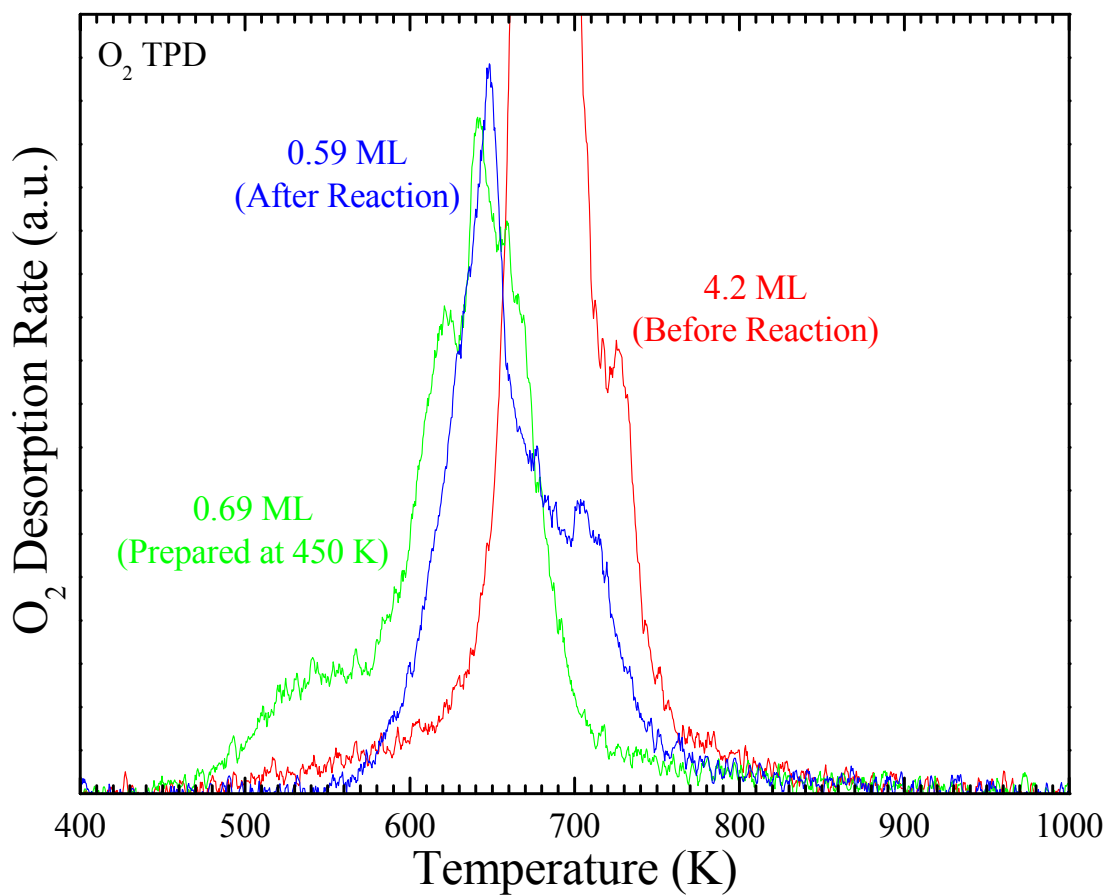


Figure 6-8. O₂ TPD traces (temperature ramp = 1 K s⁻¹) obtained from 4.2 ML and 0.69 ML of oxygen atoms prepared on Pt(100) at 450 K by adsorption from an oxygen-atom beam and after approximately 23.4 ML of CO partially reduces the 4.2 ML covered surface at 400 K to an oxygen coverage of 0.59 ML.

CHAPTER 7 CONCLUSION

7.1 Synopsis

The oxidation of Pt and other late transition metals is central to many applications of heterogeneous catalysis, including fuel processing applications, the selective oxidation of organic compounds, and pollution control of combustion products. Certainly, the active surface of a transition-metal catalyst can be in an oxidized state under the operating conditions typical of these catalytic processes. Moreover, since transition metals and their oxides usually exhibit different chemisorptive and reactive properties, the extent of surface oxidation can significantly affect catalyst performance. Given that a variety of oxygen states can exist on transition-metal surfaces and that these states can interact uniquely with reactant molecules, there is substantial motivation for pursuing a deeper understanding of the oxidation of late transition-metal surfaces. However, the vast array of potential catalytic surfaces available necessitates focusing studies to low-index, single-crystalline surfaces that have traditionally been used to model reaction systems. As such, the present work provides details of recent investigations into the growth, properties, and reactivity of high-concentration oxygen phases on the Pt(100) surface.

In examining the adsorption of gas-phase oxygen atoms on the Pt(100) surface, we find that the types and relative populations of oxygen phases that develop are highly dependent on the surface temperature during adsorption for relatively low oxygen coverages. At 450 K, a disordered, high-concentration oxygen state preferentially forms at the expense of an ordered, 2D surface oxide that populates at a surface temperature of ~ 575 K, presumably due to kinetic barriers hindering the formation of the 2D oxide. Thus, the disordered state appears to be metastable relative to the surface oxide. For higher coverages, oxygen atoms apparently adsorb on top of the surface oxide, acting as a precursor to forming 3D, bulk-like oxide particles. By

varying the incident oxygen-atom flux, we investigated the kinetics governing this transition from 2D to 3D oxide growth, and show that a model assuming that precursor oxygen atoms adsorbed on the 2D oxide can either associatively desorb or react with the 2D oxide to form a 3D oxide particle quantitatively reproduces the measured kinetics. From an analysis of the data, we estimate that the formation rate of a 3D oxide nucleus has a fourth-order dependence on the coverage of these precursor oxygen atoms, thus implying a critical configuration for oxide nucleus formation requiring four precursor oxygen atoms. Interestingly, thermodynamic considerations show that the thermal stability of these 3D oxide particles significantly exceeds that of bulk PtO₂, suggesting that similarly large kinetic barriers hinder the decomposition of the 3D oxide as further evidenced by explosive O₂ desorption during TPD.

Having developed a better understanding of the growth and properties of high-concentration oxygen phases on the Pt(100) surface, we examined the reactivity of these phases toward the oxidation of CO. By adsorbing CO on oxygen-covered Pt(100) at low temperature and utilizing TPRS, we find that the reaction is facile on oxygen phases that form below coverages of about 1 ML and inefficient when 3D oxide particles partially cover the surface. Direct, isothermal reaction measurements at higher temperatures provide additional support for these findings. Our work shows that the reactivity toward CO is highest for the 2D oxide and decreases in the order of metastable oxygen, oxygen chemisorbed in a disordered (3×1) phase, and 3D oxide. Given that we observe relatively weak CO binding within the 2D oxide and metastable oxygen phase, we find that reaction at higher temperatures also occurs on metallic regions of the surface covered with relatively low concentrations of chemisorbed oxygen atoms, and that neighboring high-density oxygen phases serve as an oxygen source for these metallic regions.

For CO oxidation measurements on surfaces partially covered by 3D oxide, reaction at higher temperatures generally occurs on reactive dilute oxygen phases surrounding 3D oxide domains with oxygen atoms migrating from the oxide to these dilute phases. However, influences coupling the oxygen and CO concentrations within the various phases and the migration rate of these species between phases complicate the kinetics. We suspect that the relative inactivity of 3D oxide toward CO is likely due to kinetic barriers associated with the creation and transport of Pt adatoms, such that CO can react with the 3D oxide but at a much slower rate than the oxygen phases that form at lower coverages. Interestingly, in TPRS we observe significant surface defect formation and oxygen loss to the bulk during reaction with the surface partially covered by oxide domains. At higher temperatures, we further observe that the morphology of the 3D oxide strongly influences the kinetics. These results provide additional support to the growing evidence that oxidized Pt is less reactive toward CO oxidation than the oxygen phases that form at intermediate coverages.

7.2 Future Considerations

7.2.1 Structural Investigations

The experiments discussed in the present work offer significant advances toward understanding the oxidation of Pt and other late transition metals, however many questions remained unanswered. For example, while our work demonstrates that significant restructuring occurs as the surface oxygen coverage increases, the real-space structure of the various intermediate oxygen phases and the oxides are unresolved. Future work, likely utilizing STM methods, should attempt to characterize the real-space structures of the disordered (3×1) oxygen phases, metastable oxygen state, 2D oxide, and 3D oxide. Moreover, future investigations focusing on the structural nature of the oxide precursor state will likely contribute to a better understanding of the kinetics governing 3D oxide formation. Finally, future investigations

detailing the structural transitions that occur as the surface oxygen and oxide phases decompose or react will aid in developing a more comprehensive kinetic model describing these processes.

7.2.2 Reactivity Studies

While the experiments discussed in the present work suggest that 3D oxide formed on Pt(100) is inactive to CO relative to oxygen phases that develop at intermediate coverages, future investigations should further explore the reactivity of oxygen-covered Pt(100) using reactants other than CO. For example, NO oxidation is of particular relevance to the remediation of combustion effluent products, and there is therefore ample motivation for future investigations into NO oxidation over Pt(100) surfaces covered with high-concentration oxygen phases. Given the current controversy surrounding the relative reactivity of 3D oxide, especially towards CO oxidation, on Pt surfaces as discussed in Section 1.1, future work should pay particular attention to the experimental conditions. Indeed, since it is plausible that O₂ adsorbed on top of the 3D oxide is reactive toward CO rather than the 3D oxide itself under high-pressure conditions, future research should consider the possibility that O₂ or oxygen atoms can adsorb on top of the oxide and investigate the relative reactivity of these oxygen species, perhaps by utilizing isotopic labeling techniques.

7.2.3 Computational Modeling

With the recent rapid technological advances in computers, particularly in terms of their increasing speed and decreasing costs, computational modeling techniques are becoming increasingly popular and powerful. As such, future investigations involving oxygen-covered Pt(100) should attempt to utilize such computational methods, like DFT, to aid in interpreting experimental data and calculating parameters for use in kinetic models. Of particular relevance to the work presented herein, computational modeling could enhance our understanding of the transition from 2D to 3D oxide formation. While the structural investigations suggested above

may present a clearer picture of the oxide precursor state, computational methods may be the most efficient way to calculate energy barriers. Therefore, their utility for enhancing a kinetic description of the processes governing 3D oxide formation provides ample motivation for future experimental investigations complemented by computational modeling. Similar advantages offered by computational methods can be exploited to complement future structural and reactivity investigations as discussed above.

7.2.4 Generality of Findings

The experiments described within provide results that are specific to the Pt(100) surface; however, it remains unclear whether the findings are generally applicable to other transition-metal surfaces. Moreover, it is unclear whether these findings are relevant to similar processes on other crystalline planes of Pt. For instance, the precursor-mediated model presented to describe the transition from 2D to 3D oxide formation may be a more general phenomenon. Indeed, it is certainly plausible that large kinetic barriers hinder oxide formation on other transition-metal surfaces and that precursor oxygen atoms precede the growth of 3D oxide particles. Future investigations should aim to determine whether other transition metals experience precursor-mediated oxide growth and, if so, determine whether the nature of the precursor oxygen atoms is general. It is also plausible that oxide decomposition occurs via similar processes on various transition-metal surfaces, and future studies should therefore attempt to distinguish these similarities and differences. Finally, future work should consider examining whether the crystalline face influences the reactivity of the oxygen phases that develop. Indeed, while our work shows that the 3D oxide is relatively inactive toward CO oxidation on Pt(100), it is conceivable that using a different crystalline face of Pt will allow a more active 3D oxide surface to develop. Future investigations should consider this possibility.

LIST OF REFERENCES

- [1] A.L. Gerrard, J.F. Weaver, *J. Chem. Phys.* 123 (2005) 224703.
- [2] B.L.M. Hendriksen, J.W.M. Frenken, *Phys. Rev. Lett.* 89 (2002) 046101.
- [3] M.D. Ackermann, T.M. Pedersen, B.L.M. Hendriksen, O. Robach, S.C. Bobaru, I. Popa, C. Quiros, H. Kim, B. Hammer, S. Ferrer, J.W.M. Frenken, *Phys. Rev. Lett.* 95 (2005) 255505.
- [4] N. Seriani, W. Pompe, L.C. Ciacchi, *J. Phys. Chem. B* 110 (2006) 14860.
- [5] T.M. Pedersen, W.X. Li, B. Hammer, *Phys. Chem. Chem. Phys.* 8 (2006) 1566.
- [6] W.X. Li, B. Hammer, *Chem. Phys. Lett.* 409 (2005) 1.
- [7] M.S. Chen, Y. Cai, Z. Yan, K.K. Gath, S. Axnanda, D.W. Goodman, *Surf. Sci.* 601 (2007) 5326.
- [8] R.B. Getman, W.F. Schneider, *J. Phys. Chem. C* 111 (2007) 389.
- [9] P.R. Norton, J.A. Davies, D.K. Creber, C.W. Sitter, T.E. Jackman, *Surf. Sci.* 108 (1981) 205.
- [10] K. Heinz, E. Lang, K. Strauss, K. Müller, *Appl. Surf. Sci.* 11-12 (1982) 611.
- [11] K. Heinz, E. Lang, K. Strauss, K. Müller, *Surf. Sci.* 120 (1982) L401.
- [12] M.A. van Hove, R.J. Koestner, P.C. Stair, J.P. Bibérian, L.L. Kesmodel, I. Bartoš, G.A. Somorjai, *Surf. Sci.* 103 (1981) 189.
- [13] P. Heilmann, K. Heinz, K. Müller, *Surf. Sci.* 83 (1979) 487.
- [14] A.E. Morgan, G.A. Somorjai, *Surf. Sci.* 12 (1968) 405.
- [15] M.A. Barteau, E.I. Ko, R.J. Madix, *Surf. Sci.* 102 (1981) 99.
- [16] K. Griffiths, T.E. Jackman, J.A. Davies, P.R. Norton, *Surf. Sci.* 138 (1984) 113.
- [17] A. Hopkinson, J.M. Bradley, X.C. Guo, D.A. King, *Phys. Rev. Lett.* 71 (1993) 1597.
- [18] A. Hopkinson, X.-C. Guo, J.M. Bradley, D.A. King, *J. Chem. Phys.* 99 (1993) 8262.
- [19] P.A. Thiel, R.J. Behm, P.R. Norton, G. Ertl, *J. Chem. Phys.* 78 (1983) 7448.

- [20] M.A. van Hove, R.J. Koestner, P.C. Stair, J.P. Bibérian, L.L. Kesmodel, I. Bartoš, G.A. Somorjai, *Surf. Sci.* 103 (1981) 218.
- [21] P.R. Norton, P.E. Bindner, K. Griffiths, *J. Vac. Sci. Technol. A* 2 (1984) 1028.
- [22] C.R. Helms, H.P. Bonzel, S. Kelemen, *J. Chem. Phys.* 65 (1976) 1773.
- [23] B. Lang, P. Légaré, G. Maire, *Surf. Sci.* 47 (1975) 89.
- [24] G. Kneringer, F.P. Netzer, *Surf. Sci.* 49 (1975) 125.
- [25] G.N. Derry, P.N. Ross, *Surf. Sci.* 140 (1984) 165.
- [26] P.R. Norton, K. Griffiths, P.E. Bindner, *Surf. Sci.* 138 (1984) 125.
- [27] X.-C. Guo, J.M. Bradley, A. Hopkinson, D.A. King, *Surf. Sci.* 310 (1994) 163.
- [28] I. Langmuir, *Trans. Faraday Soc.* 17 (1922) 621.
- [29] T. Engel, G. Ertl, *Adv. Catal.* 28 (1979) 1; and references therein.
- [30] R. Imbihl, G. Ertl, *Chem. Rev.* 95 (1995) 697; and references therein.
- [31] G. Ertl, P.R. Norton, J. Rüstig, *Phys. Rev. Lett.* 49 (1982) 177.
- [32] G. Brodén, G. Pirug, H.P. Bonzel, *Surf. Sci.* 72 (1978) 45.
- [33] R.J. Behm, P.A. Thiel, P.R. Norton, P.E. Bindner, *Surf. Sci.* 147 (1984) 143.
- [34] M.A. Barteau, E.I. Ko, R.J. Madix, *Surf. Sci.* 104 (1981) 161.
- [35] E. Bechtold, *Surf. Sci.* 115 (1982) L125.
- [36] V.V. Gorodetskii, A.V. Matveev, P.D. Cobden, B.E. Nieuwenhuys, *J. Mol. Catal. A: Chem.* 158 (2000) 155.
- [37] V.V. Gorodetskii, A.V. Matveev, E.A. Podgornov, F. Zaera, *Top. Catal.* 32 (2005) 17.
- [38] J.F. O'Hanlon, *A user's guide to vacuum technology*, 3rd ed., Hoboken, NJ Wiley-Interscience, 2003.

- [39] R.I. Masel, Principles of adsorption and reaction on solid surfaces, Hoboken, NJ: Wiley-Interscience, 1996.
- [40] A.L. Gerrard, Interactions of atomic oxygen with Pt(111) and nitrided Si(100), Gainesville, FL: University of Florida, 2005.
- [41] A.L. Gerrard, J.-J. Chen, J.F. Weaver, J. Phys. Chem. B 109 (2005) 8017.
- [42] J.T. Yates, Experimental Innovations in Surface Science: A Guide to Practical Laboratory Methods and Instruments, New York, NY: AIP Press, 1998.
- [43] H.H. Kan, R.B. Shumbera, J.F. Weaver, J. Chem. Phys. 126 (2007) 134704.
- [44] D.A. King, Surf. Sci. 47 (1975) 384.
- [45] P.A. Redhead, Vacuum 12 (1962) 203.
- [46] W.M. Riggs, M.J. Parker, "Surface analysis by X-ray photoelectron spectroscopy" in Methods of surface analysis, edited by A.W. Czanderna, New York, NY: Elsevier Scientific Publishing Company, 1975.
- [47] C.D. Wagner, W.M. Riggs, L.E. Davis, J.F. Moulder, Handbook of X-ray photoelectron spectroscopy, 1st ed., edited by G.E. Muilenberg, Eden Prairie, MN: Perkin-Elmer Corporation (Physical Electronics), 1979.
- [48] G. Ertl, J. Küppers, Low energy electrons and surface chemistry, 2nd ed., Weinheim, Federal Republic of Germany: VCH Verlagsgesellschaft, 1985.
- [49] R.E.R. Colen, J. Christoph, F. Peña, H.H. Rotermund, Surf. Sci. 408 (1998) 310.
- [50] J. Dicke, H.H. Rotermund, J. Lauterbach, Surf. Sci. 454-456 (2000) 352.
- [51] J.F. Weaver, J.-J. Chen, A.L. Gerrard, Surf. Sci. 592 (2005) 83.
- [52] R.B. Shumbera, H.H. Kan, J.F. Weaver, Surf. Sci. 601 (2007) 235.
- [53] A.T. Pasteur, S.J. Dixon-Warren, D.A. King, J. Chem. Phys. 103 (1995) 2251.

- [54] A. Borg, A.-M. Hilmen, E. Bergene, Surf. Sci. 306 (1994) 10.
- [55] R.J. Behm, P.A. Thiel, P.R. Norton, G. Ertl, J. Chem. Phys. 78 (1983) 7437.
- [56] N.A. Deskins, J. Lauterbach, K.T. Thomson, J. Chem. Phys. 122 (2005) 184709.
- [57] Y. Matsumoto, Y. Aibara, K. Mukai, K. Moriwaki, Y. Okawa, B.E. Nieuwenhuys, K. Tanaka, Surf. Sci. 377-379 (1997) 32.
- [58] C.P. Oliver, B.V. King, D.J. O'Connor, Surf. Sci. 561 (2004) 33.
- [59] H.H. Rotermund, J. Lauterbach, G. Haas, Appl. Phys. A 57 (1993) 507.
- [60] G. Ertl, J. Koch, Z. Phys. Chem. 69 (1970) 323.
- [61] T.W. Orent, S.D. Bader, Surf. Sci. 115 (1982) 323.
- [62] E.M. Stuve, R.J. Madix, C.R. Brundle, Surf. Sci. 146 (1984) 155.
- [63] S.-L. Chang, P.A. Thiel, J. Chem. Phys. 88 (1988) 2071.
- [64] S.-L. Chang, P.A. Thiel, J.W. Evans, Surf. Sci. 205 (1988) 117.
- [65] J.F. Skelly, T. Bertrams, A.W. Munz, M.J. Murphy, A. Hodgson, Surf. Sci. 415 (1998) 48.
- [66] K. Klier, Y.-N. Wang, G.W. Simmons, J. Phys. Chem. 97 (1993) 633.
- [67] B. Klötzer, K. Hayek, C. Konvicka, E. Lundgren, P. Varga, Surf. Sci. 482-485 (2001) 237.
- [68] R.B. Shumbera, H.H. Kan, J.F. Weaver, Surf. Sci. 600 (2006) 2928.
- [69] N.A. Saliba, Y.-L. Tsai, C. Panja, B.E. Koel, Surf. Sci. 419 (1999) 79.
- [70] W.X. Li, L. Österlund, E.K. Vestergaard, R.T. Vang, J. Matthiesen, T.M. Pedersen, E. Lægsgaard, B. Hammer, F. Besenbacher, Phys. Rev. Lett. 93 (2004) 146104.
- [71] C.R. Parkinson, M. Walker, C.F. McConville, Surf. Sci. 545 (2003) 19.
- [72] A. Savitzky, M.J.E. Golay, Anal. Chem. 36 (1964) 1627.
- [73] D.A. Shirley, Phys. Rev. B 5 (1972) 4709.

- [74] H.A.E. Hagelin, J.F. Weaver, G.B. Hoflund, G.N. Salaita, *J. Electron Spectrosc. Relat. Phenom.* 124 (2002) 1.
- [75] H.A.E. Hagelin-Weaver, J.F. Weaver, G.B. Hoflund, G.N. Salaita, *J. Electron Spectrosc. Relat. Phenom.* 134 (2004) 139; and references therein.
- [76] G. Zheng, E.I. Altman, *Surf. Sci.* 462 (2000) 151.
- [77] G. Zheng, E.I. Altman, *Surf. Sci.* 504 (2002) 253.
- [78] G.M. Bancroft, I. Adams, L.L. Coatsworth, C.D. Bennewitz, J.D. Brown, W.D. Westwood, *Anal. Chem.* 47 (1975) 586.
- [79] T.L. Barr, *J. Phys. Chem.* 82 (1978) 1801.
- [80] M.-C. Jung, H.-D. Kim, M. Han, W. Jo, D.C. Kim, *Jpn. J. Appl. Phys.* 38 (1999) 4872.
- [81] S. Penner, P. Bera, S. Pedersen, L.T. Ngo, J.J.W. Harris, C.T. Campbell, *J. Phys. Chem. B* 110 (2006) 24577.
- [82] F.T. Wagner, P.N. Ross, Jr., *Appl. Surf. Sci.* 24 (1985) 87.
- [83] G.V. Samsonov (ed.), *The oxide handbook*, translated from Russian by C. N. Turton and T. I. Turton, New York, NY: IFI/Plenum, 1973.
- [84] C.T. Campbell, *Phys. Rev. Lett.* 96 (2006) 066106.
- [85] D.R. Lide (ed.), *CRC handbook of chemistry and physics : a ready-reference book of chemical and physical data*, 71st ed., Boca Raton, FL: CRC Press, 1990.
- [86] C.T. Campbell, *Surf. Sci. Rep.* 27 (1997) 1.
- [87] C.T. Campbell, personal communication (2006).
- [88] K. Reuter, M. Scheffler, *Appl. Phys. A* 78 (2004) 793.
- [89] E. Lundgren, G. Kresse, C. Klein, M. Borg, J.N. Andersen, M. De Santis, Y. Gauthier, C. Konvicka, M. Schmid, P. Varga, *Phys. Rev. Lett.* 88 (2002) 246103.

- [90] M. Todorova, E. Lundgren, V. Blum, A. Mikkelsen, S. Gray, J. Gustafson, M. Borg, J. Rogal, K. Reuter, J.N. Andersen, M. Scheffler, *Surf. Sci.* 541 (2003) 101.
- [91] E. Lundgren, J. Gustafson, A. Mikkelsen, J.N. Andersen, A. Stierle, H. Dosch, M. Todorova, J. Rogal, K. Reuter, M. Scheffler, *Phys. Rev. Lett.* 92 (2004) 046101.
- [92] J. Gustafson, A. Mikkelsen, M. Borg, J.N. Andersen, E. Lundgren, C. Klein, W. Hofer, M. Schmid, P. Varga, L. Köhler, G. Kresse, N. Kasper, A. Stierle, H. Dosch, *Phys. Rev. B* 71 (2005) 115442.
- [93] E. Lundgren, A. Mikkelsen, J.N. Andersen, G. Kresse, M. Schmid, P. Varga, *J. Phys.: Condens. Matter* 18 (2006) R481; and references therein.
- [94] J. Lauterbach, K. Asakura, H.H. Rotermund, *Surf. Sci.* 313 (1994) 52.
- [95] N. McMillan, T. Lele, C. Snively, J. Lauterbach, *Catal. Today* 105 (2005) 244.
- [96] P.R. Norton, R.L. Tapping, J.W. Goodale, *J. Vac. Sci. Technol.* 14 (1977) 446.
- [97] N. Cabrera, N.F. Mott, *Rep. Prog. Phys.* 12 (1949) 163.
- [98] F.P. Fehlner, N.F. Mott, *Oxid. Met.* 2 (1970) 59.
- [99] K.R. Lawless, *Rep. Prog. Phys.* 37 (1974) 231.
- [100] Y. Xu, W.A. Shelton, W.F. Schneider, *J. Phys. Chem. A* 110 (2006) 5839.
- [101] Q. Ge, P. Hu, D.A. King, M.-H. Lee, J.A. White, M.C. Payne, *J. Chem. Phys.* 106 (1997) 1210.
- [102] R.B. Shumbera, H.H. Kan, J.F. Weaver, *Surf. Sci.* 601 (2007) 4809.
- [103] J. Liu, M. Xu, T. Nordmeyer, F. Zaera, *J. Phys. Chem.* 99 (1995) 6167.
- [104] P.R. Norton, *Surf. Sci.* 44 (1974) 624.
- [105] P.R. Norton, P.J. Richards, *Surf. Sci.* 49 (1975) 567.

- [106] H. Gabasch, A. Knop-Gericke, R. Schlögl, M. Borasio, C. Weilach, G. Rupprechter, S. Penner, B. Jenewein, K. Hayek, B. Klötzer, *Phys. Chem. Chem. Phys.* 9 (2007) 533.
- [107] G. Zheng, E.I. Altman, *J. Phys. Chem. B* 106 (2002) 1048.
- [108] V.D. Thomas, J.W. Schwank, J.L. Gland, *Surf. Sci.* 464 (2000) 153.
- [109] K.-H. Allers, H. Pfnür, P. Feulner, D. Menzel, *J. Chem. Phys.* 100 (1994) 3985.
- [110] T.J. Lerotholi, G. Held, D.A. King, *Surf. Sci.* 601 (2007) 1285.
- [111] M.J.P. Hopstaken, J.W. Niemantsverdriet, *J. Chem. Phys.* 113 (2000) 5457.
- [112] H. Conrad, G. Ertl, J. Küppers, *Surf. Sci.* 76 (1978) 323.
- [113] A. Alavi, P. Hu, T. Deutsch, P.L. Silvestrelli, J. Hutter, *Phys. Rev. Lett.* 80 (1998) 3650.
- [114] A. Eichler, J. Hafner, *Surf. Sci.* 433-435 (1999) 58.
- [115] A. Eichler, J. Hafner, *J. Catal.* 204 (2001) 118.
- [116] Y.D. Kim, A.P. Seitsonen, S. Wendt, J. Wang, C. Fan, K. Jacobi, H. Over, G. Ertl, *J. Phys. Chem. B* 105 (2001) 3752.
- [117] B.K. Min, A.R. Alemozafar, M.M. Biener, J. Biener, C.M. Friend, *Top. Catal.* 36 (2005) 77.
- [118] H. Gabasch, W. Unterberger, K. Hayek, B. Klötzer, G. Kresse, C. Klein, M. Schmid, P. Varga, *Surf. Sci.* 600 (2006) 205.
- [119] A. Klust, R.J. Madix, *J. Chem. Phys.* 126 (2007) 084707.
- [120] R.B. Shumbera, H.H. Kan, J.F. Weaver, *J. Phys. Chem. C* 112 (2008) 4232.
- [121] A. Crossley, D.A. King, *Surf. Sci.* 95 (1980) 131.
- [122] T.E. Jackman, K. Griffiths, J.A. Davies, P.R. Norton, *J. Chem. Phys.* 79 (1983) 3529.
- [123] R.W. McCabe, L.D. Schmidt, *Surf. Sci.* 66 (1977) 101.
- [124] M.W. Lesley, L.D. Schmidt, *Surf. Sci.* 155 (1985) 215.

BIOGRAPHICAL SKETCH

Robert Bradley Shumbera, or Brad as his family and friends know him, was born on January 18, 1981, in Orlando, Florida, to Mark Andrew Shumbera and Dawn Annette Tilley. Brad was raised in the Kissimmee – St. Cloud area of Florida, where he graduated fourth in his class from Osceola High School in May 1999. Through these years, he benefited from the loving support of his parents and maternal grandparents, Bob and Faye Tilley. After high school, Brad enrolled in the School of Engineering at Vanderbilt University in Nashville, Tennessee, where he particularly enjoyed work for the Office of Housing and Residential Education as a resident advisor and head resident. In May 2003, he graduated cum laude with his Bachelor of Engineering in chemical engineering from Vanderbilt. On July 26, 2003, Brad married Kristen Lara Van Voorst in Clermont, Florida, before enrolling in graduate studies.

After an eventful summer in 2003, Brad returned to his native Florida and began working toward a Ph.D. in chemical engineering at the University of Florida in Gainesville, Florida. Under the supervision of Dr. Jason F. Weaver, Brad became educated in general surface science principles with a particular focus in kinetics and catalysis. While the majority of his research involved examining the growth, properties, and reactivity of the various high-concentration oxygen phases that form on the Pt(100) surface, Brad also participated in numerous investigations into non-thermal reaction chemistry on and the oxidation of the Pt(111), Pt(100), and Pd(111) surfaces. During his tenure, he also served as a teaching assistant for undergraduate courses in Materials of Chemical Engineering and Energy Transfer Operations. In May 2008, Brad received his Ph.D. in chemical engineering and began work as a Software Development Engineer with Bryan Research & Engineering, Inc. in Bryan, Texas.